Copyright Undertaking

This thesis is protected by copyright, with all rights reserved.

By reading and using the thesis, the reader understands and agrees to the following terms:

IMPORTANT

If you have reasons to believe that any materials in this thesis are deemed not suitable to be distributed in this form, or a copyright owner having difficulty with the material being included in our database, please contact lbsys@polyu.edu.hk providing details. The Library will look into your claim and consider taking remedial action upon receipt of the written requests.

ROBUST CONTROL AND FILTERING FOR SYSTEMS WITH STATE-DEPENDENT UNCERTAINTIES AND APPLICATIONS

LI ZHENGCHAO

PhD

The Hong Kong Polytechnic University

This programme is jointly offered by The Hong Kong Polytechnic University and Harbin Institute of Technology

2020

The Hong Kong Polytechnic University

Department of Mechanical Engineering

Harbin Institute of Technology

School of Astronautics

Robust Control and Filtering for Systems with State-dependent Uncertainties and Applications

LI ZHENGCHAO

A thesis submitted in partial fulfilment of the requirements

for the degree of Doctor of Philosophy

August 2019

CERTIFICATE OF ORIGINALITY

I hereby declare that this thesis is my own work and that, to the best of my knowledge and belief, it reproduces no material previously published or written, nor material that has been accepted for the award of any other degree or diploma, except where due acknowledgement has been made in the text.

_____ (Signed)

_____ LI Zhengchao _____ (Name of student)

Publications arising from the thesis

Journal Papers

1. **Zhengchao Li**, Xingjian Jing, and Jinyong Yu. Robust Nonlinear Human Following Control of a Tracked Mobile Robot with a Passive Quasi-zero-stiffness Suspension, 2020 (under preparation).

2. **Zhengchao Li**, Xingjian Jing, Bo Sun, and Jinyong Yu. Autonomous Navigation of a Tracked Mobile Robot with Novel Passive Bio-inspired Suspension, *IEEE/ASME Transactions on Mechatronics*, doi: 10.1109/TMECH. 2020 .2987004, 2020. (SCI, Regular paper, IF: 4.943)

3. **Zhengchao Li**, Xingjian Jing, and Jinyong Yu. Fault Detection Based on a Bio-Inspired Vibration Sensor System, *IEEE Access*, vol. 6, pp. 10867-10877, 2017. (SCI, Regular paper, IF: 4.098)

4. **Zhengchao Li**, Xudong Zhao, and Jinyong Yu. On Robust Control of Continuous-Time Systems with State-dependent Uncertainties and Its Application to Mechanical Systems, *ISA Transactions*, vol. 60, pp. 12-20, 2016. (SCI, Regular paper, IF: 4.343)

5. **Zhengchao Li** and Xudong Zhao. New Results on Robust Control for a Class of Uncertain Systems and Its Applications to Chua's Oscillator, *Nonlinear Dynamics*, vol. 84, no. 4, pp. 1929-1941, 2016. (SCI, Regular paper, IF: 4.604)

6. **Zhengchao Li**, Jingying Li, Jinyong Yu, and Xudong Zhao. Robust Filter Design for a Class of Uncertain Systems with $\mathcal{D}$ Stability Constraints under a Unified Framework. *Journal of The Franklin Institute*, vol. 353, no. 16, pp. 4233-4252, 2016. (SCI, Regular paper, IF: 3.653)

Conference Papers

1. **Zhengchao Li**, Xingjian Jing, and Jinyong Yu. Trajectory Tracking Control of a Tracked Mobile Robot with a Passive Bio-Inspired Suspension. *2019 IEEE International Conference on Mechatronics (ICM)*, Ilmenau, Germany, March, 2019, pp. 114-119.

2. **Zhengchao Li**, Xingjian Jing, and Jinyong Yu. Fault Detection based on a Bio-Inspired Vibration Sensor System. *the 11th Asian Control Conference (ASCC)*, Gold Coast, Australia, December, 2017, pp. 1918-1923.

Abstract

In mechanical systems, electronic circuits, and other fields of engineering, there exist many key structured subsystems, which mainly consist of core components with state-dependent uncertainties or state-dependent nonlinearities. To generate a suitable control law to overcome the imperfection of model and guarantee a certain performance against the presence of uncertainties or external disturbances, it is of great significance to research the problem of robust stability analysis and synthesis for this class of dynamic systems with state-dependent uncertainties. Based on a full understanding of the state of the art in state-dependent uncertain systems, this thesis focuses on robust control and filtering of state-dependent uncertain systems and applications.

The novelty and contribution of the thesis lie in the following aspects: (1) Robust stability analysis and synthesis of state-dependent uncertain systems are systematically addressed by constructing a novel parameter-dependent Lyapunov function and less conservative results are obtained by utilizing properties of the time-derivatives of state-dependent parameters. The proposed robust controller design methodology is applied to stabilization and synchronization of Chua's oscillator; (2) A novel robust filter design method for state-dependent uncertain systems is presented by introducing a generalized filtering performance index - extended dissipativity. H_∞, L_2-L_∞, passive and dissipative filtering problems can be solved successfully within a unified framework. The small current estimation problem of a tunnel diode circuit system under uncertain disturbances is solved by using the proposed robust filter design method; (3) A novel vibration sensor for real-time measurement of absolute vibration motion is developed based on a bio-inspired animal-limb-like structure with state-dependent nonlinearity. With this bio-inspired vibration sensor, the problems of error accumulation and real-time performance induced

by traditional measurement method using accelerometer can be effectively eliminated. A model-based fault detection algorithm using the vibration sensor is presented to deal with the real-time detection problem of fast time-varying weak fault signal which cannot be exactly identified by existing frequency-based and wavelet-based fault detection methods; (4) Robust autonomous navigation of a tracked mobile robot with passive bio-inspired suspension based on double-layer nonlinear model predictive control (NMPC) is proposed to improve the trajectory tracking accuracy against the slippage disturbances caused by unexpected "slippery track" phenomenon. The double layer NMPC scheme can accurately track the global reference trajectory and perform local trajectory optimization in occurrence of slippage disturbances with less computational burden; (5) Through estimating human's motion, a vision-based robust controller with disturbance compensation is designed to achieve better smoothness, rapidity, and accuracy of human-robot following. The developed vision based robust following controller can effectively prevent the target out of the robot camera's field of view (FOV) leading to following failure in narrow environment. The corresponding simulations and experiments have demonstrated the effectiveness and advantages of the developed robust control and filtering methods for state-dependent uncertain systems.

Acknowledgments

This work was done during my Ph.D. study at the Hong Kong Polytechnic University (PolyU) and at the Harbin Institute of Technology (HIT) under the joint Ph.D. programmes leading to dual awards. I would like to express my most sincere gratitude to Dr. JING Xingjian, my respectful chief supervisor at PolyU, for his persistent guidance and support. I also appreciate his profound knowledge and deep insight into the research topics and his assistance on completion of this thesis. I am also deeply indebted to Prof. Okyay Kaynak and Prof. YU Jinyong, my co-supervisors at HIT, for their continuous support and guidance of my Ph.D. study and related research. I am very grateful to Prof. GAO Huijun, the Director of Research Institute of Intelligent Control and Systems at HIT, for providing me with the unique opportunity to conduct research at HIT.

I would like to thank Prof. ZHAO Xudong, Prof. LIU Ming, and Prof. QIU Jianbin for their valuable discussions and enthusiastic supports. I would like to extend my thanks to all my wonderful friends and colleagues from research groups at PolyU and HIT. The list is too long to present. Their generous friendship and encouragement have always accompanied me and made my life more colorful, I wish them all the best.

Finally, I would like to thank my beloved wife and parents for their understanding, endless support and love.

Hung Hom, June 2019   LI, Zhengchao

Table of contents

List of Figures

List of Tables

List of notations and abbreviations

Notations

Notation	Description
$\mathbb{R}^n$	$n-$dimensional Euclidean space
$\forall$	for all
$\in$	belong to
$\approx$	approximately equal
s.t.	subject to
$\rightarrow$	approach
P^T	transport of P
P^{-1}	inverse of P
$[A]_s$	$A + A^T$
$diag\{...\}$	a block-diagonal matrix
$\|\cdot\|$	Euclidean norm or spectral norm
$P > 0$	matrix P is real symmetric and positive-definite
$\star$	a term in a block matrix induced by symmetry
$\mathcal{L}_2[0, \infty)$	square-integrable vector functions over $[0, \infty)$

Abbreviations

Abbreviation	Expansion
CCL	Cone Complementarity Linearization
FOV	Field of View
GPS	Global Positioning System
IMU	Inertial Measurement Unit
LMIs	Linear Matrix Inequalities
MSD	Mass-Spring-Damper
NMPC	Nonlinear Model Predictive Control
PID	Proportional-Integral-Derivative
PtoP	Peak-to-Peak
QZS	Quasi-Zero-Stiffness
RMS	Root-Mean-Square
RGB-D	Red Green Blue and Depth
STFT	Short-Time Fourier Transform
SDK	Software Development Kit

1 Introduction

1.1 Background and motivation

Robust control has been studied in extensive works [3–7] due to its applications in many practical control problems, e.g., power electronic systems [8], flight control systems [9], motion control systems [10] and networked control systems [11]. Indeed, a control law is typically designed from an idealized and simplified model of the practical control system. The potential problem of controller without considering the uncertainties is that closed-loop system performance and stability are easier to be affected, which indicates that the controller is not robust enough to suppress the uncertain disturbances. The goal of robust control is to generate a suitable control law to overcome the imperfection of model and guarantee a certain performance against the presence of uncertainties or external disturbances.

In robust control, the main sources of uncertainties consist of parameter variations, unmodelled dynamics and disturbance inputs [12–14]. Generally speaking, system uncertainties can be classified into unstructured and structured uncertainties. The former often consist of sensor noise and input disturbance. And the latter include discrepancies between the mathematical model and the actual physical plant. There exists a number of structured uncertain systems in practical industrial fields, where the variations of system parameters are closely dependent on system states. Objects with such uncertain parameters can be Chua's diode [15, 16], negative resistance oscillator [17] or Josephson junction [18] in electronic circuit systems; stiffness, inertia, damping, and viscosity coefficients in mechanical systems; aerodynamical coefficients in flight control systems [9] and

so on. Due to the effect of state-dependent behaviour, the systems have more colorful and complex characteristics, such as local stability, multiple equilibria, and domain of attraction. Traditional approaches of modeling, control and filtering to deal with general uncertain systems cannot be directly extended to this case. Consequently, it is of great practical significance to study such systems with state-dependent uncertainties or nonlinearities.

Robust stability analysis and synthesis

Most approaches of robust stability analysis for uncertain systems are developed based on the most traditional Lyapunov function with constant matrix P [19–22]. If the robust stability conditions can be formulated in terms of linear matrix inequalities(LMIs), the problem can be numerically solved by convex optimization techniques. Although, the traditional Lyapunov function with constant matrix P has been verified to be an efficient and powerful tool in the LMI framework for robust stability analysis and stabilization of systems with polytopic uncertainties. A serious limitation of traditional Lyapunov function with constant matrix P is that the conservativeness can lead to the result that constant matrix P does not exist for some uncertain systems. To relax the conservativeness of stability and stabilization problems, the parameter-dependent Lyapunov function [23] that is quadratic on the system state and depends affinely on the uncertain parameters will be introduced.

For systems with state-dependent uncertainties, there have been a few results reported in existing literatures. Stability analysis and stabilization are presented in [24], robust filtering is addressed in [25]. Note that the Lyapunov function proposed in [24], [25] is more complicated than normal parameter-dependent Lyapunov function due to the couplings of different Lyapunov matrices and the stabilization conditions in [24] are presented in terms of nonlinear matrix inequalities. Although the nonlinear matrix inequalities can be translated into the LMIs by using an iterative algorithm (e.g., cone complementarity linearization(CCL) technique [26]), but it is difficult to determine an initial feasible solution for the iterative algorithm.

Motivated by the above observations, a new parameter-dependent Lyapunov function that depends affinely on the state-dependent uncertain parameters is proposed to reduce the conservativeness and complexity.

Robust filter design

In practice, it is hard to directly and accurately measure the system state or the cost of measurement is probably expensive. As a branch of state estimation theory, robust filtering of uncertain dynamic systems has received growing attention due to its strong applications in both theoretical and practical areas. There have been a number of significant results on filtering problems for various dynamic systems, e.g., robust Kalman-Bucy filter for uncertain stochastic systems under persistent excitation [27], adaptive filter for robust proprioceptive robot impact detection under model uncertainties [28], periodically time-varying H_∞ memory filter [29], H_∞ filter for linear continuous-time systems with polytopic parameter uncertainties and time-varying state delay [30], robust L_2-L_∞ filter for systems with uncertain parameters [31], robust reliable dissipative filtering for networked control systems [32] and so on. Practical applications of robust filter can be found among various engineering areas involved in sensorless control of induction-motor drives based on robust filter and adaptive speed estimation [33], channel equalization of digital communication with nosy measurement based on reconstruction using H_∞ robust filter [34], robust fault detection and isolation filters for aircraft engine failure scenarios [35], target tracking from noise-corrupted measurements based on robust filtering [36], spacecraft attitude estimation based on robust adaptive unscented Kalman filter [37], etc.

Transient response are basically equally important as stability and robustness of the closed-loop system. Besides the constraint of decay rate, one efficient approach to guarantee satisfactory transient response is placing the poles in a suitable region (e.g., circular region and disk region). Such problems are referred as $\mathcal{D}$-stability problems. There are some published literatures taking the pole placement issue into consideration in robust filtering problem [38–41]. For example, in [38], a full order H_∞ filter with filter dynamics

constrained to some specific regions inside the unit open disk was designed for discrete-time systems subjected to polytope type uncertainty. A H_∞ filter is designed for linear continuous system with parameter uncertainties and parabolic pole assignment in [41]. Thus, to achieve expected dynamic performances for filtering error system, $\mathcal{D}$ stability constraint is considered when designing robust filter for state-dependent uncertain systems.

Motivated by the above observations, this thesis considers the problem of robust filter design for continuous-time uncertain system with state-dependent uncertainties, taking the $\mathcal{D}$ stability constraints into consideration, based on a new performance index–extended dissipativity. With this generalized performance index, some classical filtering problems such as H_∞, $L_2 - L_\infty$, passive, mixed $H_\infty/$ passive, and dissipative filtering problems can be solved successfully under a unified framework. This can allow us to choose a suitable filtering strategy according to different practical applications or noise levels, which is conveniently implemented by adjusting the weighting matrices in the generalized performance index.

Vibration sensor with state-dependent nonlinearity

Vibration analysis is one of the fundamental condition monitoring techniques for machinery maintenance and fault diagnosis, which can be used in the cases of manufacturing and operating to realize the quality control and health monitoring. During past decades, a series of significant results on vibration-based fault diagnosis have been reported in various fields of industrial applications, such as railway wheel flat fault detection [42], winding deformation detection of power grid transformer [43, 44], and structural damage detection of gear, bearing, stator and rotor in mechanical system [45–49].A key factor of conducting fault detection is to acquire accurate vibration signals, including amplitude, velocity, and acceleration. For example, in power grid transformer, it is desired to use vibration motion to describe the degree of winding deformation. A general way is to use accelerometer as the measurement of vibration motion. Nevertheless, this solution will lead to serious problem of error accumulation due to double time-domain integration of

the acceleration signal with non-zero mean. Especially, the accumulation error increases over the time. An alternative method is adopting frequency-domain integral instead of the time-domain. Through setting the corresponding low-frequency component generated from integral as zero, the accumulation error can be cancelled. It is worth pointing out the frequency-domain integral requires a complete acceleration signal, which indicates that the frequency-domain integral cannot be extended to real-time fault detection. Besides, some studies also use laser [50] to measure absolute motion, but which holds very strict requirements on installation space and environments. Hence, an interesting and challenging topic arises naturally: *whether is it possible to simply and effectively realize the real-time measurement of absolute vibration motion by resorting to some novel measurement methods*? One of the purposes of this thesis is to give a positive answer to the above question by resorting to the state-dependent nonlinearity.

On the other hand, nonlinear structure with very beneficial state-dependent stiffness and damping characteristics has received growing attention due to its excellent performance of achieving vibration isolation or suppression [51–55]. Some applications of nonlinear structure can be found in vibration isolator with state-dependent quasi-zero-stiffness (QZS) [52–54]. Recently, a novel nonlinear structure inspired by the limb structures of animals and insects in motion vibration control has been systematically investigated in [56–58]. This novel structure is also called Z-like or X-like structure. The X-like structure can be regarded as the combination of Z-like structure. Compared with existing QZS structures, this bio-inspired structure has better loading capacity and equilibrium stability. Meanwhile, this bio-inspired structure can be easily implemented with only linear spring and damper components.

Based on the previous discussion about bio-inspired structure, a bio-inspired vibration sensor using state-dependent quasi-zero-stiffness mechanism for accurate real-time measurement of absolute motion will be constructed in this thesis. In addition, an application example of fault detection using the bio-inspired vibration sensor is also presented.

Robust navigation control of mobile robots

Robots have shown their great application potential in various engineering areas, such as search and rescue, logistics and transportation, patrol and surveillance, service and nursing [59–67]. The tracked mobile robot with obvious advantages of moving in the rough terrain environment and negotiating irregular obstacles has received continuous attentions [68–70]. It is worth pointing out that most of the significant results on the tracked mobile robot are focused on the obstacle negotiation capability, like the actively articulated tracked robot [70]. Although the active technologies can effectively improve the trafficability, the system complexity and energy consumption will also increase [71], [72]. A few research is focused on the passive suspension design. Most of the passive suspension of the tracked mobile robot are based on the conventional mass-spring-damping system, which has inherent trade-off between the loading capacity and vibration isolation performance. Thus, how to design the passive suspension system with guarantee of both loading capacity and vibration isolation performance is still a challenge worth further studying.

The previously mentioned bio-inspired structure has shown high static stiffness, low dynamic stiffness and broad frequency range of vibration isolation [53, 56, 73]. Compared with the conventional mass-spring-damping system, this bio-inspired structure has potential for providing better loading capacity and vibration isolation performance. The bio-inspired structure provides a novel solution to overcome the inherent trade-off between the loading capacity and vibration isolation performance. On the other side, with a stable upper platform, vibration attenuation abilities of some high precision systems mounted on the mobile robot can be enhanced, like the poor image quality problems induced by camera vibration. Inspired from the bio-inspired structure, a tracked mobile robot platform with novel passive bio-inspired suspension will be introduced in this thesis.

Autonomous navigation ability plays an important role in unmanned operation. However the uncertainties of kinematics equation induced by unknown slippage disturbance have severe restrictions on navigation accuracy of mobile robots [74–76]. The slippage is

closely dependent on the robot's state. Slippage during turning or obstacle negotiating is even more obvious. Traditional control methods using GPS to measure the slippage for compensation are not available in the GPS denied environment [74]. To address this problem, robust navigation control using nonlinear model predictive control (NMPC) method is considered. The NMPC algorithm has appeared its powerful capability on the trajectory tracking control of mobile robot under the constrained input conditions [77–79]. The advantages of NMPC are the on-line optimization over a finite horizon based on the current measurement and prior model. To compensate the slippage disturbance, the prior mode of NMPC is updated in real time by using the odometry and IMU to measure the slippage instead of GPS. In order to implement the perception and navigation, laser radar and camera are generally used to generate the outline map of surrounding environment. Due to the mapping processing latency, the NMPC scheme is performed at a relatively low frequency, which cannot capture the slippage disturbance timely. Though lifting method in [80] can effectively increase the control frequency, the computational complexity caused by frequency lifting will increase to a very high level for the case with a long horizon [81]. Usually, a long horizon can prevent from local oscillation behaviour and guarantee motion smoothness. Importantly, due to the "soft suspension", the tracked robot under this study is subject to unexpected "slippery track" phenomenon when passing a ground obstacle although the track is not really slipped. Hence, one of the main concerns of this thesis is to design robust navigation controller to improve trajectory tracking accuracy of the tracked mobile robot against the uncertain slippage disturbance with less computational burden.

Robust following control of mobile robots

Human-following capability is one of the most important things for human-robot interaction. Vision based tracking technology is a natural and flexible way to achieve human-following control in unstructured environment. By resorting to vision based tracking technology, the robot can follow a specified human to provide some services or accomplish some human-robot collaborative tasks [82–87]. Potential applications of the human-following control are summarized as follows: (1). personal assistant robots carry-

ing heavy packages and following the passengers in airport [88]. (2). retail service robots carrying merchandise, providing in-store customer service and following the customer to the checkout counter [89]. Through the vision based human-following, the tracked mobile robot is capable of assisting human to carry heavy stuff or perform tasks in some unstructured environments conveniently. Human-following smoothness and keeping the target within the robot camera's field of view (FOV) are the key performance indicators to evaluate the human-following controller. Due to the fact that human's motion is often completely unpredictable, traditional human-following method using proportional-integral-derivative (PID) controllers cannot simultaneously guarantee the smoothness and rapidity of human-following [86].

Thus, this thesis will looks into the challenges of designing a robust controller with disturbance compensation for vision based human following control of this tracked mobile robot. In addition, the hand gesture recognition based human-robot interaction and collision avoidance capabilities are also considered for the human-following control.

1.2 Objectives of this work

Motivated by the aforementioned background and the state of the art of state-dependent uncertain systems, the main objective of this thesis is to investigate the robust control and filtering of state-dependent uncertain systems and applications on vibration sensor and tracked mobile robot. The objectives are listed as follows.

- Construct a parameter-dependent Lyapunov function to reduce the conservativeness of robust stability analysis conditions using the most traditional Lyapunov function with constant matrix P. Model-dependent state-feedback stabilization scheme design based on the parameter-dependent Lyapunov function.

- Robust filter design for state-dependent uncertain systems by introducing a more generalized performance index. Solve some classical filtering problems under a unified framework.

- Use a bio-inspired limb-like structure with state-dependent quasi-zero-stiffness characteristic to construct a vibration sensor system. Apply this sensor to absolute motion measurement and fault detection.

- Develop a tracked mobile robot with passive bio-inspired suspension to enhance the capability of traversing very rugged terrain and maintaining stability. Adopt the model predictive control method to realize the robust navigation control in occurrence of uncertain disturbance, like the obvious slippage during turning or obstacle negotiating.

- Estimate the unknown disturbance caused by human motion through using the depth skeleton image. Design a vision-based robust human-following controller with disturbance compensation. Implement the hand gesture recognition based human-robot interaction and laser radar based collision avoidance.

1.3 Contributions of the thesis

The main contributions of this thesis are summarized as follows:

(1) The robust stability analysis and stabilization for continuous-time systems with state-dependent uncertainties are addressed via constructing a new parameter-dependent Lyapunov function. It is noted that the stability analysis conditions utilizing the property of the time-derivatives of state-dependent parameters have the potential of significantly reducing conservativeness compared to the most traditional quadratic Lyapunov function with constant matrix P. A model-dependent state-feedback stabilization scheme, which can provide more flexibility in controller synthesis, is also proposed. This study provides a flexible and low conservative method for the robust stability analysis and synthesis of state-dependent uncertain systems.

(2) A systematic and novel filter design method for state-dependent uncertain systems is proposed by introducing a generalized performance index - extended dissipativity. Some classical filtering problems such as H_∞, L_2-L_∞, passive and dissipative filtering problems for state-dependent uncertain systems can be solved successfully within a unified framework.

(3) A novel vibration sensor based on a bio-inspired animal-limb-like structure with state-dependent nonlinearity is developed for the real-time measurement of absolute vibration motion. With this bio-inspired vibration sensor, the problems of error accumulation and real-time performance induced by traditional measurement method using accelerometer can be effectively eliminated. This vibration sensor provides an effective and convenient way to measure the absolute vibration motion especially for moving platforms. A model-based fault detection algorithm using the vibration sensor is proposed to cope with the real-time detection problem of weak fault with fast time-varying characteristic which cannot be exactly identified by existing methods.

(4) The developed tracked mobile robot with passive bio-inspired suspension provides a new alternative to existing mobile robots with passive mass-spring-damper suspension for simultaneously enhancing the capability of traversing very rugged terrain and maintaining stability. Additionally, the proposed robust navigation control using double layer nonlinear model predictive control strategy can effectively improve the trajectory tracking accuracy against the unknown slippage disturbances with less computational burden.

(5) A vision based robust controller with disturbance compensation is proposed for the human following of tracked mobile robot. The human's motion is accurately estimated through using the depth skeleton image measured by RGB-D camera. With this robust control strategy, the tracking controller has the advantage of simultaneously guaranteeing the smoothness and quick response of human-following. The newly developed vision based robust human following controller can prevent the target out of the robot camera's FOV leading to following failure for human following in narrow environment.

1.4 Outline of the thesis

The thesis is organized as follows. Chapter 2 introduces a novel parameter-dependent Lyapunov function for the robust stability analysis and synthesis of the state-dependent uncertain systems. Chapter 3 investigates the robust filter design problem of state-

dependent uncertain systems based on a generalized performance - extended dissipativity. A novel vibration sensor system based on state-dependent nonlinearity for absolute motion measurement and the application on fault detection are developed in Chapter 4. In Chapter 5, a tracked mobile robot with a novel passive bio-inspired suspension is developed. The robust navigation using model predictive control method is also realized for improving the trajectory tracking accuracy against the slippage disturbance. In Chapter 6, a vision based robust human following controller is developed for the tracked mobile robot to assist human with carrying heavy stuff or performing tasks in some unstructured environments. Chapter 7 concludes the thesis and discusses some future research directions.

2 Robust stability analysis and synthesis for state-dependent uncertain systems

This chapter will investigate the problems of robust stability analysis and synthesis for state-dependent uncertain systems, which are assumed to be of the polytopic type. A new parameter-dependent Lyapunov function that depends affinely on uncertain parameters is proposed to replace the non-quadratic Lyapunov function in [24]. As demonstrated in a numerical example, there exists a parameter-dependent Lyapunov function whereas the most traditional quadratic Lyapunov function with constant matrix P does not exist. Therefore, our approach can lead to increased applicability and reduced conservativeness. Furthermore, in order to fully take advantage of the parameter-dependent Lyapunov function, we propose a model-dependent state-feedback stabilization scheme that can provide more flexibilities in controller synthesis, where the time derivatives are assumed to be computable from the states and the stabilization conditions are presented in terms of LMIs. The new model-dependent feedback controller contains the static state-feedback controller as a special case. A numerical example is provided to illustrate the effectiveness of the proposed approaches. Finally, we apply the developed methodology to stabilization and synchronization of Chua's oscillator, which has wide applications in power electronic systems and secure communication systems [90], [91]. Consequently, it is of great practical significance to apply the developed methodology to stabilization and synchronization of Chua's oscillator.

The remainder of this chapter is structured as follows. Section 2.1 starts with the model

description of continuous-time systems with state-dependent polytopic uncertainties and introduces a new parameter-dependent Lyapunov function. Robust stability conditions for the considered uncertain systems are established on the basis of parameter-dependent Lyapunov function proposed in Section 2.2, and then a relaxed stability condition that utilizes a property of the time-derivatives of uncertain parameters is given. Section 2.3 presents a new model-dependent state-feedback stabilization scheme. A numerical example and a Chua's oscillator system are presented in Section 2.4 to demonstrate the effectiveness and applicability of the proposed methodologies. Finally, Section 2.5 concludes the chapter.

2.1 Problem formulation and preliminaries

Consider the following continuous-time system with state-dependent uncertainties:

$$\begin{cases} \dot{x}(t) = A(\sigma(x(t)))x(t) + B(\sigma(x(t)))u(t) \\ y(t) = Cx(t) \end{cases} \tag{2.1.1}$$

where $x(t) \in \mathbb{R}^{n_x}$ is the system state; $u(t) \in \mathbb{R}^{n_u}$ is the control input; $y(t) \in \mathbb{R}^{n_y}$ is the system output; $\sigma(x(t)) \in \mathbb{R}^m$ is the uncertain parameter vector, representing the state-dependent unknown parametric perturbations; System (2.1.1)'s state matrix $A(\sigma(x(t)))$ and control matrix $B(\sigma(x(t)))$ are described by the following convex polytopic sets:

$$\mathcal{A} = \{A(\sigma(x(t)))|A(\sigma(x(t))) = \sum_{i=1}^{m} \sigma_i(x_\sigma^i(t))A_i\} \tag{2.1.2}$$

$$\mathcal{B} = \{B(\sigma(x(t)))|B(\sigma(x(t))) = \sum_{i=1}^{m} \sigma_i(x_\sigma^i(t))B_i\} \tag{2.1.3}$$

where $A_i \in \mathbb{R}^{n_x \times n_x}$ and $B_i \in \mathbb{R}^{n_x \times n_u}$ are vertices of the corresponding uncertainty polytope, which are known real constant matrices; In addition, $x_\sigma^i(t)$ is a vector whose entries are elements of state $x(t)$; $\sigma_i(x_\sigma^i(t))$ is the complement of uncertain parameter vector,

which satisfies the following properties:

$$\sigma_i(x_\sigma^i(t)) > 0, \sum_{i=1}^{m}\sigma_i(x_\sigma^i(t)) = 1 \tag{2.1.4}$$

Any continuous-time systems with state-dependent uncertainties in the form of (2.1.1) can be expressed in the following more convenient form

$$\begin{cases} \dot{x}(t) = \sum_{i=1}^{m}\sigma_i(x_\sigma^i(t))A_ix(t) + \sum_{i=1}^{m}\sigma_i(x_\sigma^i(t))B_iu(t) \\ y(t) = Cx(t) \end{cases} \tag{2.1.5}$$

To establish the robust stability and stabilization conditions of system (2.1.5), the following candidate Lyapunov function is proposed

$$V(x(t)) = x^T(t)\sum_{i=1}^{m}\sigma_i(x_\sigma^i(t))P_ix(t) \tag{2.1.6}$$

where P_i is a positive-definite matrix. It follows that, Lyapunov function $V(x(t))$, defined from a set of positive definite matrices $P_i, i \in S = \{1, 2, \ldots, m\}$ and uncertain parameters $\sigma_i(x_\sigma^i(t))$, $i \in S$, satisfies i) $V(0) = 0$; ii) $V(x(t))$ is a continuously differentiable function; iii) $V(x(t)) > 0, \forall x(t) \in R^{n_x}\backslash 0^{n_x}$; iv) $\|x(t)\| \rightarrow \infty \Rightarrow V(x(t)) \rightarrow \infty$.

2.2 Robust stability conditions

The robust stability conditions for system (2.1.5) with $u(t) = 0$ by resorting to the most traditional quadratic Lyapunov function with constant matrix P can be summed up in Theorem 2.1 [24].

Theorem 2.1 *[24] System (2.1.5) with $u(t) = 0$ is stable if there exists a symmetric positive-definite matrix P, such that, $\forall i \in S$,*

$$PA_i + A_i^TP < 0 \tag{2.2.1}$$

However, Theorem 2.1 developed by a single Lyapunov function suffers from the problem of serious conservativeness, which can lead to the result that a common Lyapunov function does not exist for some uncertain systems. An alternative approach is to consider the parameter dependent Lyapunov function given in (2.1.6). Theorem 2.2 gives sufficient conditions to guarantee the stability of (2.1.5) with $u(t) = 0$ when parameter dependent Lyapunov function is considered.

Theorem 2.2 *Assume that $\dot{\sigma}_r(x_\sigma^r(t)) \le \phi_r$, $r \in S$, system (2.1.5) with $u(t) = 0$ is stable if there exists a set of symmetric positive-definite matrices P_r, $r \in S$, such that*

$$\frac{1}{2}(A_i^T P_j + P_j A_i + A_j^T P_i + P_i A_j) + \sum_{r=1}^m \phi_r P_r < 0, i \le j \qquad (2.2.2)$$

Proof. According to the candidate of Lyapunov function (2.1.6), one has that

$$
\begin{aligned}
\dot{V}(x(t)) =& x^T(t) \sum_{i=1}^m \sum_{j=1}^m \sigma_i(x_\sigma^i(t))\sigma_j(x_\sigma^j(t))(A_j^T P_i + P_i A_j)x(t) \\
&+ x^T(t) \sum_{r=1}^m \dot{\sigma}_r(x_\sigma^r(t)) P_r x(t) \\
=& x^T(t) \sum_{i=1}^m \sum_{j=1}^m \sigma_i(x_\sigma^i(t))\sigma_j(x_\sigma^j(t))\frac{1}{2}(A_j^T P_i + P_i A_j \\
&+ A_i^T P_j + P_j A_i)x(t) + x^T(t) \sum_{r=1}^m \dot{\sigma}_r(x_\sigma^r(t)) P_r x(t) \qquad (2.2.3)
\end{aligned}
$$

By considering $\dot{\sigma}_r(x_\sigma^r(t)) \le \phi_r$, $r \in S$, it follows that

$$
\begin{aligned}
\dot{V}(x(t)) \le& x^T(t) \sum_{i=1}^m \sum_{j=1}^m \sigma_i(x_\sigma^i(t))\sigma_j(x_\sigma^j(t))\{\frac{1}{2}(A_j^T P_i \\
&+ P_i A_j + A_i^T P_j + P_j A_i) + \sum_{r=1}^m \phi_r P_r\}x(t) \qquad (2.2.4)
\end{aligned}
$$

Therefore, if (2.2.2) holds, $\dot{V}(x(t)) < 0$, $\forall x(t) \ne 0$, which indicates the asymptotic stability of system (2.1.5) with $u(t) = 0$. $\qquad \square$

Remark 2.1 *: The stability conditions in (2.2.2) contain information about the time-derivatives of the uncertain parameters, which may have advantage of leading to a less*

conservative result in stability analysis. Note that (2.2.2) represents a set of LMIs if $\phi_r, r \in S$ can be given in advance. Scalars ϕ_r denote the upper bounds to the time-derivative of $\sigma_r(x_\sigma^r(t))$. However, ϕ_r cannot be always obtained in practical control problems, which is also commented by [92], [93]. Thus, stability analysis conditions in Theorem 2.2 are only suitable to the systems with available boundary conditions ϕ_r.

By introducing more variables P_i, LMIs (2.2.2) are seem less restrictive than (2.2.1). But there is a very obvious difference between LMIs (2.2.1) and (2.2.2) . Parameter-dependent Lyapunov function (2.1.6) generates information about the time derivatives of uncertain parameters into LMIs (2.2.2), whereas there is no such a term in LMIs (2.2.1). If $P_i = P_j = P$ and $\phi_i = \phi_j = 0, \forall i, j \in S$, conditions in Theorem 2.2 reduce to the conditions in Theorem 2.1. Theorem 2.2 must always provide better results than Theorem 2.1, when the matrices sum $\sum_{r=1}^{m} \phi_r P_r$ in (2.2.2) is negative-definite. It seems that Theorem 2.2 can provide better results, or at least the same, than Theorem 2.1 for some cases. Actually this is not true for every case. That will be illustrated by a numerical example later.

Through considering an important property of the time derivatives of uncertain parameters, a relaxed stability analysis approach to guarantee the stability of (2.1.5) with $u(t) = 0$ is given in Theorem 2.3. The property is

$$\sum_{r=1}^{m} \dot{\sigma}_r(x_\sigma^r(t)) = 0 \qquad (2.2.5)$$

According to property (2.2.5), it follows that

$$\dot{\sigma}_z(x_\sigma^z(t)) = \sum_{r \neq z}^{m} \dot{\sigma}_r(x_\sigma^r(t)), z \in S \qquad (2.2.6)$$

By applying (2.2.6), stability conditions given in Theorem 2.2 can be relaxed as follows in Theorem 2.3.

Theorem 2.3 *Assume that $\dot{\sigma}_v(x_\sigma^v(t)) \leq \phi_v$, $\phi_z = \max\{\phi_1, \phi_2, \dots, \phi_m\}$, system (2.1.5) with $u(t) = 0$ is stable, if there exists a set of symmetric positive-definite matrices P_v,*

$v \in S$, *such that*

$$P_r - P_z \geq 0 \qquad (2.2.7)$$

$$\frac{1}{2}(A_j^T P_i + P_i A_j + A_i^T P_j + P_j A_i) + \sum_{r \neq z}^{m} \phi_r(P_r - P_z) < 0 \qquad (2.2.8)$$

$$r \neq z, r, z, \in S, i \leq j, i, j \in S$$

Proof. Consider (2.1.6) as a Lyapunov function candidate, then

$$
\begin{aligned}
\dot{V}(x(t)) =& x^T(t) \sum_{i=1}^{m}\sum_{j=1}^{m} \sigma_i(x_\sigma^i(t))\sigma_j(x_\sigma^j(t))\frac{1}{2}(A_j^T P_i + P_i A_j \\
&+ A_i^T P_j + P_j A_i)x(t) + x^T(t)\sum_{r=1}^{m}\dot{\sigma}_r(x_\sigma^r(t))P_r x(t) \\
=& x^T(t) \sum_{i=1}^{m}\sum_{j=1}^{m} \sigma_i(x_\sigma^i(t))\sigma_j(x_\sigma^j(t))\frac{1}{2}(A_j^T P_i + P_i A_j \\
&+ A_i^T P_j + P_j A_i)x(t) + x^T(t)\sum_{r \neq z}^{m}\dot{\sigma}_r(x_\sigma^r(t))P_r x(t) \\
&+ x^T(t)\dot{\sigma}_z(x_\sigma^z(t))P_z x(t) \qquad (2.2.9)
\end{aligned}
$$

From (2.2.6)

$$
\begin{aligned}
\dot{V}(x(t)) =& x^T(t) \sum_{i=1}^{m}\sum_{j=1}^{m} \sigma_i(x_\sigma^i(t))\sigma_j(x_\sigma^j(t))\frac{1}{2}(A_j^T P_i + P_i A_j + \\
& A_i^T P_j + P_j A_i)x(t) + x^T(t)\sum_{r \neq z}^{m}\dot{\sigma}_r(x_\sigma^r(t))(P_r - P_z)x(t) \qquad (2.2.10)
\end{aligned}
$$

Assuming that $\dot{\sigma}_r(x_\sigma^r(t)) \leq \phi_r$, $r \in S$ and (2.2.7) hold, it follows that

$$
\begin{aligned}
\dot{V}(x(t)) \leq& x^T(t) \sum_{i=1}^{m}\sum_{j=1}^{m} \sigma_i(x_\sigma^i(t))\sigma_j(x_\sigma^j(t))\{\frac{1}{2}(A_j^T P_i + P_i A_j \\
&+ A_i^T P_j + P_j A_i) + \sum_{r \neq z}^{m}\phi_r(P_r - P_z)\}x(t) \qquad (2.2.11)
\end{aligned}
$$

If condition (2.2.8) holds, then $\dot{V}(x(t)) < 0$, $\forall x(t) \neq 0$ and system (2.1.5) with $u(t) = 0$ is globally asymptotically stable. This completes the proof $\qquad \square$

According to the comparison between Theorem 2.1 and Theorem 2.2, the matrices

sum $\sum_{r=1}^{m}\phi_r P_r$ may be pointed out as the main source of conservatism. And $\phi_z = \max\{\phi_1, \phi_2, \ldots, \phi_m\}$ plays an important role in the matrices sum $\sum_{r=1}^{m}\phi_r P_r$. By considering the property (2.2.5), the contribution of ϕ_z is neglected. The matrices sum $\sum_{r=1}^{m}\phi_r P_r$ in (2.2.2) is translated to $\sum_{r\neq z}^{m}\phi_r(P_r - P_z)$ in (2.2.8). Thus, (2.2.8) are more relaxed conditions than (2.2.2), and Theorem 2.3 can provide a less conservative version of Theorem 2.2.

2.3 State-feedback controller stabilization

In this section , the stabilization problem for the closed-loop system will be investigated. To take full advantage of the parameter-dependent Lyapunov function, a new model-dependent state-feedback controller design approach will be proposed in this case, where the time derivatives of parameters $\sigma_i(x_\sigma^i(t))$ can be calculated from system states. Consider the following model-dependent state-feedback control law

$$u_i(t) = K_i x(t), i \in S \tag{2.3.1}$$

where $u_i(t)$ is virtual control input of the corresponding uncertainty polytope, K_i is the model-dependent state-feedback gain matrix. Then, the resulting closed-coop system can be represented as

$$\dot{x}(t) = \sum_{i=1}^{m}\sigma_i(x_\sigma^i(t))(A_i + B_i K_i)x(t) \tag{2.3.2}$$

Assume that $K(x(t))$ is a real model-dependent state-feedback controller, which is closely related to the uncertainty polytope. Model-dependent state-feedback control law can be rewritten as the following form

$$u(t) = K(x(t))x(t) \tag{2.3.3}$$

According to the design approach of model-dependent state-feedback control law (2.3.1), it follows that $K(x(t))$ satisfies the following property

$$B(\sigma(x(t)))K(x(t)) = \sum_{i=1}^{m}\sigma_i(x_\sigma^i(t))B_iK_i \qquad (2.3.4)$$

Theorem 2.4 gives stabilization conditions via the new model-dependent state-feedback controller (2.3.1).

Theorem 2.4 *Assume that* $\dot{\sigma}_i(x_\sigma^i(t)) \le \phi_i$, $|\phi_z| = \max\{|\phi_1|, |\phi_2|, \ldots, |\phi_m|\}$. *If there exist scalars* ϵ, λ, *positive-definite matrices* $\bar{P}_i$, *and matrices* $\bar{Q}_{ij}$, *such that*

$$\frac{1}{(\lambda+1)\epsilon}I < \bar{P}_r < \frac{1}{\epsilon}I, \ \frac{1}{\epsilon}I < \bar{P}_z \qquad (2.3.5)$$

$$\begin{bmatrix} [A_j\bar{P}_i + B_j\bar{Q}_{ij}]_s & \bar{P}_i \\ \bar{P}_i^T & -[\sum\limits_{r\neq z}^{m}|\phi_r|\,\epsilon(\lambda+1)I]^{-1} \end{bmatrix} < 0 \qquad (2.3.6)$$

$$0 < \epsilon, 0 < \lambda, r \neq z, r, z, \in S, i, j \in S$$

where

$$K_j = \bar{Q}_{ij}\bar{P}_i^{-1}$$

then the system (2.1.5) can be stabilized by the state-feedback controller (2.3.1).

Proof. Consider (2.1.6) as a Lyapunov function candidate, then

$$
\begin{aligned}
\dot{V}(x(t)) =& x^T(t)\sum_{i=1}^{m}\sum_{j=1}^{m}\sigma_i(x_\sigma^i(t))\sigma_j(x_\sigma^j(t))(G_j^TP_i + P_iG_j)x(t) \\
& + x^T(t)\sum_{r=1}^{m}\dot{\sigma}_r(x_\sigma^r(t))P_rx(t) \\
=& x^T(t)\sum_{i=1}^{m}\sum_{j=1}^{m}\sigma_i(x_\sigma^i(t))\sigma_j(x_\sigma^j(t))(G_j^TP_i + P_iG_j)x(t) \\
& + x^T(t)\sum_{r\neq z}^{m}\dot{\sigma}_r(x_\sigma^r(t))P_rx(t) + x^T(t)\dot{\sigma}_z(x_\sigma^z(t))P_zx(t) \qquad (2.3.7)
\end{aligned}
$$

where $G_j = A_j + B_j K_j$. From (2.2.6), one obtains

$$\dot{V}(x(t)) = x^T(t) \sum_{i=1}^{m} \sum_{j=1}^{m} \sigma_i(x_\sigma^i(t)) \sigma_j(x_\sigma^j(t))(G_j^T P_i + P_i G_j) x(t)$$

$$+ x^T(t) \sum_{r \neq z}^{m} \dot{\sigma}_r(x_\sigma^r(t))(P_r - P_z) x(t) \tag{2.3.8}$$

Denoting $\bar{P}_i = P_i^{-1}, i \in S$, (2.3.5) is equal to

$$\frac{I}{(\lambda + 1)\epsilon} < P_r^{-1} < \frac{I}{\epsilon}, \ \frac{I}{\epsilon} < P_z^{-1}, \ 0 < \epsilon, \ 0 < \lambda \tag{2.3.9}$$

Due to (2.3.9), the following relations hold

$$\begin{cases} 0 < P_z \\ 0 < \epsilon P_z^{-1} - I \qquad\qquad \Rightarrow P_z < \epsilon I \\ P_z(\epsilon P_z^{-1} - I) = (\epsilon P_z^{-1} - I)P_z \end{cases} \tag{2.3.10}$$

$$\begin{cases} 0 < P_r \\ 0 < I - \epsilon P_r^{-1} \qquad\qquad \Rightarrow \epsilon I < P_r \\ P_r(I - \epsilon P_r^{-1}) = (I - \epsilon P_r^{-1})P_r \end{cases} \tag{2.3.11}$$

$$\begin{cases} 0 < P_r \\ 0 < \epsilon(\lambda + 1)P_r^{-1} - I \\ P_r[\epsilon(\lambda + 1)P_r^{-1} - I] = [\epsilon(\lambda + 1)P_r^{-1} - I]P_r \end{cases}$$
$$\Rightarrow P_r < \epsilon(\lambda + 1)I \tag{2.3.12}$$

Then, (2.3.13) can be obtained from (2.3.10), (2.3.11) and (2.3.12)

$$0 < P_r - P_z < \epsilon(\lambda + 1)I \tag{2.3.13}$$

Assuming that $\dot{\sigma}_i(x_\sigma^r(t)) \leq \phi_i, \ i \in S$. According to (2.3.8) and (2.3.13), it follows that

$$\dot{V}(x(t)) \leq x^T(t) \sum_{i=1}^{m} \sum_{j=1}^{m} \sigma_i(x_\sigma^i(t)) \sigma_j(x_\sigma^j(t))[(G_j^T P_i + P_i G_j)$$

$$+ \sum_{r \neq z}^{m} |\phi_r| (P_r - P_z)] x(t)$$

$$< x^T(t) \sum_{i=1}^{m} \sum_{j=1}^{m} \sigma_i(x_\sigma^i(t)) \sigma_j(x_\sigma^j(t)) [(G_j^T P_i + P_i G_j)$$

$$+ \sum_{r \neq z}^{m} |\phi_r| \epsilon(\lambda+1)I] x(t) \qquad (2.3.14)$$

Thus, $\dot{V}(x(t))$ is negative if there exist scalars $\epsilon > 0$ and $\lambda > 0$ such that

$$(G_j^T P_i + P_i G_j) + \sum_{r \neq z}^{m} |\phi_r| \epsilon(\lambda+1)I < 0 \qquad (2.3.15)$$

Then, perform congruence transformation to (2.3.15) by P_i^{-1} with the change of matrix variables defined by

$$\bar{P}_i = P_i^{-1}, \ \bar{Q}_{ij} = K_j \bar{P}_i$$

It can be easily seen that (2.3.16) holds.

$$[A_j \bar{P}_i + B_j \bar{Q}_{ij}]_s + \sum_{r \neq z}^{m} |\phi_r| \epsilon(\lambda+1) \bar{P}_i \bar{P}_i < 0 \qquad (2.3.16)$$

According to Schur complement, (2.3.16) is equal to (2.3.6). Therefore, if (2.3.16) holds, $\dot{V}(x(t)) < 0$, $\forall x(t) \neq 0$. By noting that model-dependent state-feedback gain matrix K_j can be recovered from matrices $\bar{P}_i$ and $\bar{Q}_{ij}$,

$$K_j = \bar{Q}_{ij} \bar{P}_i^{-1} \qquad (2.3.17)$$

This completes the proof. $\qquad \qquad \square$

Remark 2.2 : *The conditions in Theorem 2.4 are LMIs if ϵ and λ are given. Besides, the upper-bounds of time-derivatives of $\sigma_i(x_\sigma^i(t))$ cannot always be estimated from the state and control-input. The model-dependent state-feedback stabilization scheme is applicable only for the case where ϕ_i can be estimated from the states and control-input. The case will be illustrated by a design example of Chua's oscillator later.*

If all the model-dependent state-feedback gain matrices K_i are the same in Theorem 2.4(i.e., $K_i = K_j = K$, $\forall i, j \in S$), then model-dependent state-feedback controller will reduce to static state-feedback controller (i.e., $u_i(t) \triangleq u(t) = Kx(t)$, $\forall i \in S$).

There exist $m - 1$ additional free variables in model-dependent state-feedback controller design approach with respect to static state-feedback controller. It means that Theorem 2.4 has the advantage of robust performance to suppress the perturbation of uncertain parameters and ensure the stability of the corresponding closed-loop system, which will be illustrated by a numerical example later.

2.4 Simulation examples

In this section, a numerical example of linear system with state-dependent uncertainties is first presented to demonstrate the advantages of the robust stability conditions in Theorem 2.2 and Theorem 2.3 with respect to Theorem 2.1. Then, an example of Chua's oscillator is provided to demonstrate necessity of our proposed system model and the applicability of our developed controller design approach in Theorem 2.4. All of the results of this section are attained by using MATLAB-based toolbox YALMIP [94] and the solver SDPT3 [95] for solving LMIs.

2.4.1 Example 1: stability analysis

Consider the continuous-time uncertain system with state dependent uncertainties, described by:

$$
\begin{bmatrix} \dot{x}_1(t) \\ \dot{x}_2(t) \end{bmatrix} =
$$

$$
\begin{bmatrix} -3.5 + 0.25(\sin(x_1(t)) + \sin(x_2(t))) \\ 0.5(\beta-1)+0.15(\beta+1)(\sin(x_1(t))+\sin(x_2(t))) \end{bmatrix}
$$

$$
\begin{bmatrix} & -1 \\ 0.5(\alpha-2)-0.1(\alpha+2)(\sin(x_1(t))+\sin(x_2(t))) \end{bmatrix} \begin{bmatrix} x_1(t) \\ x_2(t) \end{bmatrix} \tag{2.4.1}
$$

where β and α are the system parameters. The above system can be described in the

form of (2.1.5)

$$\dot{x}(t) = \sum_{i=1}^{4} \sigma_i(x_\sigma^i(t))A_i x(t)$$

where

$$\sigma_1(x_\sigma^1(t)) = 0.25 - 0.25\sin(x_2(t)),$$

$$\sigma_2(x_\sigma^2(t)) = 0.25 + 0.25\sin(x_2(t)),$$

$$\sigma_3(x_\sigma^3(t)) = 0.25 - 0.25\sin(x_1(t)),$$

$$\sigma_4(x_\sigma^4(t)) = 0.25 + 0.25\sin(x_1(t)),$$

$$A_1 = \begin{bmatrix} -5 & -4 \\ -1 & \alpha \end{bmatrix}, A_2 = \begin{bmatrix} -4 & -4 \\ 0.6\beta - 0.4 & 0.6\alpha - 0.8 \end{bmatrix}$$

$$A_3 = \begin{bmatrix} -3 & -4 \\ 0.4\beta - 0.6 & 0.4\alpha - 1.2 \end{bmatrix}, A_4 = \begin{bmatrix} -2 & -4 \\ \beta & -2 \end{bmatrix}$$

The stability of system (2.4.1) is verified for several values of system parameters, comprising $\alpha \times \beta \in [-20, 0] \times [100, 200]$. Consider the time derivative of uncertain parameter

$$\dot{\sigma}_1(x_\sigma^1(t)) = \frac{\partial \sigma_1(x_\sigma^1(t))}{\partial x_2(t)} \dot{x}_2(t)$$

By substituting

$$\dot{x}_2(t) = \begin{bmatrix} 0 & 1 \end{bmatrix} \times \sum_{i=1}^{4} \sigma_i(x_\sigma^i(t))A_i x(t)$$

into $\dot{\sigma}_1(x_\sigma^1(t))$, we can obtain

$$\phi_1 = \max_{-\frac{\pi}{40} < x_1 < \frac{\pi}{40}, -\frac{\pi}{40} < x_2 < \frac{\pi}{40}} \dot{\sigma}_1(x_\sigma^1(t))$$

under the assumption $x_1(t) \in [-\frac{\pi}{40} \ \frac{\pi}{40}]$, $x_2(t) \in [-\frac{\pi}{40} \ \frac{\pi}{40}]$ for the given parameters α, β. Parameters ϕ_2, ϕ_3, and ϕ_4 can be obtained in the same way.

Comparison results are depicted in Fig.2.1 respectively. Cross indicates that the stability can be testified out by Theorem 2.2, whereas traditional quadratic Lyapunov function with constant matrix P in Theorem 2.1 is infeasible, meanwhile dot denotes that the stability can be testified out by Theorem 2.3, whereas Theorem 2.2 is infeasible. Fur-
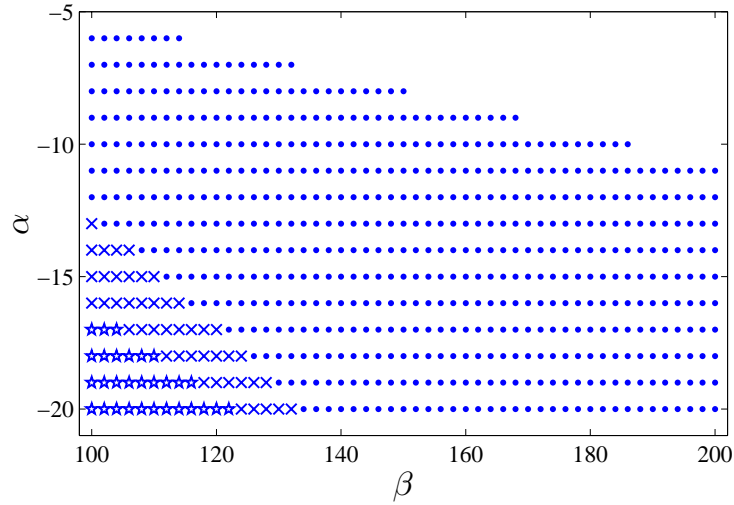
Fig. 2.1: Stability analysis with the most traditional quadratic Lyapunov function with constant matrix P (☆) and Theorem 2.2 (☆ and ×) and with Theorem 2.3 (☆, × and ●) under assumption $x_1(t) \in [-\frac{\pi}{40} \ \frac{\pi}{40}]$, $x_2(t) \in [-\frac{\pi}{40} \ \frac{\pi}{40}]$.

thermore, take $[\alpha \ \beta] = [-14 \ 100]$ and $[\alpha \ \beta] = [-20 \ 200]$ in Fig. 2.1 for examples. State responses of the underlying system with corresponding parameters $[\alpha \ \beta] = [-14 \ 100]$ and $[\alpha \ \beta] = [-20 \ 200]$ for initial condition $x(0) = [-\frac{\pi}{200} \ \frac{\pi}{200}]^T$ are depicted in Fig. 2.3 and Fig. 2.4 respectively. It can be seen from Fig. 2.3 and Fig. 2.4 that the systems with corresponding parameters are stable. Based on the above discussions, we can conclude that Theorem 2.2 promotes a larger stability margin than Theorem 2.1, and the conservativeness is further reduced in Theorem 2.3. However, opposite occurs for some specific sets of parameters, e.g., ϕ_i, $i \in S$. This is exactly what will be presented in the following.

For $x_1(t) \in [-\frac{\pi}{2} \ \frac{\pi}{2}]$, $x_2(t) \in [-\frac{\pi}{2} \ \frac{\pi}{2}]$, repeating system (2.4.1) with Theorem 2.1, Theorem 2.2 and Theorem 2.3. Stability analysis results are depicted in Fig.2.2. Note that the stable margins of Theorem 2.2 are empty, do not include that from the Theorem 2.1. It means that the stability condition of Theorem 2.2 failed to search the stability region in this case. However, results of Theorem 2.3 not only contain the results of the most traditional quadratic Lyapunov function approach with constant matrix P completely, but also expand the stability margins with a larger stability region.

Difference between previous example and this one is that the concerned system state
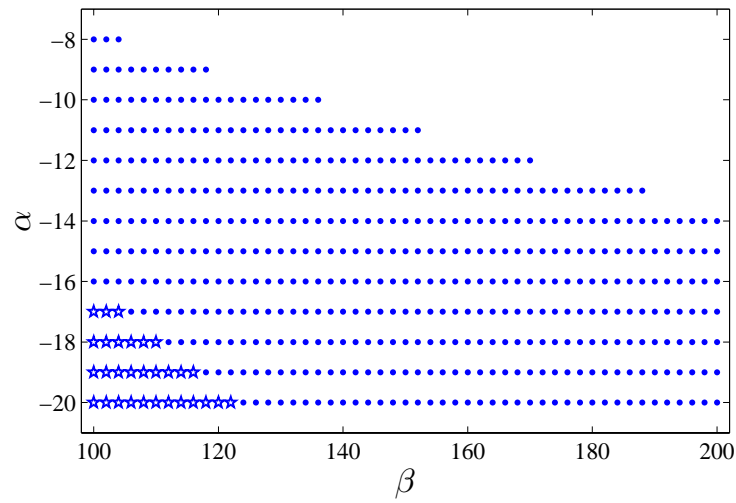
Fig. 2.2: Stability analysis with the most traditional quadratic Lyapunov function with constant matrix P (☆) and Theorem 2.2 ($\times$) and with Theorem 2.3 (☆, $\times$ and ●) under assumption $x_1(t) \in [-\frac{\pi}{2} \ \frac{\pi}{2}]$, $x_2(t) \in [-\frac{\pi}{2} \ \frac{\pi}{2}]$.
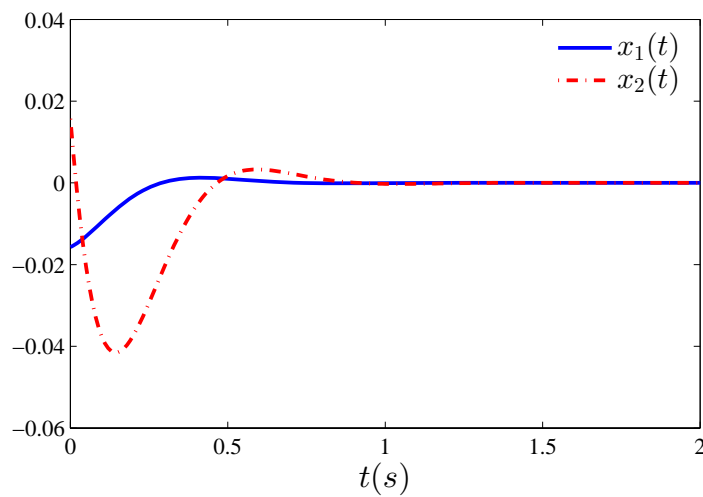
Fig. 2.3: State response of the underlying system for given parameters $[\alpha \ \beta] = [-14 \ 100]$.
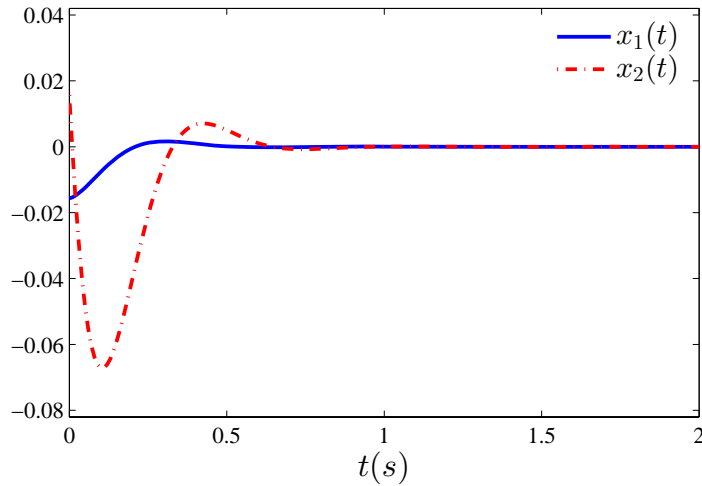
Fig. 2.4: State response of the underlying system for given parameters $[\alpha \ \beta] = [-20 \ 200]$.

ranges from $x_1(t) \in [-\frac{\pi}{40} \ \frac{\pi}{40}]$, $x_2(t) \in [-\frac{\pi}{40} \ \frac{\pi}{40}]$ to $x_1(t) \in [-\frac{\pi}{2} \ \frac{\pi}{2}]$, $x_2(t) \in [-\frac{\pi}{2} \ \frac{\pi}{2}]$, which leads to the variation of parameters ϕ_i, $i \in S$. Upper bounds of the time-derivatives of the uncertain parameters $\sigma_i(x_\sigma^i(t))$, $i \in S$ increase as the concerned system state regions become larger. Finally, we can conclude that Theorem 2.3 can provide a less conservative version of Theorem 2.2 by utilizing a property of the time-derivatives of uncertain parameters. This result shows the advantage of parameter-dependent Lyapunov functions proposed in (2.1.6).

2.4.2 Example 2: Chua's oscillator

In this example, we consider the problems of stabilization and synchronization of Chua's oscillator, which has wide applications in secure communication systems and power electronic systems. Consider a Chua's oscillator in Fig.2.5 borrowed from Reference [96]. It consists of three linear energy storage elements (inductor L, capacitor C_1 and capacitor C_2), two linear resistors (resistor R_L and resistor R_E) and a special nonlinear Chua's diode D. According to the Kirchhoff's voltage law and current law, the above Chua's
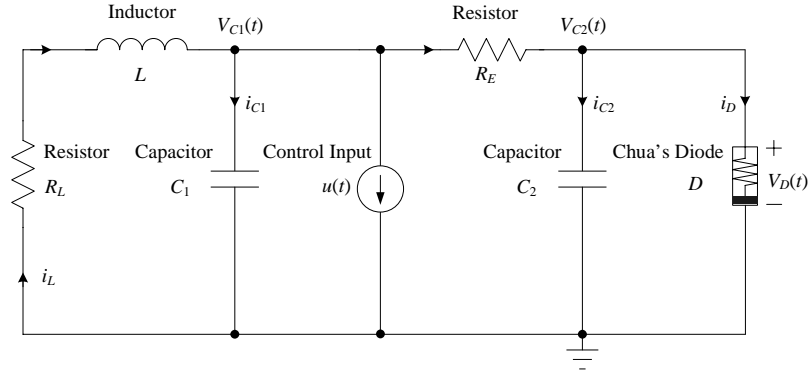
Fig. 2.5: A Chua's oscillator circuit

oscillator is characterized by

$$\begin{cases} C_1 \dfrac{dV_{C1}(t)}{dt} = -\dfrac{V_{C1}(t) - V_{C2}(t)}{R_E} + i_L(t) - u(t) \\ C_2 \dfrac{dV_{C2}(t)}{dt} = \dfrac{V_{C1}(t) - V_{C2}(t)}{R_E} - i_D(t) \\ L \dfrac{di_L(t)}{dt} = -V_{C1}(t) - R_L i_L(t) \end{cases}$$

where independent current source $u(t)$ is the control input, $i_L(t)$ is the current through the inductor L; $V_{C_1}(t)$, $V_{C_2}(t)$ are the voltages across the capacitors C_1, C_2 respectively, $i_D(t)$ is the current through the Chua's diode D, which is uncertain and depends non-linearly on the $V_D(t)$ [96]. Here, suppose that

$$i_D = l_1 V_D(t) + l_2 V_D^2(t) + l_3 V_D^3(t)$$

Let $x_1(t) = V_{C_1}(t)$, $x_2(t) = V_{C_2}(t)$ and $x_3(t) = i_L(t)$ be the state variables, then the Chua's oscillator can be expressed by the following state-space equation:

$$\begin{bmatrix} \dot{x}_1(t) \\ \dot{x}_2(t) \\ \dot{x}_3(t) \end{bmatrix} = \begin{bmatrix} \frac{-1}{R_E C_1} & \frac{1}{R_E C_1} & \frac{1}{C_1} \\ \frac{1}{R_E C_2} & [\frac{-1}{R_E C_2} - \frac{1}{C_2}(l_1 + l_2 x_2(t) + l_3 x_2^2(t))] & 0 \\ -\frac{1}{L} & 0 & -\frac{R_L}{L} \end{bmatrix}$$
$$\begin{bmatrix} x_1(t) \\ x_2(t) \\ x_3(t) \end{bmatrix} + \begin{bmatrix} -\frac{1}{C_1} \\ 0 \\ 0 \end{bmatrix} u(t)$$

Then, we consider the Chua's oscillator with the following parameters: $C_1 = 1.0\ F$, $C_2 = 0.1\ F$, $R_E = 0.7\ \Omega$, $R_L = 0.01\ \Omega$, $L = 70\ mH$, $l_1 = -8/7$, $l_2 = -1/100$, $l_3 = 2/7$. Without control input, responses of open-loop Chua's oscillator are depicted in Fig. 2.6 with initial condition $x(0) = [-0.1\ -0.1\ 0.1]^T$, from which oscillatory behavior of Chua's oscillator can be observed. As we can see in Fig. 2.7, system states approach a stable limit-cycle approximating a circle at the origin.
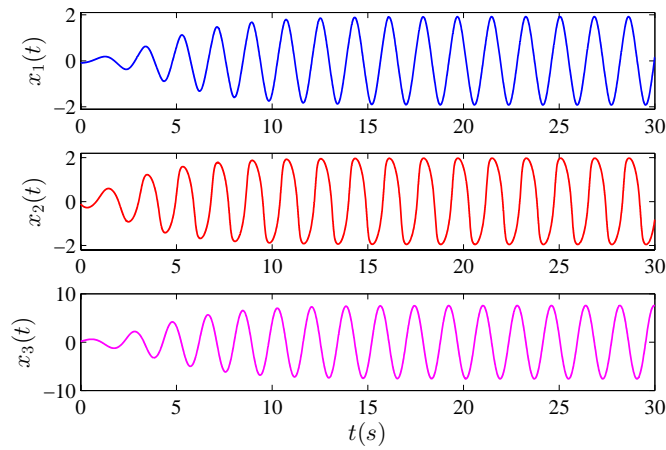
Fig. 2.6: State responses of the open-loop Chua's oscillator with initial condition $x(0) = \begin{bmatrix} -0.1 & -0.1 & 0.1 \end{bmatrix}^T$
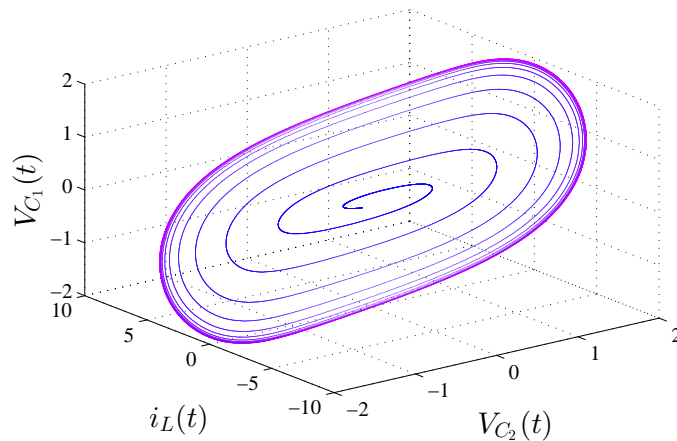
Fig. 2.7: 3-D stable limit-cycle

Without sacrificing the generality, assume that $V_{C_1}(t) \in [-6,\ 6]\ V$, $V_{C_2} \in [-6,\ 6]\ V$.

Therefore, above Chua's oscillator can be rewritten in a polytopic form of system (2.1.5)

$$\dot{x}(t) = \sum_{i=1}^{4} \sigma_i(x_\sigma^i(t))[A_i x(t) + B_i u(t)]$$

where $x(t) = [x_1(t)\ x_2(t)\ x_3(t)]^T$, $\sigma_1(x_\sigma^1(t)) = \frac{1}{24}x_2(t) + \frac{1}{4}$, $\sigma_2(x_\sigma^2(t)) = -\frac{1}{24}x_2(t) + \frac{1}{4}$, $\sigma_3(x_\sigma^3(t)) = -\frac{1}{72}x_2^2(t)+\frac{1}{2}$ and $\sigma_4(x_\sigma^4(t)) = \frac{1}{72}x_2^2(t)$, $(0 \leq \sigma_1(x_\sigma^1(t)),\sigma_2(x_\sigma^2(t)),\ \sigma_3(x_\sigma^3(t)),\sigma_4(x_\sigma^4(t)) \leq 1,\sigma_1(x_\sigma^1(t)) + \sigma_2(x_\sigma^2(t)) + \sigma_3(x_\sigma^3(t)) + \sigma_4(x_\sigma^4(t)) = 1)$ represent the uncertain parameter vector; A_i and B_i $(i \in S)$ are the vertices of the corresponding uncertainty polytope. Therefore, it arrives at

$$A_1 = \begin{bmatrix} -\frac{10}{7} & \frac{10}{7} & 1 \\ \frac{100}{7} & -\frac{58}{35} & 0 \\ -\frac{100}{7} & 0 & -\frac{1}{7} \end{bmatrix}, A_2 = \begin{bmatrix} -\frac{10}{7} & \frac{10}{7} & 1 \\ \frac{100}{7} & -\frac{142}{35} & 0 \\ -\frac{100}{7} & 0 & -\frac{1}{7} \end{bmatrix},$$

$$A_3 = \begin{bmatrix} -\frac{10}{7} & \frac{10}{7} & 1 \\ \frac{100}{7} & -\frac{20}{7} & 0 \\ -\frac{100}{7} & 0 & -\frac{1}{7} \end{bmatrix}, A_4 = \begin{bmatrix} -\frac{10}{7} & \frac{10}{7} & 1 \\ \frac{100}{7} & -\frac{1460}{7} & 0 \\ -\frac{100}{7} & 0 & -\frac{1}{7} \end{bmatrix},$$

$$B_1 = B_2 = B_3 = B_4 = \begin{bmatrix} -1 & 0 & 0 \end{bmatrix}^T$$

1.*Chua's Oscillator Stabilization*

Oscillatory phenomenon is conventionally considered unacceptable for engineering applications, largely because their performance seems unpredictable and unquantifiable, which deteriorates the system performance and leads to system instability, especially in power electronic systems [97]. Therefore, we aim at designing a model-dependent state-feedback controller based on the approach proposed in Theorem 2.4 to suppress the oscillatory behavior of Chua's circuit in Fig. 2.5.

Consider the time derivative of uncertain parameter

$$\dot{\sigma}_i(x_\sigma^i(t)) = \frac{\partial \sigma_i(x_\sigma^i(t))}{\partial x_2(t)} \dot{x}_2(t)$$

By substituting

$$
\begin{aligned}
\dot{x}_2(t) &= \begin{bmatrix} 0 & 1 & 0 \end{bmatrix} \times \sum_{i=1}^{4} \sigma_i(x_\sigma^i(t))[A_i x(t) + B_i u(t)] \\
&= \begin{bmatrix} 0 & 1 & 0 \end{bmatrix} \times \sum_{i=1}^{4} \sigma_i(x_\sigma^i(t)) A_i x(t)
\end{aligned}
$$

into $\dot{\sigma}_i(x_\sigma^i(t))$, we can obtain

$$
\phi_i = \max_{-6 < x_1, x_2 < 6} \dot{\sigma}_i(x_\sigma^i(t))
$$

$\phi_1 = 30.1500$, $\phi_2 = 29.8500$, $\phi_3 = 120.6000$, $\phi_4 = 3.1862$. Model-dependent state-feedback controller is designed by applying the stabilization approach in Theorem 2.4, and computational time for this example in computer (PC with Intel Core2 processors @2.20GHz @2.20GHz and 3.0 GB DDR2 of memory) is less than 5.95 seconds.

$$
K_1 = \begin{bmatrix} -1.5095 & 63.0684 & -10.2284 \end{bmatrix}
$$

$$
K_2 = \begin{bmatrix} -1.5078 & 62.9542 & -10.2285 \end{bmatrix}
$$

$$
K_3 = \begin{bmatrix} -1.5087 & 63.0113 & -10.2284 \end{bmatrix}
$$

$$
K_4 = \begin{bmatrix} -1.1253 & 53.2145 & -10.2387 \end{bmatrix}
$$

By noting that $B_i = B_j = B(\sigma(x(t))), \forall i, j \in S$ in this example. According to the property in (2.3.4), model-dependent state-feedback controller $K(x(t))$ can be reduced to the following form

$$
\begin{aligned}
K(x(t)) &= \sum_{i=1}^{4} \sigma_i(x_\sigma^i(t)) K_i \\
&= \begin{bmatrix} 0.0053 x_2^2(t) - 0.0001 x_2(t) - 1.5086 \\ -0.1361 x_2^2(t) + 0.0048 x_2(t) + 63.011 \\ -0.0001 x_2^2(t) - 10.2284 \end{bmatrix}^T
\end{aligned}
$$

Assume that the maximize current supplied by current source $u(t)$ is less than 10 A, i.e., $|u(t)| \leq 10$. Fig. 2.8 and Fig. 2.9 depict the control input signal and state response of closed-loop Chua's oscillator respectively, where controller is activated at $t \geq 20$. By

comparing result in Fig. 2.6 with that in Fig. 2.9, it is clear that the model-dependent state-feedback controller can asymptotically stabilize the underlying system with a good performance.
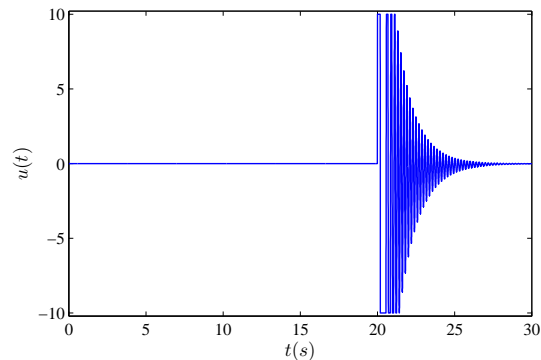
Fig. 2.8: Control input of closed-loop Chua's oscillator. Controller is activated at $t \geq 20$.
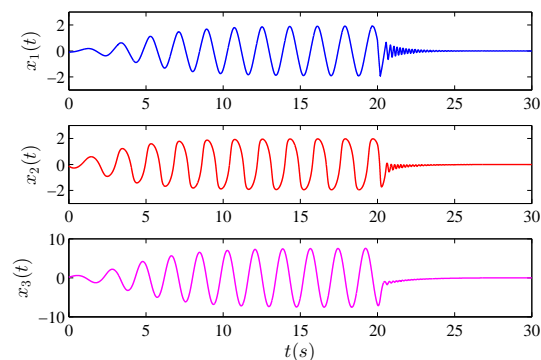
Fig. 2.9: State response of closed-loop Chua's oscillator with initial condition $x(0) = \begin{bmatrix} -0.1 & -0.1 & 0.1 \end{bmatrix}^T$

2.Chua's Oscillator Synchronization

Then, consider the synchronization problem for two identical Chua's Oscillators with different initial conditions.

$$\dot{x}(t) = f(x(t))$$
$$\dot{\tilde{x}}(t) = f(\tilde{x}(t)) + Bu(t)$$

where $u(t)$ is the input of synchronization controller implemented by a controlled current source, $\dot{x}(t) = f(x(t))$ is the driving or master system and $\dot{\tilde{x}}(t) = f(\tilde{x}(t))$ is the response

or slave system. By introducing the error variables $e_1 = \tilde{x}_1 - x_1$, $e_2 = \tilde{x}_2 - x_2$, $e_3 = \tilde{x}_3 - x_3$, the error dynamical system can be expressed as

$$
\begin{bmatrix} \dot{e}_1(t) \\ \dot{e}_2(t) \\ \dot{e}_3(t) \end{bmatrix} = \begin{bmatrix} -\frac{1}{R_E C_1} & \frac{1}{R_E C_1} & \frac{1}{C_1} \\ \frac{1}{R_E C_2} & [-\frac{1}{R_E C_2} - \frac{1}{C_2} g(x_2(t), \tilde{x}_2(t))] & 0 \\ -\frac{1}{L} & 0 & -\frac{R_L}{L} \end{bmatrix}
$$
$$
\begin{bmatrix} e_1(t) \\ e_2(t) \\ e_3(t) \end{bmatrix} + \begin{bmatrix} -\frac{1}{C_1} \\ 0 \\ 0 \end{bmatrix} u(t)
$$

where

$$
g(x_2(t), \tilde{x}_2(t)) = l_1 + l_2[x_2(t) + \tilde{x}_2(t)] + l_3[x_2^2(t) + x_2(t)\tilde{x}_2(t) + \tilde{x}_2^2(t)]
$$

is the nonlinear or uncertain part of the error dynamical system. The problem of synchronization between the two identical Chua's oscillators can be translated into a problem of how to realize the asymptotical stabilization of the error dynamical system at origin. Therefore, the goal is to design a controller $u(t)$ such that $\lim_{t\to\infty} \|e(t)\| = 0$, $e(t) = [e_1(t) \ e_2(t) \ e_3(t)]^T$. Consider two identical Chua's oscillators with the same parameters as that in the previous example. Error dynamical system mentioned above can be rewritten in a polytopic form of system (2.1.5)

$$
\dot{e}(t) = \sum_{i=1}^{4} \sigma_i(x_2(t), \tilde{x}_2(t))[A_i e(t) + B_i u(t)]
$$

where $\sigma_i(x_2(t), \tilde{x}_2(t))$ is the uncertain parameter depending on system state variables $x_2(t)$ and $\tilde{x}_2(t)$,

$$
\sigma_1(x_2(t), \tilde{x}_2(t)) = \frac{1}{48}[x_2(t) + \tilde{x}_2(t)] + \frac{1}{4}
$$
$$
\sigma_2(x_2(t), \tilde{x}_2(t)) = \frac{-1}{48}[x_2(t) + \tilde{x}_2(t)] + \frac{1}{4}
$$
$$
\sigma_3(x_2(t), \tilde{x}_2(t)) = \frac{-1}{216}[x_2^2(t) + x_2(t)\tilde{x}_2(t) + \tilde{x}_2^2(t)] + \frac{1}{2}
$$
$$
\sigma_4(x_2(t), \tilde{x}_2(t)) = \frac{1}{216}[x_2^2(t) + x_2(t)\tilde{x}_2(t) + \tilde{x}_2^2(t)]
$$

$(0 \leq \sigma_1(x_2(t), \tilde{x}_2(t)), \sigma_2(x_2(t), \tilde{x}_2(t)), \sigma_3(x_2(t), \tilde{x}_2(t)),\ \sigma_4(x_2(t), \tilde{x}_2(t)) \leq 1, \sigma_1(x_2(t), \tilde{x}_2(t)) +$
$\sigma_2(x_2(t), \tilde{x}_2(t)) + \sigma_3(x_2(t), \tilde{x}_2(t)) + \sigma_4(x_2(t), \tilde{x}_2(t)) = 1)$; A_i and B_i $(i \in S)$ are the vertices
of the corresponding uncertainty polytope.

$$A_1 = \begin{bmatrix} -\frac{10}{7} & \frac{10}{7} & 1 \\ \frac{100}{7} & -\frac{16}{35} & 0 \\ -\frac{100}{7} & 0 & -\frac{1}{7} \end{bmatrix}, A_2 = \begin{bmatrix} -\frac{10}{7} & \frac{10}{7} & 1 \\ \frac{100}{7} & -\frac{184}{35} & 0 \\ -\frac{100}{7} & 0 & -\frac{1}{7} \end{bmatrix},$$

$$A_3 = \begin{bmatrix} -\frac{10}{7} & \frac{10}{7} & 1 \\ \frac{100}{7} & -\frac{20}{7} & 0 \\ -\frac{100}{7} & 0 & -\frac{1}{7} \end{bmatrix}, A_4 = \begin{bmatrix} -\frac{10}{7} & \frac{10}{7} & 1 \\ \frac{100}{7} & -620 & 0 \\ -\frac{100}{7} & 0 & -\frac{1}{7} \end{bmatrix},$$

$$B_1 = B_2 = B_3 = B_4 = \begin{bmatrix} -1 & 0 & 0 \end{bmatrix}^T$$

Consider the time derivative of uncertain parameter

$$\dot{\sigma}_i(x_2(t), \tilde{x}_2(t)) = \frac{\partial \sigma_i(x_2(t), \tilde{x}_2(t))}{\partial x_2(t)} \dot{x}_2(t) + \frac{\partial \sigma_i(x_2(t), \tilde{x}_2(t))}{\partial \tilde{x}_2(t)} \dot{\tilde{x}}_2(t)$$

By substituting

$$\dot{x}_2(t) = \begin{bmatrix} 0 & 1 & 0 \end{bmatrix} \times \sum_{i=1}^{4} \sigma_i(x_\sigma^i(t)) A_i x(t)$$

$$\dot{\tilde{x}}_2(t) = \begin{bmatrix} 0 & 1 & 0 \end{bmatrix} \times \sum_{i=1}^{4} \sigma_i(\tilde{x}_\sigma^i(t))[A_i \tilde{x}(t) + B_i u(t)]$$

$$= \begin{bmatrix} 0 & 1 & 0 \end{bmatrix} \times \sum_{i=1}^{4} \sigma_i(\tilde{x}_\sigma^i(t)) A_i \tilde{x}(t)$$

into $\dot{\sigma}_i(x_2(t), \tilde{x}_2(t))$, we can obtain

$$\phi_i = \max_{-6 < x_1, x_2 < 6;\ -6 < \tilde{x}_1, \tilde{x}_2 < 6} \dot{\sigma}_i(x_2(t), \tilde{x}_2(t))$$

$\phi_1 = 30.1500$, $\phi_2 = 29.8500$, $\phi_3 = 120.6000$, $\phi_4 = 3.1862$. Synchronization controller
is obtained by applying the stabilization approach in Theorem 2.4, and computational
time for this example in computer (PC with Intel Core2 processors @2.20GHz @2.20GHz

and 3.0 GB DDR2 of memory) is less than 3.89 seconds.

$$K_1 = \begin{bmatrix} 3.7240 & 248.2100 & -7.7791 \end{bmatrix}$$

$$K_2 = \begin{bmatrix} 3.7549 & 249.8049 & -7.7783 \end{bmatrix}$$

$$K_3 = \begin{bmatrix} 3.7394 & 249.0075 & -7.7787 \end{bmatrix}$$

$$K_4 = \begin{bmatrix} 7.9557 & 454.1497 & -7.6821 \end{bmatrix}$$

According to the property in (2.3.4), synchronization controller $K(x(t))$ can be reduced to the following form

$$K(x(t)) = \sum_{i=1}^{4} \sigma_i(x_2(t), \tilde{x}_2(t)) K_i =$$

$$\begin{bmatrix} 0.0195x_2^2(t) + 0.0195x_2(t)\tilde{x}_2(t) + 0.0195\tilde{x}_2^2(t) + 3.7394 \\ 0.9497x_2^2(t) + 0.9497x_2(t)\tilde{x}_2(t) + 0.9497\tilde{x}_2^2(t) + 249.01 \\ 0.0004x_2^2(t) + 0.0004x_2(t)\tilde{x}_2(t) + 0.0004\tilde{x}_2^2(t) - 7.7787 \end{bmatrix}^T$$

Assume that the maximize current supplied by current source $u(t)$ is less than 10 A, i.e., $|u(t)| \leq 10$. The performance of synchronization control is illustrated with the initial conditions being $x(0) = [-0.1 \ -0.1 \ 0.1]^T$ for driving system and $\tilde{x}(0) = [0.1 \ 0.1 \ -0.1]^T$ for response system. Synchronization process between the driving oscillator and response oscillator is depicted in Fig. 2.10, where synchronization controller is activated at $t \geq 20$. Fig. 2.11 depicts the control input behavior where at first there are some slight peaks ar $t \geq 20$, but when the synchronization error is closer to zero, the control signal reduces. The final convergence of synchronization error can be observed in Fig. 2.12. The model-dependent synchronization controller indeed stabilizes the error dynamical system.
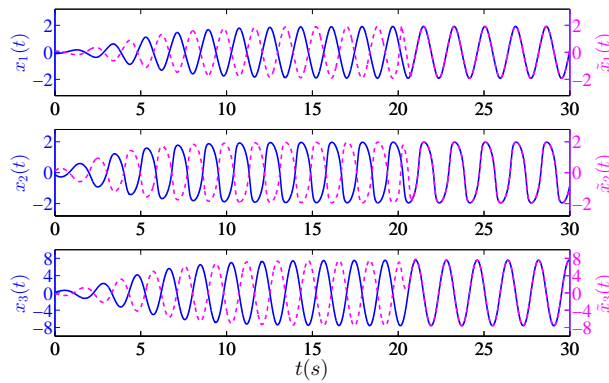
Fig. 2.10: Synchronization performance of two identical Chua's oscillator with initial conditions $x(0) = [\ -0.1\quad -0.1\quad 0.1\ ]^T$, $\tilde{x}(0) = [\ 0.1\quad 0.1\quad -0.1\ ]^T$ and synchronization controller is activated at $t \geq 20$. Driving oscillator in full lines; response oscillator in dashed lines.
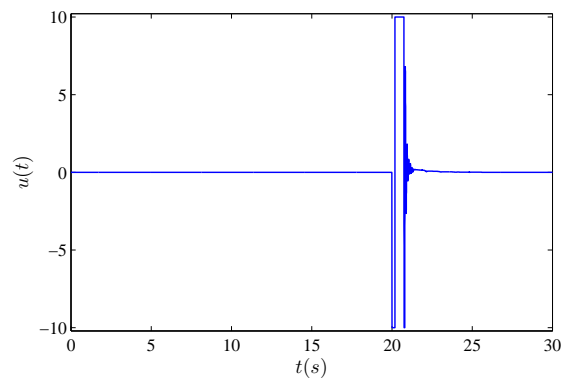
Fig. 2.11: Control input of synchronization controller. Synchronization controller is activated at $t \geq 20$.
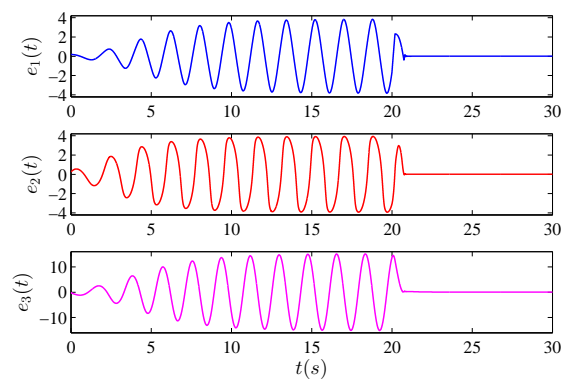
Fig. 2.12: Synchronization error signals. Synchronization controller is activated at $t \geq 20$.

2.5 Concluding remarks

This chapter has considered the problems of robust control for a class continuous time systems involving state-dependent uncertain parameters via constructing a new parameter dependent Lyapunov function. Based on the parameter dependent Lyapunov approach, stability conditions for uncertain open-loop systems are given. Furthermore, some improved stability conditions are established by utilizing the property of time-derivatives of uncertain parameters. Then, a model-dependent state-feedback stabilization scheme, which has more flexibilities in controller synthesis and can achieve better system performances in practice, is presented. The model-dependent state-feedback controller contains the static state-feedback controller as a special case. A numerical example is provided to illustrate the effectiveness of the proposed approaches. Finally, the developed controller design methodology is applied to stabilization and synchronization of Chua's oscillator, which has wide applications in secure communication systems and power electronic systems.

3 Robust filter design for state-dependent uncertain systems

This chapter considers the problem of robust filter design for continuous-time uncertain system with state-dependent uncertainties, taking the $\mathcal{D}$ stability constraints into consideration, based on a new performance index. Initially, a novel model is presented to describe such dynamic systems, which contain not only the general time-varying parameters uncertainties, but also the state-dependent uncertainties, even the couplings of both. And corresponding robust filter is also given. Then, the new performance index, which contains the H_∞, $L_2 - L_\infty$, passive and dissipative performance indices as special cases, is introduced. Furthermore, a novel type of robust model-independent filter for the considered systems is developed such that the corresponding filtering error system can guarantee the prescribed H_∞, $L_2 - L_\infty$, passive and dissipative performance levels with $\mathcal{D}$ stability constraints. Consequently, the robust filter can be designed in terms of solutions to a set of convex optimization problems. In addition, it is worth pointing out that the model-independent filter proposed in this thesis does not require that the model information is accessible for the filter design. Finally, a numerical example of tunnel diode circuit system is presented to demonstrate the applicability and effectiveness of the proposed robust filter design method.

The remainder of this chapter is structured as follows. Section 3.1 starts with problem formulation and preliminaries about robust filter design and introduces a generalized filtering performance index. In Section 3.2, robust filter design method based on convex optimization techniques is developed. Section 3.3 addresses the small current estimation

problem of a tunnel diode circuit system by resorting to the proposed robust filter design method. Finally, Section 3.4 concludes the chapter.

3.1 Problem formulation and preliminaries

Consider the following continuous-time uncertain system with state-dependent uncertainties:

$$
\begin{cases}
\dot{x}(t) = A(\sigma(x(t), \lambda(t)))x(t) + B(\sigma(x(t), \lambda(t)))w(t) \\
z(t) = C(\sigma(x(t), \lambda(t)))x(t) + D(\sigma(x(t), \lambda(t)))w(t) \\
y(t) = E(\sigma(x(t), \lambda(t)))x(t) + F(\sigma(x(t), \lambda(t)))w(t)
\end{cases}
\tag{3.1.1}
$$

where $x(t) \in \mathbb{R}^{n_x}$ is the system state; $w(t) \in \mathbb{R}^{n_w}$ is the disturbance input which belongs to $\mathcal{L}_2[0, \infty)$; $y(t) \in \mathbb{R}^{n_y}$ is the measured output; $z(t) \in \mathbb{R}^{n_z}$ is the signal to be estimated; $\sigma(x(t), \lambda(t)) \in \mathbb{R}^m$ is the uncertain parameter vector, including the normal time-varying parameters uncertainties $\lambda(t) \in \mathbb{R}^{n_\lambda}$ and the unknown state-dependent parametric perturbations; System matrices $A(\sigma(x(t), \lambda(t)))$, $B(\sigma(x(t), \lambda(t)))$, $C(\sigma(x(t), \lambda(t)))$, $D(\sigma(x(t), \lambda(t)))$, $E(\sigma(x(t), \lambda(t)))$ and $F(\sigma(x(t), \lambda(t)))$ belong to the following convex polytopic sets:

$$
\mathcal{X} = \left\{ X(\sigma(x(t), \lambda(t))) \Big| X(\sigma(x(t), \lambda(t))) = \right.
$$
$$
\left. \sum_{i=1}^m \sigma_i(x^i(t), \lambda^i(t))X_i, X_i \in \{A_i, B_i, C_i, D_i, E_i, F_i\} \right\}
\tag{3.1.2}
$$

where A_i, B_i, C_i, D_i, E_i and F_i ($i \in \mathcal{S} := \{1, 2, ..., m\}$) are vertices of the corresponding uncertainty polytope, which are known real constant matrices with appropriate dimensions; In addition, $x^i(t)$ is a vector whose entries are elements of $x(t)$; $\lambda^i(t)$ is a vector whose entries are elements of $\lambda(t)$; $\sigma_i(x^i(t), \lambda^i(t))$ is the complement of uncertain parameter vector, which satisfies the following properties:

$$
\sigma_i(x^i(t), \lambda^i(t)) > 0, \ \sum_{i=1}^m \sigma_i(x^i(t), \lambda^i(t)) = 1
\tag{3.1.3}
$$

Any continuous-time uncertain system with state-dependent uncertainties in the form of (3.1.1) can be expressed in the following more convenient form:

$$
\begin{cases}
\dot{x}(t) = \sum_{i=1}^{m} \sigma_i(x^i(t), \lambda^i(t))[A_i x(t) + B_i w(t)] \\
z(t) = \sum_{i=1}^{m} \sigma_i(x^i(t), \lambda^i(t))[C_i x(t) + D_i w(t)] \\
y(t) = \sum_{i=1}^{m} \sigma_i(x^i(t), \lambda^i(t))[E_i x(t) + F_i w(t)]
\end{cases}
\tag{3.1.4}
$$

Remark 3.1 *Compared with the continuous-time uncertain system model with state-dependent polytopic uncertainties proposed in [98], not only the state-dependent polytopic uncertainties but also the general time-varying parameters uncertainties with known bounds are considered in a unified model as presented in (3.1.1).*

For system (3.1.1), consider a full-order model-dependent filter taking the following form:

$$
\begin{cases}
\dot{x}_f(t) = A_f(\sigma(x(t), \lambda(t))) x_f(t) + B_f(\sigma(x(t), \lambda(t))) y(t) \\
z_f(t) = C_f(\sigma(x(t), \lambda(t))) x_f(t)
\end{cases}
\tag{3.1.5}
$$

where $x_f(t)$ is the filter state; $z_f(t)$ is the filter output; filter system matrices $A_f(\sigma(x(t), \lambda(t)))$, $B_f(\sigma(x(t), \lambda(t)))$ and $C_f(\sigma(x(t), \lambda(t)))$ are the model-dependent matrices to be determined. It is noted that $A_f(\sigma(x(t), \lambda(t)))$, $B_f(\sigma(x(t), \lambda(t)))$ and $C_f(\sigma(x(t), \lambda(t)))$ will be denoted by constant matrices A_{fi}, B_{fi} and C_{fi}, respectively. Introduce an augmented state vector $\tilde{x}(t)$ as $\tilde{x}(t) = [x^T(t)\ x_f^T(t)]^T$. The output error is defined as $\tilde{z}(t) = z(t) - z_f(t)$. Then, the filtering error system is given by combining system (3.1.1) and filter (5.2.4) together:

$$
\begin{cases}
\dot{\tilde{x}}(t) = \tilde{A}(\sigma(x(t), \lambda(t)))\tilde{x}(t) + \tilde{B}(\sigma(x(t), \lambda(t)))w(t) \\
\tilde{z}(t) = \tilde{C}(\sigma(x(t), \lambda(t)))\tilde{x}(t) + \tilde{D}(\sigma(x(t), \lambda(t)))w(t)
\end{cases}
\tag{3.1.6}
$$

where

$$
\tilde{A}(\sigma(x(t), \lambda(t))) = \begin{bmatrix} A(\sigma(x(t), \lambda(t))) & 0 \\ B_f(\sigma(x(t), \lambda(t)))E(\sigma(x(t), \lambda(t))) & A_f(\sigma(x(t), \lambda(t))) \end{bmatrix}
$$

$$\tilde{B}(\sigma(x(t), \lambda(t))) = \begin{bmatrix} B(\sigma(x(t), \lambda(t))) \\ B_f(\sigma(x(t), \lambda(t))) F(\sigma(x(t), \lambda(t))) \end{bmatrix}$$

$$\tilde{C}(\sigma(x(t), \lambda(t))) = \begin{bmatrix} C(\sigma(x(t), \lambda(t))) & -C_f(\sigma(x(t), \lambda(t))) \end{bmatrix}$$

$$\tilde{D}(\sigma(x(t), \lambda(t))) = D(\sigma(x(t), \lambda(t)))$$

Remark 3.2 *It is worth pointing out that the model information of system (3.1.1) is assumed to be obtained in the implementation of model-dependent filters in (5.2.4). However, the model-dependent information may not always be accessible directly in some practical situations (such as the parameters' uncertainties of resistor, capacitor, and inductor in circuit systems, which maybe come from the sources: aging of the materials, constructive differences, thermal drift, disturbance, etc. In practice, it is hard to get ideal knowledge on the system uncertain parameters, or the cost is probably expensive), which will be detailedly illustrated by a simulation example of tunnel diode circuit later. Thus, the model-dependent filter in the form of (5.2.4) is no longer applicable for such cases. Note that the design approach of model-dependent filters cannot be used to construct the model-independent filters due to the coupled terms between the filter matrices and model-dependent parameters. Therefore, new approaches need to be developed to deal with the model-independent filter design problem.*

In view of Remark 3.2, we will consider the following full-order mode-independent filter for system (3.1.1) in this thesis:

$$\begin{cases} \dot{x}_f(t) = A_f x_f(t) + B_f y(t) \\ z_f(t) = C_f x_f(t) \end{cases} \tag{3.1.7}$$

where $x_f(t) \in \mathbb{R}^{n_x}$ is the filter state; $z_f(t) \in \mathbb{R}^{n_z}$ is the filter output; A_f, B_f and C_f are the model-independent constant matrices to be determined. Define $\tilde{z}(t) = z(t) - z_f(t)$ and $\tilde{x}(t) = [x^T(t) \quad x_f^T(t)]^T$. Then, the filtering error system resulting from (3.1.4) and

(3.1.7) is described by

$$
\begin{cases}
\dot{\tilde{x}}(t) = \sum_{i=1}^{m} \sigma_i(x^i(t), \lambda^i(t))[\tilde{A}_i \tilde{x}(t) + \tilde{B}_i w(t)] \\
\tilde{z}(t) = \sum_{i=1}^{m} \sigma_i(x^i(t), \lambda^i(t))[\tilde{C}_i \tilde{x}(t) + \tilde{D}_i w(t)]
\end{cases}
\tag{3.1.8}
$$

where

$$
\tilde{A}_i = \begin{bmatrix} A_i & 0 \\ B_f E_i & A_f \end{bmatrix}, \quad \tilde{B}_i = \begin{bmatrix} B_i \\ B_f F_i \end{bmatrix}
$$

$$
\tilde{C}_i = \begin{bmatrix} C_i & -C_f \end{bmatrix}, \quad \tilde{D}_i = D_i
$$

In this chapter, $\mathcal{D}$ stability constraint is imposed for the purpose of achieving expected dynamic performances for filtering error system (3.1.8). In what follows, we will consider the model-independent filter with the following $\mathcal{D}$ stability constraints lie in a circular region.

Lemma 3.1 *Let $\mho(q, r)$ denotes any circular region centering in q with radius r in the complex plane (q, $r \in R$ and $r > 0$). Then, all the eigenvalues of $\tilde{A}(\sigma(x(t), \lambda(t)))$ in filtering error system (3.1.6) lie in the region $\mho(q, r)$, if and only if there exists a symmetric matrix $P > 0$ such that*

$$
\begin{bmatrix} -P & P[\tilde{A}(\sigma(x(t), \lambda(t))) - qI] \\ \star & -r^2 P \end{bmatrix} < 0
\tag{3.1.9}
$$

Before ending this section, we recall the following assumption and definition, which will be used to develop the main results in the sequel.

Assumption 1: [99] Matrices Φ, Ψ_1, Ψ_2 and Ψ_3 satisfy the following conditions:

1) $\Phi = \Phi^T, \Psi_1 = \Psi_1^T$ and $\Psi_3 = \Psi_3^T$;

2) $\Phi \geq 0$ and $\Psi_1 \leq 0$;

3) $\|D_i\| \cdot \|\Phi\| = 0, \forall i \in \mathcal{S}$;

4) $(\|\Psi_1\| + \|\Psi_2\|)\|\Phi\| = 0$;

5) $D_i^T \Psi_1 D_i + D_i^T \Psi_2 + \Psi_2^T D_i + \Psi_3 > 0, \ \forall i \in \mathcal{S}.$

Definition 3.1 *[99] For given matrices Φ, Ψ_1, Ψ_2 and Ψ_3 satisfying Assumption 1, system (3.1.8) is said to be extended dissipative if there exits a scalar ρ such that the following inequality holds for any $t_f \geq 0$ and all $w(t) \in \mathcal{L}_2[0, \ \infty)$*

$$\int\limits_0^{t_f} J(t)dt - \tilde{z}(t_v)^T \Phi \tilde{z}(t_v) \geq \rho, \quad t_v \in [0, \ t_f] \tag{3.1.10}$$

where

$$J(t) = \tilde{z}(t)^T \Psi_1 \tilde{z}(t) + 2\tilde{z}(t)^T \Psi_2 w(t) + w(t)^T \Psi_3 w(t)$$

Remark 3.3 *The new performance index introduced in Definition 3.1 contains a few of classical performance indices as special cases. By using above new performance index, some well-known filtering problems such as H_∞, $L_2 - L_\infty$, passive and dissipative filtering problems can be solved successfully within a unified framework [99].*

1) *Let $\Phi = 0$, $\Psi_1 = -I$, $\Psi_2 = 0$, $\Psi_3 = \gamma^2 I$ and $\rho = 0$, inequality (3.1.10) reduces to H_∞ performance index [100];*

2) *Let $\Phi = I$, $\Psi_1 = 0$, $\Psi_2 = 0$, $\Psi_3 = \gamma^2 I$ and $\rho = 0$, inequality (3.1.10) becomes $L_2 - L_\infty$ (energy-to-peak) performance index [101];*

3) *If the dimension of output $\tilde{z}(t)$ is the same as that of disturbance $w(t)$, then inequality (3.1.10) with $\Phi = 0$, $\Psi_1 = 0$, $\Psi_2 = I$, $\Psi_3 = \gamma I$ and $\rho = 0$ becomes the passivity performance index [102];*

4) *Let $\Phi = 0$, $\Psi_1 = Q_0$, $\Psi_2 = S_0$, $\Psi_3 = R_0 - \tau I$ and $\rho = 0$, inequality (3.1.10) reduces to the strict (Q_0, S_0, R_0)-dissipativity [103];*

5) Let $\Phi = 0$, $\Psi_1 = -\epsilon I$, $\Psi_2 = I$, $\Psi_3 = -\tau I$ with $\varepsilon > 0$ and $\tau > 0$, the inequality (3.1.10) becomes the very-strict passivity performance index.

In the definition of the very-strict passivity, scalar ρ is not required to be zero. It was shown in [102] that ρ should be a non-positive scalar. This fact can also be verified from Assumption 1 and Definition 1. Indeed, when $w(t) = 0$, it follows from (3.1.10) that

$$\rho \leq \int_0^{t_f} \tilde{z}(t)^T \Psi_1 \tilde{z}(t) dt - \tilde{z}(t_v)^T \Phi \tilde{z}(t_v), \quad t_v \in [0,\ t_f]$$

Note from Assumption 1 that $\Phi \geq 0$ and $\Psi_1 \leq 0$. Thus, above inequality implies that $\rho \leq 0$

Then, our objective is to design a model-independent full-order filter in the form of (3.1.7) such that for all admissible uncertainties:

1) The filtering error system (3.1.8) with $w(t) = 0$ is asymptotically stable;

2) The filtering error system (3.1.8) satisfies the $\mathcal{D}$ stability constraints (3.1.9);

3) The filtering error system (3.1.8) guarantees the new performance index proposed in (3.1.10) for all nonzero $w(t) \in \mathcal{L}_2[0,\ \infty)$.

3.2 Performance criterion and filter design

In this section, the filter design problem will be considered. We first present the performance criterion for the filtering error system (3.1.8) where the filter matrices in (3.1.7) are assumed to be given.

Theorem 3.1 *Given matrices Φ, Ψ_1, Ψ_2 and Ψ_3 satisfying Assumption 1, the filtering error system (3.1.8) is asymptotically stable and satisfies the index performance in Definition 1 and the poles lie in a circular region $\mho(q, r)$ defined in Lemma 1, if there exist*

matrices $P > 0$ and $G > 0$, such that the following linear matrix inequalities (LMIs) hold, $\forall i \in \mathcal{S}$:

$$G < P \tag{3.2.1}$$

$$\Pi_i < 0 \tag{3.2.2}$$

$$\tilde{C}_i^T \Phi \tilde{C}_i < G \tag{3.2.3}$$

$$\begin{bmatrix} -P & P(\tilde{A}_i - qI) \\ \star & -r^2 P \end{bmatrix} < 0 \tag{3.2.4}$$

where

$$\Pi_i = \begin{bmatrix} [P\tilde{A}_i]_s - \tilde{C}_i^T \Psi_1 \tilde{C}_i & P\tilde{B}_i - \tilde{C}_i^T \Psi_1 \tilde{D}_i - \tilde{C}_i^T \Psi_2 \\ \star & -\tilde{D}_i^T \Psi_1 \tilde{D}_i - [\tilde{D}_i^T \Psi_2]_s - \Psi_3 \end{bmatrix}$$

and the scalar ρ involved in Definition 1 can be chosen as

$$\rho = -V(0) \tag{3.2.5}$$

Proof: Consider the following Lyapunov function:

$$V(t) = \tilde{x}(t)^T P \tilde{x}(t) \tag{3.2.6}$$

The time derivative of $V(t)$ is expressed as:

$$\begin{aligned} \dot{V}(t) &= 2\tilde{x}(t)^T P \dot{\tilde{x}}(t) \\ &= 2\sum_{i=1}^{m} \sigma_i(x^i(t), \lambda^i(t))\tilde{x}(t)^T P[\tilde{A}_i \tilde{x}(t) + \tilde{B}_i w(t)] \end{aligned} \tag{3.2.7}$$

Then, one has that

$$\dot{V}(t) - J(t) \leq \sum_{i=1}^{m} \sigma_i(x^i(t), \lambda^i(t)) \left\{ 2\tilde{x}(t)^T P[\tilde{A}_i \tilde{x}(t) + \tilde{B}_i w(t)] \right.$$

$$- [\tilde{C}_i \tilde{x}(t) + \tilde{D}_i w(t)]^T \Psi_1 [\tilde{C}_i \tilde{x}(t) + \tilde{D}_i w(t)]$$

$$\left. - 2[\tilde{C}_i \tilde{x}(t) + \tilde{D}_i w(t)]^T \Psi_2 w(t) - w(t)^T \Psi_3 w(t) \right\} \tag{3.2.8}$$

(3.2.8) can be reformulated as

$$\dot{V}(t) - J(t) \leq \eta(t)^T \sum_{i=1}^{m} \sigma_i(x^i(t), \lambda^i(t)) \Pi_i \eta(t) \tag{3.2.9}$$

where $\eta(t)^T = [\tilde{x}(t)^T \quad w(t)^T]$ and

$$\Pi_i = \begin{bmatrix} [P\tilde{A}_i]_s - \tilde{C}_i^T \Psi_1 \tilde{C}_i & P\tilde{B}_i - \tilde{C}_i^T \Psi_1 \tilde{D}_i - \tilde{C}_i^T \Psi_2 \\ \star & -\tilde{D}_i^T \Psi_1 \tilde{D}_i - [\tilde{D}_i^T \Psi_2]_s - \Psi_3 \end{bmatrix}$$

It can be seen from inequality (3.2.2) that

$$\dot{V}(t) - J(t) \leq \eta(t)^T \sum_{i=1}^{m} \sigma_i(\tilde{x}^i(t)) \Pi_i \, \eta(t) < 0 \tag{3.2.10}$$

From (3.2.2), it follows that there always exists a sufficiently small positive scalar $\mu > 0$ such that $\Pi_i < -\mu I$, which implies that

$$\dot{V}(t) - J(t) \leq -\mu \|\eta(t)\|^2 \leq -\mu \|\tilde{x}(t)\|^2 \tag{3.2.11}$$

Thus, $J(t) \geq \dot{V}(t)$ holds for any $t \geq 0$. By the Newton-Leibniz formula, one has that

$$\int_0^{t_f} J(t) dt \geq V(t_f) - V(0), \quad \forall \, t_f \geq 0 \tag{3.2.12}$$

Recalling (3.2.1) and (3.2.5), we have

$$\int_0^{t_f} J(t) dt \geq \tilde{x}(t_f)^T G \tilde{x}(t_f) + \rho \tag{3.2.13}$$

According to Definition 1, we need to prove that the following inequality holds for any

matrices Φ, Ψ_1, Ψ_2, and Ψ_3 satisfying Assumption 1:

$$\int\limits_0^{t_f} J(t)dt - \tilde{z}(t_v)^T \Phi \tilde{z}(t_v) \geq \rho, \quad t_v \in [0, \ t_f] \tag{3.2.14}$$

where t_f is any nonnegative scalar. To this end, the two cases of $\|\Phi\| = 0$ and $\|\Phi\| \neq 0$ are considered, respectively. First, for the case of $\|\Phi\| = 0$, it follows from (3.2.13) that

$$\int_0^{t_f} J(t)dt \geq \tilde{x}(t_f)^T G\tilde{x}(t_f) + \rho \geq \rho \tag{3.2.15}$$

which means (3.2.14) holds by noting that $\tilde{z}(t_v)^T \Phi \tilde{z}(t_v) = 0$ ($\|\Phi\| = 0 \Leftrightarrow \Phi = 0$). For another case of $\|\Phi\| \neq 0$, it is required that $\|\Psi_1\| + \|\Psi_2\| = 0$ and $\|D_i\| = 0$ under Assumption 1, from which $\Psi_1 = 0$, $\Psi_2 = 0$ and $\Psi_3 > 0$ can be obtained. Thus, $J(t) = w(t)^T \Psi_3 w(t) \geq 0$. This, together with (3.2.13), implies that, for any $t_f \in [0, \ \infty)$ and $t_v \in [0, \ t_f]$, the following inequality holds:

$$\int_0^{t_f} J(t)dt \geq \int_0^{t_v} J(t)dt \geq \tilde{x}(t_v)^T G\tilde{x}(t_v) + \rho \tag{3.2.16}$$

Then, according to (3.2.3) and (3.2.16), the following inequality holds for any $t_f > 0$

$$\int_0^{t_f} J(t)dt - \tilde{z}(t_v)^T \Phi \tilde{z}(t_v) \geq \int_0^{t_f} J(t)dt - \sum_{i=1}^m \sigma_i(x^i(t_v), \lambda^i(t_v))\tilde{x}(t_v)^T \tilde{C}_i^T \Phi \tilde{C}_i \tilde{x}(t_v)$$

$$\geq \int_0^{t_f} J(t)dt - \tilde{x}(t_v)^T G\tilde{x}(t_v) \geq \rho \tag{3.2.17}$$

Thus, inequality (3.2.14) holds for any $t_f \in [0, \infty)$ and $t_v \in [0, t_f]$. Through considering the two cases of $\|\Phi\| = 0$ and $\|\Phi\| \neq 0$ as discussed above, it is easy to conclude that filtering error system (3.1.8) is extended dissipative in the sense of Definition 1. With $w(t) = 0$, it follows from (3.2.11) that

$$\dot{V}(t) \leq \tilde{z}(t)^T \Psi_1 \tilde{z}(t) - \mu \|\tilde{x}(t)\|^2 \tag{3.2.18}$$

Noticing that $\Psi_1 \leq 0$ under Assumption 1, it can be concluded that $\dot{V}(t) \leq -\mu\|\tilde{x}(t)\|^2$, which means that the filtering error system (3.1.8) with $w(t) = 0$ is asymptotically

stable. Additionally, by constraint condition (3.2.4), it is obtained that (3.1.9) holds. According to Lemma 3.1, all the eigenvalues of filtering error system lie in a circular region, centering in q with radius r. This completes the proof. $\qquad\square$

Remark 3.4 *Theorem 4.1 provides the performance criteria for the filtering error system (3.1.8) with given filter matrices. The performance criteria in Theorem 4.1 are expressed in the form of LMIs. It follows from (3.1.10) that $\rho = 0$ under zero initial conditions. Thus, by choosing appropriate matrices Φ, Ψ_1, Ψ_2 and Ψ_3 as discussed in Remark 3.3, Theorem 4.1 can be applied to check the $L_2 - L_\infty$ performance, H_∞ performance, passivity, dissipativity and very-strict passivity for the filtering error system (3.1.8), respectively.*

Based on the conditions in Theorem 4.1, the problem of model-independent filter design for systems with state-dependent uncertainties will be solved in the following part. Recalling Assumption 1 and noting that $\Phi \geq 0$, $\Psi_1 \leq 0$, there always exist matrices $\tilde{\Phi}$ and $\tilde{\Psi}_1$ such that

$$\Phi = \tilde{\Phi}^T \tilde{\Phi}, \quad \Psi_1 = -\tilde{\Psi}_1^T \tilde{\Psi}_1 \tag{3.2.19}$$

The existence conditions of filter design for system (3.1.1) are presented in the following theorem.

$$\overline{\Pi}_i = \begin{bmatrix} [RA_i + \overline{B}_f E_i]_s & \overline{A}_f + A_i^T L^T + E_i^T \overline{B}_f^T & RB_i + \overline{B}_f F_i - C_i^T \Psi_2 & C_i^T \tilde{\Psi}_1^T \\ \star & [\overline{A}_f]_s & LB_i + \overline{B}_f F_i + \overline{C}_f^T \Psi_2 & -\overline{C}_f^T \tilde{\Psi}_1^T \\ \star & \star & -[D_i^T \Psi_2]_s - \Psi_3 & D_i^T \tilde{\Psi}_1^T \\ \star & \star & \star & -I \end{bmatrix} \tag{3.2.20}$$

Theorem 3.2 *For given matrices $\tilde{\Phi}$, $\tilde{\Psi}_1$, Ψ_2 and Ψ_3 satisfying (3.2.19) and Assumption 1, the filtering error system in (3.1.8) is asymptotically stable, and satisfies a new performance index in Definition 1, and the poles lie in the circular region $\mho(q, r)$ defined*

in Lemma 3.1, if there exist matrices $R > 0$, $L > 0$, $\overline{G} > 0$, $\overline{A}_f$, $\overline{B}_f$ and $\overline{C}_f$ with appropriate dimensions satisfying the following conditions, $\forall i \in \mathcal{S}$:

$$\overline{G} < \overline{P} \tag{3.2.21}$$

$$\overline{\Pi}_i < 0 \tag{3.2.22}$$

$$\overline{\Theta}_i < 0 \tag{3.2.23}$$

$$\begin{bmatrix} -\overline{P} & W_i \\ \star & -r^2\overline{P} \end{bmatrix} < 0 \tag{3.2.24}$$

where

$$\overline{P} = \begin{bmatrix} R & L \\ L & L \end{bmatrix}, \ \overline{G} = \begin{bmatrix} G_1 & G_2 \\ \star & G_3 \end{bmatrix}$$

$$\overline{\Theta}_i = \begin{bmatrix} -G_1 & -G_2 & C_i^T \tilde{\Phi}^T \\ \star & -G_3 & -\overline{C}_f^T \tilde{\Phi}^T \\ \star & \star & -I \end{bmatrix}$$

$$W_i = \begin{bmatrix} RA_i + \overline{B}_f E_i - qR & \overline{A}_f - qL \\ LA_i + \overline{B}_f E_i - qL & \overline{A}_f - qL \end{bmatrix}$$

and $\overline{\overline{\Pi}}_i$ is defined in (3.2.20). Moreover, if above LMIs have feasible solution, the filter matrices for model-independent filter (3.1.7) are given by

$$A_f = L^{-1}\overline{A}_f, \ B_f = L^{-1}\overline{B}_f, \ C_f = \overline{C}_f \tag{3.2.25}$$

Proof: From the inequality of (3.2.10), it is concluded that $\Pi_i < 0$, $i \in \mathcal{S}$. Under the condition of $\Psi_1 = -\tilde{\Psi}_1^T \tilde{\Psi}_1$ in (3.2.19), and applying the Schur complement equivalence,

we have that inequality (3.2.2) is equivalent to $\tilde{\Pi}_i < 0$, where

$$\tilde{\Pi}_i = \begin{bmatrix} [P\tilde{A}_i]_s & P\tilde{B}_i - \tilde{C}_i^T \Psi_2 & \tilde{C}_i^T \tilde{\Psi}_1^T \\ \star & -[\tilde{D}_i^T \Psi_2]_s - \Psi_3 & \tilde{D}_i^T \tilde{\Psi}_1^T \\ \star & \star & -I \end{bmatrix} \tag{3.2.26}$$

Furthermore, defining matrix variables

$$P \equiv \begin{bmatrix} P_{11} & P_{12} \\ P_{21} & P_{22} \end{bmatrix}, \quad H = \begin{bmatrix} I & 0 \\ 0 & P_{12}P_{22}^{-1} \end{bmatrix}$$

where $P_{11} > 0$, $P_{22} > 0$, $P_{12} = P_{21}^T$, and P_{12} is an invertible matrix. Particularly, define $R \equiv P_{11}$. Then, perform a congruence transformation to (3.2.26) by pre-multiplying $diag\{H, I, I\}$ and post-multiplying its transpose with the change of matrix variables defined by

$$\overline{A}_f = P_{12}A_f P_{22}^{-1} P_{12}^T, \quad \overline{B}_f = P_{12}B_f$$
$$\overline{C}_f = C_f P_{22}^{-1} P_{12}^T, \quad L = P_{12}P_{22}^{-1}P_{12}^T$$

It can be easily seen that (3.2.22) holds. Define $\overline{G} = HGH^T$, $\overline{P} = HPH^T$, by pre-multiplying $diag\{H, H\}$ and post-multiplying its transpose to (3.2.1), respectively, (3.2.21) holds. Similarly, pre-multiplying $diag\{H, H\}$ and post-multiplying its transpose to (3.2.4) yields the condition in (3.2.24). In addition, by applying the Schur complement with the condition of $\Phi = \tilde{\Phi}^T \tilde{\Phi}$ in (3.2.19), it can be obtained from (3.2.3) that

$$\begin{bmatrix} -G & \tilde{C}_i^T \tilde{\Phi}^T \\ \star & -I \end{bmatrix} < 0 \tag{3.2.27}$$

Then, pre-multiplying $diag\{H, I\}$ and post-multiplying its transpose to (3.2.27), respectively, gives that (3.2.23) holds. Thus, if the inequalities (3.2.21)-(3.2.24) in Theorem (3.2) hold, the filter design problem is solvable, and the filter matrices are designed

by

$$A_f = P_{12}^{-1}\overline{A}_f P_{12}^{-T} P_{22}, \ B_f = P_{12}^{-1}\overline{B}_f, \ C_f = \overline{C}_f P_{12}^{-T} P_{22}$$

Note that $P_{22} > 0$ and P_{12} is an invertible matrix, thus $P_{12}^{-T} P_{22}$ is a non-singular matrix. Define $Q = P_{12}^{-T} P_{22}$, and consider the equivalence transformation $\bar{x}_f(t) = Qx_f(t)$. Then, the system

$$\begin{cases} \dot{\bar{x}}_f(t) = QA_f Q^{-1}\bar{x}_f(t) + QB_f y(t) \\ z_f(t) = C_f Q^{-1}\bar{x}_f(t) \end{cases}$$

is said to be (algebraically) equivalent to the filter (3.1.7). Therefore, the filter matrices can be recovered in the following form

$$A_f = QP_{12}^{-1}\overline{A}_f P_{12}^{-T} P_{22} Q^{-1} = L^{-1}\overline{A}_f$$
$$B_f = QP_{12}^{-1}\overline{B}_f = L^{-1}\overline{B}_f, \ C_f = \overline{C}_f P_{12}^{-T} P_{22} Q^{-1} = \overline{C}_f$$

This completes the proof. □

Remark 3.5 *With the result of Theorem 3.2, the robust filtering problem can be rapidly and easily solved by testing the feasibility of the LMIs conditions (3.2.21)-(3.2.24). Also notice that any feasible solution to (3.2.21)-(3.2.24) yields a suitable robust filter. The minimum disturbance attenuation performance level γ such that the conditions in Theorem 3.2 hold can be readily obtained from the optimal solution of the following convex optimization problem:*

$$\min_{R,L,\overline{G},\overline{A}_f,\overline{B}_f,\overline{C}_f} \delta$$
$$subject\ to\ \ (3.2.21) - (3.2.24),\ with\ \delta \equiv \gamma^2$$

The minimum value of γ is given by $\gamma^* = \sqrt{\delta^*}$, where γ^* is the optimal value of γ, and the corresponding optimal filter is as (3.2.25).

Remark 3.6 *Here, conservativeness of the robust filter design approach proposed in this*

chapter is discussed. In order to deal with the problem of inaccessible model informa-tion, we design a common model-independent filter for all the vertices of the uncertainty polytope. Thus, model-independent filter inevitably has some degrees of conservative-ness. If the model information can be directly accessible, we can design model-dependent filter for each vertex of the uncertainty polytope. Compared with model-independent fil-ter, model-dependent filter has the advantage of reducing the conservativeness, but the implementation is more complex.

3.3 Simulation examples

In this section, a numerical example of tunnel diode circuit system will be presented to demonstrate the applicability of the proposed model-independent filter design approach. All of the results of this section are attained by using MATLAB-based toolbox YALMIP [94] and the solver SDPT3 [95] for solving convex optimization problem.
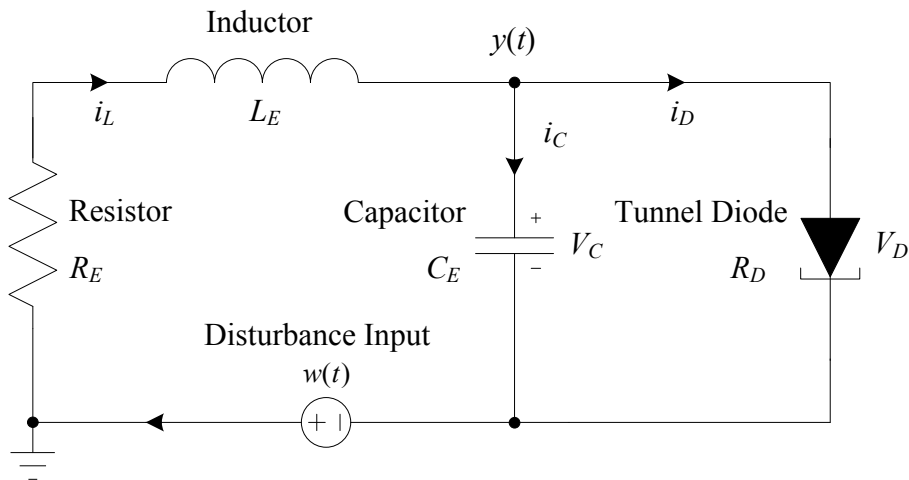
Fig. 3.1: Tunnel diode circuit.

Consider a tunnel diode circuit system as depicted in Fig. 3.1, which is characterized

by

$$\begin{cases} C_E \dot{V}_C(t) = -i_D(t) + i_L(t) \\ L_E \dot{i}_L(t) = -V_C(t) - R_E i_L(t) + w(t) \\ \quad z(t) = \quad i_L(t) \\ \quad y(t) = \quad V_C(t) - w(t) \end{cases}$$

where $i_L(t)$ is the current through the inductor L_E; $V_C(t)$, $V_D(t)$ are the voltages across the capacitor C_E and tunnel diode, respectively; $i_D(t)$ is the current through the tunnel diode and $i_D(t)$ is uncertain and depends nonlinearly on $V_D(t)$; $y(t)$ is the measured voltage; $z(t)$ is the current to be estimated and $w(t)$ is the disturbance input. Here, suppose that [104]

$$i_D(t) = l_1 V_D(t) + l_2 V_D^3(t)$$

Let $x_1(t) = V_C(t)$, $x_2(t) = i_L(t)$ be the state variables and $x(t) = [x_1(t) \quad x_2(t)]^T$, then the tunnel diode circuit can be governed by the following equations:

$$\begin{cases} \dot{x}(t) = \begin{bmatrix} -\dfrac{l_1 + l_2 x_1^2(t)}{C_E} & \dfrac{1}{C_E} \\ -\dfrac{1}{L_E} & -\dfrac{R_E}{L_E} \end{bmatrix} x(t) + \begin{bmatrix} 0 \\ 1 \end{bmatrix} w(t) \\ z(t) = \begin{bmatrix} 0 & 1 \end{bmatrix} x(t) \\ y(t) = \begin{bmatrix} 1 & 0 \end{bmatrix} x(t) - w(t) \end{cases}$$

Then, we consider the tunnel diode circuit with the parameters:

$$C_E = 20 \, \text{mF}, L_E = 2000 \, \text{mH}, l_1 = 0.002, l_2 = 0.01$$

$$R_E = R_{E0} + \alpha, R_{E0} = 10 \, \Omega, \ \alpha \in [-30\% R_{E0} \quad 30\% R_{E0}]$$

where α denotes the parameter's uncertainty of resistor R_E, which maybe come directly from the sources: aging of the materials, constructive differences and thermal drift. Thus, the parameter of R_E is supposed to vary in a 30% range with respect to the nominal value R_{E0}. Without sacrificing the generality, assume that $x_1(t) \in [-3 \quad 3]$. The above

diode circuit can be rewritten in a polytopic form:

$$
\begin{cases}
\dot{x}(t) = \sum_{i=1}^{4} \sigma_i(x^i(t), \alpha) \left[A_i x(t) + B_i w(t) \right] \\
z(t) = \sum_{i=1}^{4} \sigma_i(x^i(t), \alpha) \left[C_i x(t) + D_i w(t) \right] \\
y(t) = \sum_{i=1}^{4} \sigma_i(x^i(t), \alpha) \left[E_i x(t) + F_i w(t) \right]
\end{cases}
\tag{3.3.1}
$$

where $\sigma_1(x^1(t), \alpha) = \frac{x_1(t)^2}{18}$, $\sigma_2(x^2(t), \alpha) = 0.5 - \frac{x_1(t)^2}{18}$, $\sigma_3(x^3(t), \alpha) = \frac{3+\alpha}{12}$, $\sigma_4(x^4(t), \alpha) = \frac{3-\alpha}{12}$ and for $\forall\, i \in \mathcal{S} = \{1,\ 2,\ 3,\ 4\}$,

$$
A_1 = \begin{bmatrix} -9.1 & 50 \\ -1 & -10 \end{bmatrix},\ A_2 = \begin{bmatrix} -0.1 & 50 \\ -1 & -10 \end{bmatrix}
$$

$$
A_3 = \begin{bmatrix} -0.1 & 50 \\ -1 & -16 \end{bmatrix},\ A_4 = \begin{bmatrix} -0.1 & 50 \\ -1 & -4 \end{bmatrix}
$$

$$
B_i \equiv [0\ 1]^T,\ C_i \equiv [0\ 1],\ D_i \equiv 0,\ E_i \equiv [1\ 0],\ F_i \equiv -1
$$

Remark 3.7 *However, it is noted that the model-dependent filter in the form of (5.2.4) is no longer applicable for such a case, because of the uncertain parameter α from the uncertainty of resistor R_E , which cannot be accessible in the design of model-dependent filters. Therefore, we aim at designing a model-independent filter in the form of (3.1.7) to suppress the parameter's uncertainties and disturbances with a guaranteed performance index.*

Consider the filtering error system (3.1.8) with $\mathcal{D}$ stability constraints defined in Lemma 3.1, and the poles lie in a circular region $\mho(-20,\ 19.9)$ with center $q = (-20,\ 0)$ and radius $r = 19.9$ as depicted in Fig. 3.2. Under a unified frame, the model-independent filter is designed to satisfy H_∞, $L_2 - L_\infty$, passive and dissipative performances. Due to limited space, we only consider the H_∞ performance in this example. Let $\Phi = 0$, $\Psi_1 = -1$, $\Psi_2 = 0$ and $\Psi_3 = \gamma^2$. Then, it is obtained from (3.2.19) that $\tilde{\Phi} = 0$, $\tilde{\Psi}_1 = 1$. By applying the approach proposed in Theorem 3.2, we can obtain the minimum H_∞ noise attenuation performance index $\gamma^* = 0.2291$ and the corresponding model-independent

filter matrices are given by:

$$A_f = \begin{bmatrix} -7.5290 & 43.6298 \\ 0.0337 & -7.0407 \end{bmatrix}, \quad B_f = \begin{bmatrix} 0.5557 \\ 1.2906 \end{bmatrix}$$
$$C_f = \begin{bmatrix} 0.0249 & -0.7337 \end{bmatrix}$$

It can be seen from Fig. 3.3 that all the poles of filtering error system with respect to uncertain parameter $\alpha \in [-3, \ 3]$ lie in the circular region $\mho(-20, \ 19.9)$, which verifies that the filter satisfies the designed $\mathcal{D}$ stability constraints.
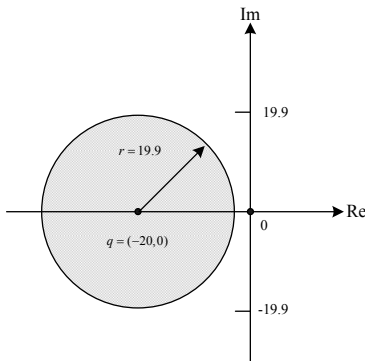
Fig. 3.2: Circular region.
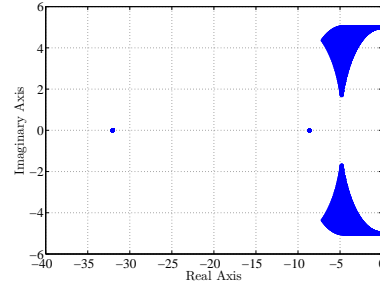
Fig. 3.3: Poles of the filtering error system with $\alpha \in [-3, \ 3]$.

Remark 3.8 *If the parameters are* $\Phi = 1$ *(*$\tilde{\Phi} = 1$*),* $\Psi_1 = 0$ *(*$\tilde{\Psi}_1 = 0$*),* $\Psi_2 = 0$ *and* $\Psi_3 = \gamma^2$*. By applying the approach proposed in Theorem 3.2, we can obtain the minimum* $L_2 - L_\infty$ *noise attenuation performance index* γ^* *and the corresponding* $L_2 - L_\infty$ *filter. Similarly, by setting appropriate parameters, Theorem 3.2 is applicable to the design of passive filter or dissipative filter. This can allow us to choose a suitable filter by adjusting the weighting matrices in the new performance index according to the different practical applications or noise levels, which is the most important distinction between the robust filter design approach proposed in this chapter and the general* $H_\infty / L_2 - L_\infty$ *filters design approaches.*

Frequency response for different filtering error system vertex is depicted in Fig.3.4, which verifies that the designed filters can guarantee the optimal H_∞ disturbance attenuation performance on the whole frequency domain.
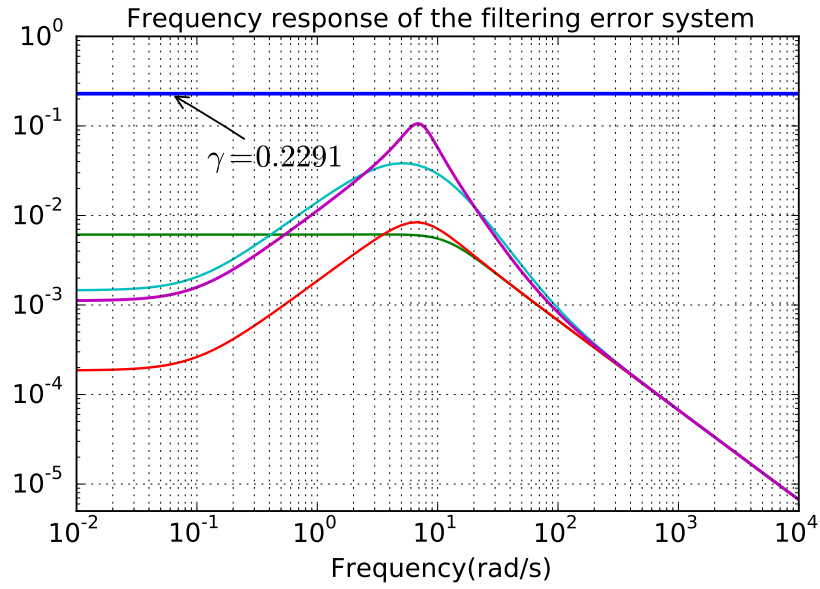
Fig. 3.4: Frequency response of the filtering error system.
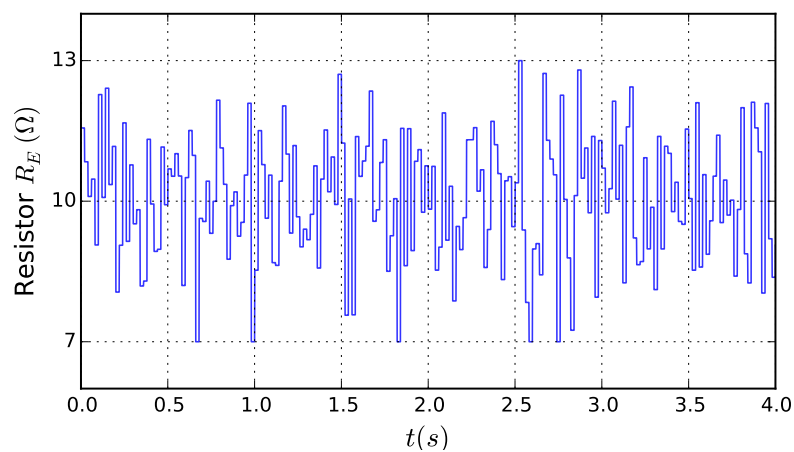
Fig. 3.5: Random resistor value uniformly distributed in the range [7 13].
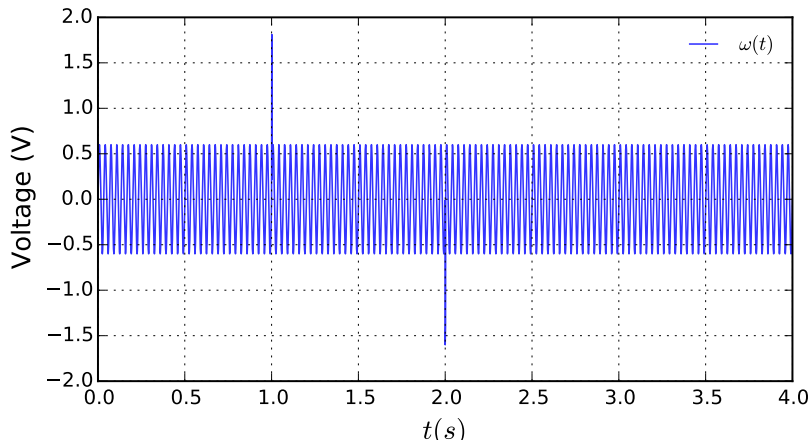
Fig. 3.6: Disturbance input $w(t) = 0.5\sin(60\pi t)$
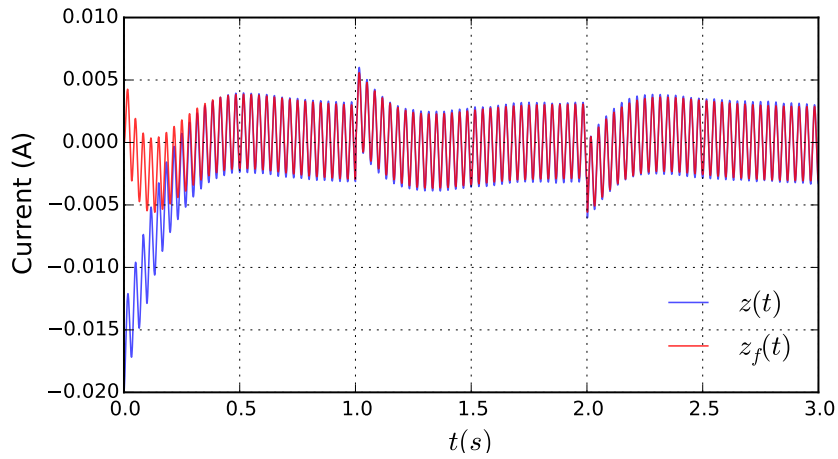
Fig. 3.7: Comparison between $z(t)$ to be estimated and filter output $z_f(t)$.
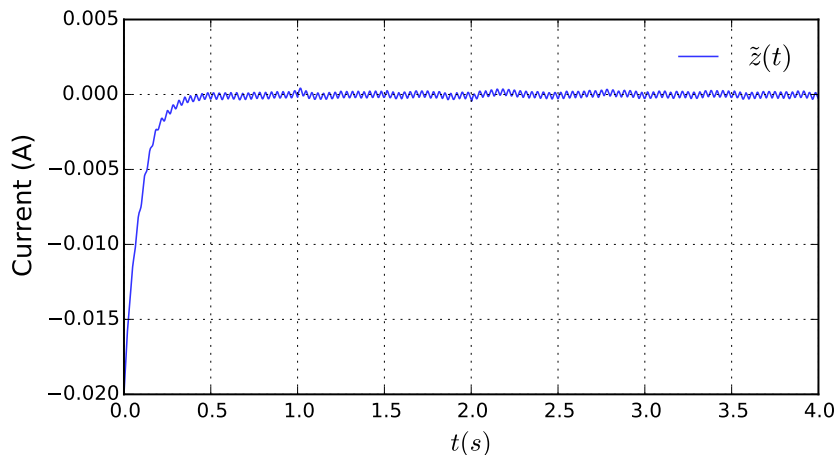
Fig. 3.8: Response of filtering error signal $\tilde{z}(t)$.
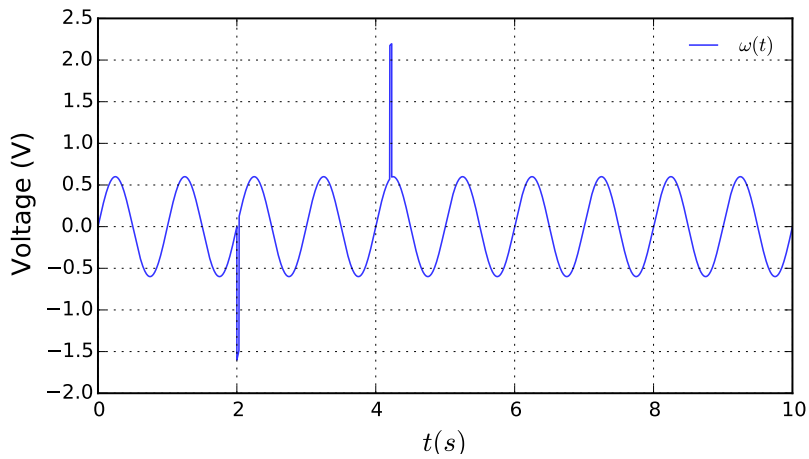
Fig. 3.9: Disturbance input $w(t) = 0.5 \sin(2\pi t)$
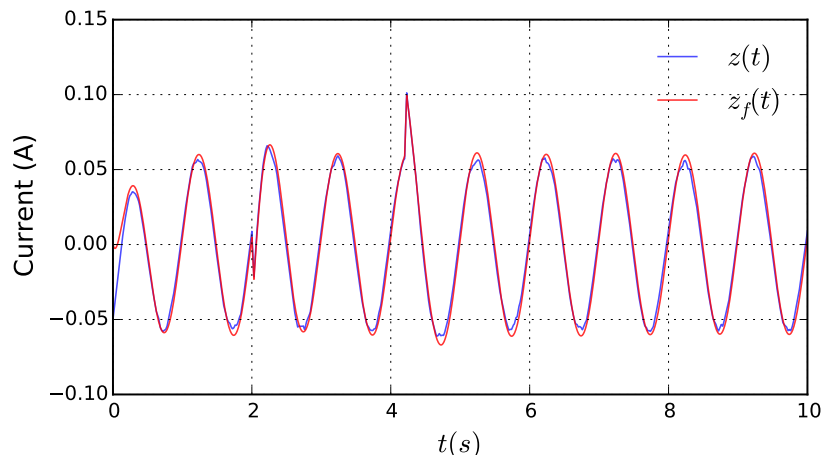
Fig. 3.10: Comparison between $z(t)$ to be estimated and filter output $z_f(t)$.
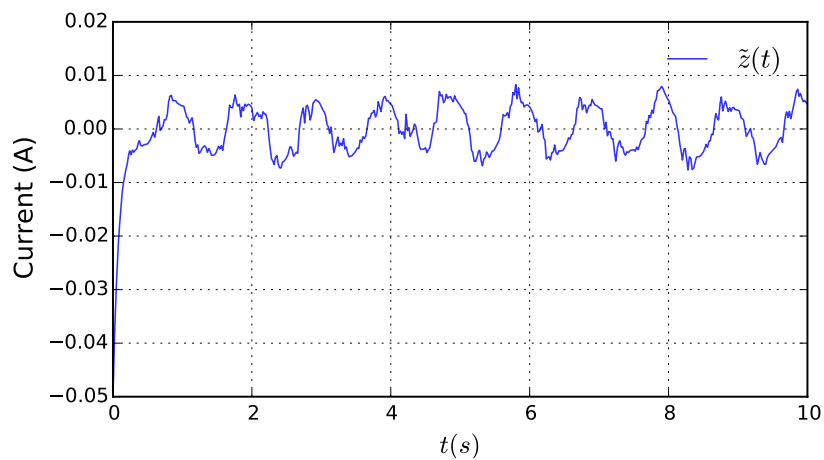
Fig. 3.11: Response of filtering error signal $\tilde{z}(t)$.

The disturbance input $w(t)$ is the combination of sinusoidal and pulse signal. Meanwhile, it is assumed that the uncertain parameter α is time-varying and stochastic in the range of $[-30\%R_{E0},\ 30\%R_{E0}]$ as shown in Fig.3.5. To illustrate the performance of the design filter, assume that the initial condition of the system (3.3.1) is $x(0) = [0.2\ -0.05]^T$ and the initial condition of the corresponding filter system is $x_f(0) = [0\ \ 0]^T$.

Under two different frequency disturbances, the comparison results between the signal $z(t)$ to be estimated and filter output $z_f(t)$ are depicted from Fig. 3.6 to Fig. 3.11. Note that although the initial conditions are different, the filtering error signal finally reduces to a low level. According to above simulation results, it is concluded that the proposed robust model-independent filter can estimate the signal to be estimated precisely and effectively in spite of parameters uncertainties and external disturbances.

3.4 Concluding remarks

This chapter has addressed the filter design problem for a class of dynamical system with state-dependent uncertain parameters. By introducing a new performance index, the H_∞, L_2-L_∞ and dissipative filtering problems with $\mathcal{D}$ stability constraints have been solved in a unified framework. Through employing the Lyapunov stability theory, the feasibility criteria for analysis of robust disturbance attenuation performance have been derived. Furthermore, the LMIs-based approaches for the design of model-independent filters of the considered system with state-dependent uncertain parameters have been developed. A numerical example of the tunnel diode circuit system has been provided to demonstrate the applicability and effectiveness of the proposed model-independent filter design method. It should also be mentioned that the method proposed in this chapter can be applied to solve systems with other types uncertainties or more complex dynamics.

4 A novel vibration sensor system with state-dependent nonlinearity

This chapter will design a bio-inspired vibration sensor for accurate real-time measurement of absolute motion. It is known that this bio-inspired structure with state-dependent QZS property can create an absolute stable point to acquire very excellent performance of vibration isolation or suppression. With this idea, the problem of measurement of absolute motion can be translated into the measurement of relative motion between the stable point and other vibrating points in bio-inspired vibration sensor. The relative motion can be easily measured by using various sensors such as optical encoder and grating ruler. Importantly, the measurement accuracy and bandwidth can be fulfilled conveniently through flexibly adjusting corresponding structural parameters. Hence, the problems of error accumulation and real-time from accelerometer measurement can be eliminated by utilizing the bio-inspired vibration sensor.

Although the fault detection techniques have been greatly developed [44–48] in the field of vibration-based analysis, there still exist some attractive and challenging topics worth further studying, one of which is how to detect the weak fault signal with fast time-varying characteristic from strong vibration in real time. For example, in vibration and shock testing platform, the weak fault may be masked in vibration signal. Existing frequency-domain based fault detection methods do not have the ability to identify it since the fast time-varying weak fault has almost no characterization on the spectrum. Multi-resolution wavelet-based method gives a positive answer to the detection problem of fast time-varying fault, which can be located by analysing the singular value

of wavelet decomposition components. However, it is worth noting that the wavelet-based fault detection method is not real time. As aforementioned observations, this bio-inspired vibration sensor system has provided a simple and effective way for the real-time accurate measurement of absolute motion, which makes the absolute motion based real-time fault detection possible. On the other side, the model-based method, which uses soft redundancy instead of hardware redundancy to generate residual signal for decision making, has been wildly applied in the fault detection of practical systems [105–108]. Through combining this bio-inspired vibration sensor and model-based fault detection method, a real-time fault detection algorithm based on measurement of absolute motion is proposed.

The remainder of this chapter is organized as follows. Section 4.1 starts with model description and analysis of the bio-inspired vibration sensor. In Section 4.2, an adaptive compensation method is applied to identification of sensor model parameter. Based on the bio-inspired vibration sensor, Section 4.3 presents an observer-based real-time fault detection algorithm. Some results are presented in Section 4.4 to demonstrate the effectiveness and applicability of the proposed methodologies. Finally, Section 4.5 concludes the chapter.

4.1 Model description and analysis

As depicted in Fig. 4.1, the n-layer bio-inspired vibration sensor system consists of connecting rods and rotating joints. This novel nonlinear structure is inspired by the limb structures of animals and insects in motion vibration control. As shown in Fig. 4.1, the bird's leg is Z-like skeleton. With this Z-like structure, the bird's running and landing is very steady, even in a very high speed. That means this Z-like structure has the potential of suppressing the vibration. In practical system, the X-like structure, which can be regarded as the combination of double Z-like structures, is much easier to be implemented. A linear spring with horizontal stiffness in the bottom layer is used as passive muscles. All the parameter descriptions of the bio-inspired vibration sensor are listed in Tab. 4.1.
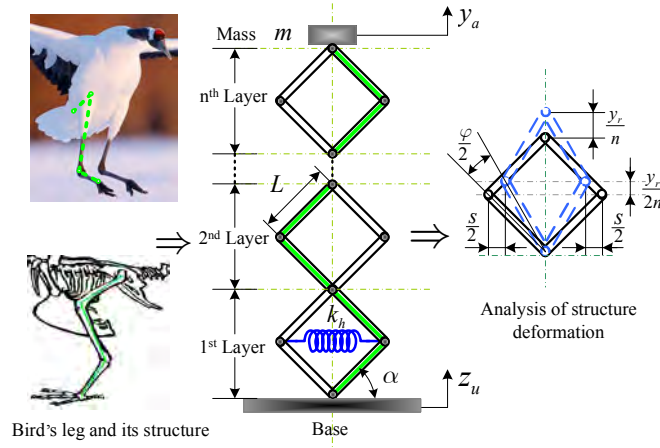
Fig. 4.1: Structural mechanism inspired from the bird's leg

Table 4.1: Parameter descriptions of the bio-inspired sensor

Symbol	Description
m	loading mass (kg)
L	length of rod (m)
α	initial angle (rad)
φ	rotational motion (rad)
s	horizontal motion (m)
n	number of layers
n_x	number of joints
k_h	linear spring stiffness (N/m)
c	rotational damping coefficient (N*s/rad)
y_a	absolute motion of the mass (m)
z_u	base excitation (m)
y_r	relative motion between mass and base (m)

Remark 4.1 *This bio-inspired vibration sensor is mainly designed for measurement of absolute vertical motion. In practical structure, a support rod will be placed in the center line to limit the movement towards the vertical direction. Along these lines, the deformation on the bio-inspired vibration sensor is symmetrical. The dynamics can be modeled as a single degree of freedom system.*

The relationships among φ, s, and y_r are described as

$$\varphi = 2\arctan\left(\frac{L\sin\alpha + \frac{y_r}{2n}}{L\cos\alpha - \frac{s}{2}}\right) - 2\alpha \tag{4.1.1}$$

$$s = 2L \cos \alpha - 2\sqrt{L^2 - (L \sin \alpha + \frac{y_r}{2n})^2} \qquad (4.1.2)$$

Here, selecting the upward as the positive direction, the relative motion between the mass and base is $y_r = y_a - z_u$.

By resorting to Lagrange's method as in [56], the dynamics of such a bio-inspired sensor system is characterized by

$$m\ddot{y}_r + m\ddot{z}_u + k_h s \frac{ds}{dy_r} = -c\, n_x (\frac{d\varphi}{dy_r})^2 \dot{y}_r \qquad (4.1.3)$$

$$\frac{d\varphi}{dy_r} = \frac{1}{n\sqrt{L^2 - (L \sin \alpha + \frac{y_r}{2n})^2}}$$

$$\frac{ds}{dy_r} = \frac{L \sin \alpha + \frac{y_r}{2n}}{n\sqrt{L^2 - (L \sin \alpha + \frac{y_r}{2n})^2}}$$

where $k_h\, s \frac{ds}{dy_r}$ and $c\, n_x (\frac{d\varphi}{dy_r})^2 \dot{y}_r$ are equivalent nonlinear stiffness and damping correspondingly. Notice that the equivalent nonlinear stiffness and damping come not from the nonlinear spring and/or damper but from the specially geometric relationship of this bio-inspired sensor structure, which is one of the obvious advantages.

Taylor series expansion of the nonlinear term in system (4.1.3). Equivalent nonlinear stiffness term $k_h\, s \frac{ds}{dy_r}$

$$k_h\, s \frac{ds}{dy_r} = \frac{\tan^2 \alpha\, k_h}{n^2} y_r + \frac{3 \sin \alpha \sec^4 \alpha\, k_h}{4\, L n^3} y_r{}^2 \qquad (4.1.4)$$
$$- \frac{(4 \sec^4 \alpha - 5 \sec^6 \alpha)\, k_h}{8\, L^2 n^4} y_r{}^3 + O(y_r{}^4)$$

Equivalent nonlinear damping coefficient $c\, n_x (\frac{d\varphi}{dy_r})^2$

$$c\, n_x (\frac{d\varphi}{dy_r})^2 = c\, n_x \left(\frac{\sec^2 \alpha}{L^2 n^2} + \frac{\sin \alpha \sec^4 \alpha}{L^3 n^3} y_r \qquad (4.1.5) \right.$$
$$\left. - \frac{(3 \sec^4 \alpha - 4 \sec^6 \alpha)}{4 L^4 n^4} y_r{}^2 + O\left(y_r{}^3\right) \right)$$

As can be seen from (4.1.3), the equivalent nonlinear stiffness $k_h s \frac{ds}{dy_r}$ and damping coefficient $c\,n_x\left(\frac{d\varphi}{dy_r}\right)^2$ are rather complicated. For the convenience of analysis and design, the equivalent nonlinear stiffness and damping coefficient are represented as polynomial expressions through Taylor series expansion at zero equilibrium, which are given in (4.1.4) and (4.1.5). Since the vertical motion of the bio-inspired sensor considered in this chapter does not exceed 0.1 m as shown in Section 4.4, the approximation accuracy is acceptable in the rest analysis and design.
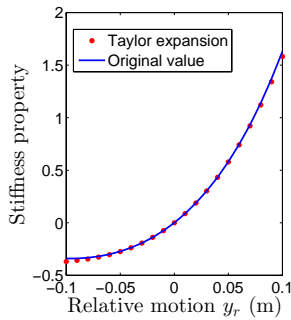
Fig. 4.2: Comparison between exact value and Taylor expansion (stiffness)
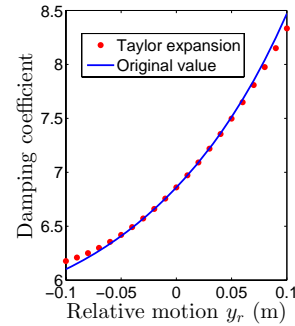
Fig. 4.3: Comparison between exact value and Taylor expansion (damping)

Then, the resonant frequency of the bio-inspired vibration sensor system is

$$f_0 = \frac{\tan\alpha}{2\,n\,\pi}\sqrt{\frac{k_h}{m}} \tag{4.1.6}$$

The equivalent nonlinear stiffness (4.1.4) depends not only on the linear spring stiffness but also on the connecting rod length, initial angle, and lay number. This is the superiority of the bio-inspired structure, and also the fundamental distinction between the traditional mass-spring system and the bio-inspired structure of this thesis. With the beneficial nonlinear stiffness, the low resonant frequency can be easily achieved through adjusting the structural parameters, upon which a wider frequency range with excellent vibration isolation or suppression performance can be guaranteed.

In addition, the equivalent nonlinear damping can make a positive contribution to improve the vibration isolation or suppression performance. Generally, increasing the linear damping can suppress the resonant peak but also degrades the performance at high

frequency range. This difficulty can also be settled by resorting to the equivalent non-linear damping providing the strong damping at resonant region but weak damping at high frequency range. Thus, with the beneficial nonlinear stiffness and damping, this bio-inspired structure has excellent vibration isolation or suppression performance, as detailed discussion and analysis in [53, 56, 57].

Remark 4.2 *When the resonant frequency of the bio-inspired structure is sufficiently low, the QZS characteristic can be achieved in a very wide range of frequencies. With the QZS property, a very excellent performance of vibration isolation or suppression can be acquired. Then the top layer mass m is approximately equivalent to a stable anti-vibration point, i.e., the amplitude of y_a is close to zero and $z_u \approx -y_r$. Thus, the measurement of absolute motion z_u can be translated into the measurement of relative motion y_r between the stable anti-vibration point and the base in this bio-inspired vibration sensor. By resorting to some simple sensors such as optical encoder and grating ruler, the relative motion y_r can be easily measured. Furthermore, this bio-inspired vibration sensor can achieve desired measurement performance by tuning the structural parameters (e.g., connecting rod length, initial angle, layer number, spring stiffness, and loading mass). A simple description about the effects of the structural parameters on the performance of vibration isolation is summarized in Table 4.2. The symbol "—", "↑", and "↓" represent increase, decrease, and no change respectively. Actually, these structural parameters are strongly coupled through the geometrical nonlinearity. When designing structural parameters, tradeoff considerations must be executed according to the practical application. For example, a spring with smaller stiffness is selected to obtain lower resonant frequency and wider frequency range of vibration isolation or suppression, but the smaller stiffness will result in the significant degradation of loading capacity and cause a larger static displacement, thus the tradeoff between the vibration isolation/suppression performance and loading capacity should be taken into account.*

Obviously, the relative motion y_r can be determined through measuring the rotation angle φ, which is implemented by installing an optical encoder in the bottom joint. The

Table 4.2: The effects of the structural parameters

	Resonant frequency	Vibration transmissibility
Increasing L	—	↑
Increasing α	↑	↑
Increasing n	↓	↓
Increasing k_h	↑	↑
Increasing c	—	↓

relationship between the rotation angle φ and the relative motion y_r is determined by

$$y_r = 2nL(\sin(\alpha + \frac{\varphi}{2}) - \sin(\alpha)) \tag{4.1.7}$$

Let $x_1(t) = y_r(t)$ and $x_2(t) = \dot{y}_r(t)$ be state variables, then the bio-inspired vibration sensor system (4.1.3) can be expressed as the following nonlinear state space equation

$$\dot{x}(t) = \begin{bmatrix} \dot{y}_r \\ -\frac{k_h}{m} s \frac{ds}{dy_r} - \frac{c}{m} n_x (\frac{d\varphi}{dy_r})^2 \dot{y}_r \end{bmatrix} + \begin{bmatrix} 0 \\ -1 \end{bmatrix} u(t) \tag{4.1.8}$$

where $x(t) = [x_1(t)\ x_2(t)]^T$ is state vector, $u(t) = \ddot{z}_u(t)$ is input signal.

Implementing the real-time measurement and fault detection requires the discrete time model of above sensor system, which is obtained according to the Euler discretization method and Taylor expansions as given in (4.1.4) and (4.1.5). For simple description, x_k^i is used to represent the ith state at time instance k. And define $x_k^1 = y_r$, $x_k^2 = \dot{y}_r$.

$$x_{k+1} = Ax_k + D_f\, f(x_k) + Bu_k \tag{4.1.9}$$

where $f(x_k)$ is a nonlinear function of state variables,

$$\begin{aligned} f(x_k) &= \frac{3 \sin\alpha \sec^4\alpha\, k_h}{4\, m\, Ln^3} {y_r}^2 - \frac{(4 \sec^4\alpha - 5 \sec^6\alpha)\, k_h}{8\, m\, L^2 n^4} {y_r}^3 \\ &+ c\, n_x\, \dot{y}_r \left(\frac{\sin\alpha\ \sec^4\alpha}{m\, L^3 n^3} y_r - \frac{(3 \sec^4\alpha - 4 \sec^6\alpha)}{4\, m\, L^4 n^4} {y_r}^2 \right) \end{aligned} \tag{4.1.10}$$

T_s is the sampling period and

$$A = \begin{bmatrix} 1 & T_s \\ -\frac{\tan^2 \alpha \, k_h \, T_s}{m \, n^2} & 1 - \frac{c \, n_x \, \sec^2 \alpha \, T_s}{m \, L^2 n^2} \end{bmatrix}, D_f = \begin{bmatrix} 0 \\ T_s \end{bmatrix} \qquad (4.1.11)$$

$$B = \begin{bmatrix} 0 \\ -T_s \end{bmatrix}$$

4.2 Parameter estimation

In many mechanical systems, it is hard to directly get ideal knowledge on the structure parameter or the cost of measurement is probably expensive [64, 109–112]. The same situation is encountered in this bio-inspired vibration sensor system. In order to obtain a comparatively exact model of the sensor system, an adaptive compensation method is applied to estimate the rotational damping coefficient [113].

For the convenience of estimating the damping coefficient, the bio-inspired sensor system (4.1.8) is reformulated as

$$x_{k+1} = x_k + F(x_k, u_k) + G(x_k, u_k)\theta \qquad (4.2.1)$$

where $\theta = \frac{c}{m}$ is the parameter to be estimated, nonlinear functions $F(x_k, u_k)$ and $G(x_k, u_k)$ are defined as

$$F(x_k, u_k) = T_s \begin{bmatrix} x_k^2 \\ -\frac{k_h}{m} s \frac{ds}{dy_r} - u_k \end{bmatrix}$$

$$G(x_k, u_k) = T_s \begin{bmatrix} 0 \\ -n_x (\frac{d\varphi}{dy_r})^2 \dot{y}_r \end{bmatrix}$$

Construct the following state-predictor for sensor system (4.2.1)

$$\hat{x}_{k+1} = \hat{x}_k + F(x_k, u_k) + G(x_k, u_k)\theta_0 + \mathcal{K}(x_k - \hat{x}_k) \qquad (4.2.2)$$

where θ_0 is the initial guess of unknown parameter θ and $\mathcal{K} > 0$ is the compensation

coefficient. Let the state estimation error be $e_k = x_k - \hat{x}_k$. From sensor system (4.2.1) and state predictor (4.2.2), the state estimation error is provided by

$$e_{k+1} = e_k + G(x_k, u_k)(\theta - \theta_0) - \mathcal{K}e_k \qquad (4.2.3)$$

Define auxiliary variables η_k and ω_k as

$$\eta_k = e_k - \omega_k(\theta - \theta_0) \qquad (4.2.4)$$

$$\omega_{k+1} = \omega_k + G(x_k, u_k) - \mathcal{K}\omega_k, \ \omega_0 = 0 \qquad (4.2.5)$$

According to (4.2.3), (4.2.4) and (4.2.5), it is obtained that

$$\eta_{k+1} = \eta_k - \mathcal{K}\eta_k, \ \eta_0 = e_0 \qquad (4.2.6)$$

Let the parameter estimation error be $\tilde{\theta}_k = \theta - \hat{\theta}_k$. The dynamic is presented as

$$\tilde{\theta}_{k+1} = \tilde{\theta}_k - \frac{1}{\|\mathcal{Q}_k\| + \varepsilon}(\mathcal{C}_k - \mathcal{Q}_k\hat{\theta}_k) \qquad (4.2.7)$$

Assume that at a time step k_c, $\mathcal{Q}_{k_c} > 0$ is satisfied. This condition is equivalent to the standard persistently exciting condition stated in terms of the sum of $w_k^T w_k$ being positive definite over a finite interval of time [113]. Then, it follows from (4.2.4) and (4.2.13) that the following relationship holds $\forall k \geq k_c$

$$\mathcal{Q}_k\theta = \sum_{i=0}^{k} \omega_i^T \omega_i \theta = \sum_{i=0}^{k} \omega_i^T(\omega_i\theta_0 + e_i - \eta_i) = \mathcal{C}_k \qquad (4.2.8)$$

Substituting $\mathcal{C}_k = \mathcal{Q}_k\theta$ into (4.2.7) yields

$$\tilde{\theta}_{k+1} = (I - \frac{\mathcal{Q}_k}{\|\mathcal{Q}_k\| + \varepsilon})\tilde{\theta}_k \qquad (4.2.9)$$

where ε is a small scalar. Thus the parameter estimation error $\tilde{\theta}$ is decreasing $\forall k \geq k_c$, and $\lim_{k\to\infty} \tilde{\theta} = 0$.

Consequently, an algorithm for the damping coefficient estimation is summarized as

follows.

Algorithm 4.1: Algorithm for Parameter Estimation

1: Give initial guess θ_0 and $\mathcal{K}$, set $k = 0$.

2: Calculate the state predictor (4.2.2).

3: Calculate the auxiliary variables.

$$\eta_{k+1} := \eta_k - \mathcal{K}\eta_k, \eta_0 = e_0 \tag{4.2.10}$$

$$\omega_{k+1} := \omega_k + G(x_k, u_k) - \mathcal{K}\omega_k, \omega_0 = 0 \tag{4.2.11}$$

$$\mathcal{Q}_{k+1} := \mathcal{Q}_k + \omega_k^T \omega_k, \mathcal{Q}_0 = 0 \tag{4.2.12}$$

$$\mathcal{C}_{k+1} := \mathcal{C}_k + \omega_k^T (\omega_k \theta_0 + e_k - \eta_k), \mathcal{C}_0 = 0 \tag{4.2.13}$$

4: Update parameter

$$\hat{\theta}_{k+1} := \hat{\theta}_k + \frac{1}{\|\mathcal{Q}_k\| + \varepsilon}(\mathcal{C}_k - \mathcal{Q}_k \hat{\theta}_k) \tag{4.2.14}$$

5: Set $k \leftarrow k + 1$, and go back to Stage 2.

Remark 4.3 *In light of the above analysis, it is clear that the parameter estimation error will converge to zero exponentially when the persistently exciting condition is satisfied. The experiment of parameter estimation will be conducted in the ideal laboratory environment, therefore system state and excitation input can be measured exactly.*

4.3 Application on fault detection

The bio-inspired vibration sensor system has provided a simple and effective way for the real-time measurement of absolute motion. In view of this point, a model-based strategy will be proposed to improve the performance of real-time vibration fault detection.

According to the discrete model (4.1.9), the sensor system considering fault input is modeled as

$$\begin{cases} x_{k+1} = Ax_k + D_f\,f(x_k) + B\,u_k + D\,d_k \\ y_{k+1} = Cx_{k+1} \end{cases} \tag{4.3.1}$$

Here, u_k is known excitation input and d_k is unknown fault input caused by the changes or damages to the monitored object structure. These changes or damages may be slowly time-varying or fast time-varying. The weak fault with fast time-varying characteristic widely exists in the practical fault diagnosis of mechanical equipment. Especially for the incipient fault of mechanical equipment, the fault signal is very weak and always submerged in the strong vibration. Due to the variance of operation condition and inherent nonlinearity of equipment, this weak fault is nonstationary signal and has fast time-varying characteristic. In general, the prior knowledge on the fast time-varying fault cannot be obtained in advance. By taking full advantage of the real-time absolute motion measurement and model-based detection method, a real-time fault detection can be simultaneously realized for both weak faults of slowly time-varying and fast time-varying. Matrices A, B, D_f and function $f(x_k)$ are defined in (4.1.9). Sensor matrix and fault distribution matrix are

$$C^T = \begin{bmatrix} 1 \\ 0 \end{bmatrix}, D = \begin{bmatrix} 0 \\ T_s \end{bmatrix} \tag{4.3.2}$$

To detect the fault input, inspired by [1], a full order nonlinear observer depicted in Fig.4.4 is constructed

$$z_{k+1} = N\,z_k + R\,u_k + L\,y_k + M\,D_f\,f(\hat{x}_k)$$
$$\hat{x}_k = z_k - E\,y_k \tag{4.3.3}$$

Vector $z_k \in \mathbb{R}^2$, $\hat{x}_k$ is the estimation of x_k. $f(\hat{x}_k)$ is a nonlinear term having the same structure as $f(x_k)$ defined in the system (4.1.9). The input to the observer is the known excitation u_k, which can be generated from a shaker or other vibration sources. The residual signal r_k is generated from the difference between the measurement of absolute
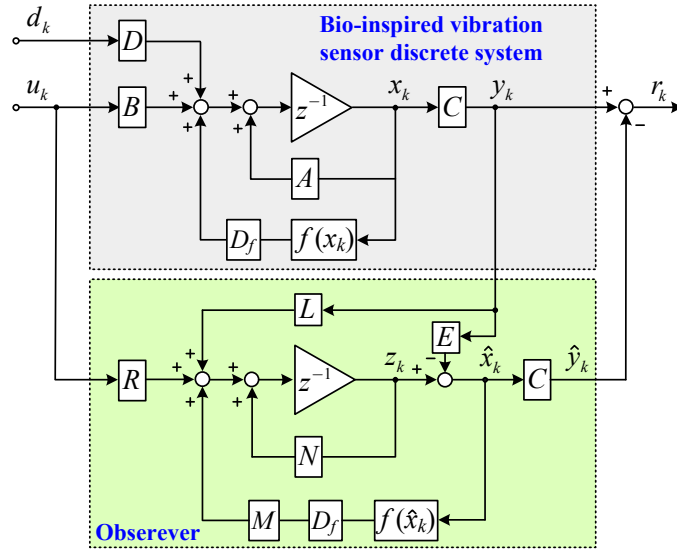
Fig. 4.4: Observer based fault detection block diagram

motion y_k and its estimation $\hat{y}_k$. Observer matrices N, R, L and M with appropriate dimensions are the unknown parameters to be determined.

A fault detection observer for system (4.3.1) is required to satisfy the following conditions: 1) the error dynamics $\tilde{x}_k = x_k - \hat{x}_k$ asymptotically converge to zero as $k \to \infty$ in fault-free case, i.e., $r_k \to 0$; 2) the inconsistencies between the fault-free case and faulty case can be reflected on the residual signal r_k.

It is noted that the nonlinear function $f(x_k)$ belongs to $\mathcal{C}^1$, i.e., its first-derivative exists and is continuous. On the other hand, the state variables are bounded (the range of absolute motion cannot exceed the length of the road and the energy of the input is bounded). Thus, nonlinear function $f(x_k)$ is locally Lipschitz. The following condition holds

$$\|f(x_l) - f(x_u)\| \leq \tau \|x_l - x_u\|, \forall x_l, x_u \in \Omega \tag{4.3.4}$$

where $\|\cdot\|$ is 2-norm operator, Ω is the bounded operating region of state variables and $\tau \geq 0$ is the Lipschitz constant. Due to $f(x_k) \in \mathcal{C}^1$, the Lipschitz constant can be

determined through calculating its derivative

$$\tau \geq \sup_{x_k \in \Omega} \{\|\frac{\partial f(x_k)}{\partial x_k}\|\} \tag{4.3.5}$$

Theorem 4.1 *For given Lipschitz constant τ, if there exist matrices $P > 0$, $\overline{E}$ and $\overline{X}$ with appropriate dimensions satisfying the following conditions: $MD \neq 0$ and*

$$\begin{bmatrix} \tau^2 I - P & 0 & A^T P + A^T C^T \overline{E}^T - C^T \overline{X}^T \\ * & -I & D_f^T P + D_f^T C^T \overline{E}^T \\ * & * & -P \end{bmatrix} < 0 \tag{4.3.6}$$

then (4.3.3) is a fault detection observer for the sensor system (4.3.1). Moreover, the observer parameters are given by

$$E = P^{-1} \overline{E}, \qquad X = P^{-1} \overline{X}$$
$$M = I + EC, \quad R = MB$$
$$N = MA - XC, L = X(I + CE) - MAE \tag{4.3.7}$$

Proof: Define the error between the sensor system and observer as

$$\tilde{x}_k = x_k - \hat{x}_k = Mx_k - z_k \tag{4.3.8}$$

where $M = I + EC$. From (4.3.3), the error dynamics is

$$\tilde{x}_{k+1} = N_k \tilde{x}_k + (MA - LC - NM)x_k + (MB - R)u_k$$
$$+ MD_f (f(x_k) - f(\hat{x}_k)) + MDd_k \tag{4.3.9}$$

If $MA - LC - NM = 0$, $MB - R = 0$, $MD \neq 0$ and system (4.3.10) is asymptotically stable,

$$\tilde{x}_{k+1} = N\tilde{x}_k + MD_f (f(x_k) - f(\hat{x}_k)) \tag{4.3.10}$$

then observer (4.3.3) is a fault detection observer. Redefine the matrix variables as

$$N = MA - XC, \; L = X(I + CE) - MAE \tag{4.3.11}$$

where $X = L + NE$. Choose a Lyapunov functional as

$$V_k = \tilde{x}_k^T P \tilde{x}_k \tag{4.3.12}$$

where P is a symmetric positive matrix. Asymptotic stability of system (4.3.10) requires

$$\Delta V_k = V_{k+1} - V_k < 0 \tag{4.3.13}$$

According to system (4.3.10)

$$\Delta V_k - (\tilde{f}_k^T \tilde{f}_k - \tau^2 \tilde{x}_k^T \tilde{x}_k) = \eta_k^T \Pi \eta_k \tag{4.3.14}$$

where $\tilde{f}_k = f(x_k) - f(\hat{x}_k)$, $\eta_k^T = [\tilde{x}_k^T \; \tilde{f}_k^T]$ and

$$\Pi = \begin{bmatrix} \tau^2 I + N^T P N - P & N^T P M D_f \\ D_f^T M^T P N & D_f^T M^T P M D_f - I \end{bmatrix} \tag{4.3.15}$$

By noting that $\Pi < 0$ indicates $\Delta V_k < (\tilde{F}_k^T \tilde{F}_k - \tau^2 \tilde{x}_k^T \tilde{x}_k)$. And then, according to Lipschitz condition (4.3.4), $\Delta V_k < 0$ is obtained. Thus the error dynamics $\tilde{x}_k = x_k - \hat{x}_k$ asymptotically converge to zero as $k \to \infty$.

However, due to the couplings of unknown matrices N, P, and M, $\Pi < 0$ is a nonlinear condition. In order to solve this problem, some linearization techniques are adopted to convert the nonlinear condition to linear case. Applying Schur complement equivalence to $\Pi < 0$ yields

$$\begin{bmatrix} \tau^2 I - P & 0 & N^T P \\ 0 & -I & D_f^T M^T P \\ PN & PMD_f & -P \end{bmatrix} < 0 \tag{4.3.16}$$

By substituting $N = MA - XC$ and $M = I + EC$ in (4.3.16), then replacing $E^T P$ and $X^T P$ with $\overline{E}^T$ and $\overline{X}^T$ respectively, (4.3.16) is written as the following equivalent form.

$$
\begin{bmatrix}
\tau^2 I - P & 0 & A^T P + A^T C^T \overline{E}^T - C^T \overline{X}^T \\
* & -I & D_f^T P + D_f^T C^T \overline{E}^T \\
* & * & -P
\end{bmatrix} < 0 \qquad (4.3.17)
$$

If condition (4.3.17) has a feasible solution, the observer parameters are recovered as (4.3.7). This completes the proof. $\qquad\square$

Remark 4.4 *According to the proof, matrix M is expressed as $M = I + EC$. From (4.3.2), it is obtained that $MD = D + ECD = D \neq 0$. Thus, the condition $MD \neq 0$ in Theorem 4.1 is always satisfied for sensor system (4.3.1).*

Conforming to the Theorem 4.1, the fault detection observer design problem can be solved by checking the feasibility of condition (4.3.6). If feasible, a suitable fault detection observer is yielded from (4.3.7). Apart from the unknown matrices P, $\overline{E}$, and $\overline{X}$, Lipschitz constant τ is another important parameter deciding the existence of feasible solution. In general, the Lipschitz constant τ cannot be arbitrarily large. Referring to the Theorem 4.1, solution to give the maximum admissible Lipschitz constant satisfying the condition (4.3.6), which represents the conservativeness of the fault detection observer design, is stated as follows.

Corollary 4.1 *The maximum admissible Lipschitz constant τ such that the condition (4.3.6) holds can be obtained via the optimal solution of the following convex optimization problem:*

$$
\min_{P, \overline{E}, \overline{X}} \lambda
$$

$$
subject\ to\ \ (4.3.18),\ \ with\ \lambda \equiv \frac{1}{\tau^2} > 0
$$

$$\begin{bmatrix} -P & 0 & A^T P + A^T C^T \overline{E}^T - C^T \overline{X}^T & I \\ * & -I & D_f^T P + D_f^T C^T \overline{E}^T & 0 \\ * & * & -P & 0 \\ * & * & * & -\lambda I \end{bmatrix} < 0 \qquad (4.3.18)$$

The maximum admissible Lipschitz constant is given by $\tau^* = \sqrt{\frac{1}{\lambda^*}}$, *where* λ^* *is the optimal value of* λ, *and the corresponding fault detection observer is recovered from (4.3.7).*

Based on the designed fault detection observer from Theorem 4.1, the residual signal is obtained $r_k = y_k - C\hat{x}_k$. In order to identify the fault signal exactly from the residual signal r_k, a residual evaluation strategy consisting of the evaluation function, threshold and fault classification is proposed [114, 115]. Here, choose a sliding time-window norm as the evaluation function

$$J(r_k) = \frac{1}{\Delta k} \sqrt{\sum_{k=k_0}^{k_n} r_k^T r_k}, \Delta k = k_n - k_0 + 1 \qquad (4.3.19)$$

The corresponding threshold is designed

$$J_{\text{th}} = \mu \sup_{\Delta_k = 0} J(r_k) + \beta \qquad (4.3.20)$$

Positive scalars $\mu \geq 1$ and $\beta \geq 0$ are weight coefficients. The fault detection sensitivity can be altered by adjusting the weight coefficients and sliding time-window length. According to the evaluation function (4.3.19) and threshold (4.3.20), the logic of fault detection is

$$\begin{cases} J(r_k) \geq J_{\text{th}} \implies \text{Fault Occurs} \implies \text{Alarm} \\ J(r_k) < J_{\text{th}} \implies \text{Fault Free} \end{cases} \qquad (4.3.21)$$

The difference of absolute motion between the fault-free case and faulty case has been given by the residual signal r_k. Thus, when a fault detection alarm is triggered, it is possible to conduct a fault level evaluation by analyzing the envelope of residual signal r_k. Furthermore, the type of fault can be identified from the fault level. But in this thesis, only simple fault detection is considered, the identification of fault level and type will not be included.

The fault detection method has been summarized as an algorithm given in Algorithm 4.2.

Algorithm 4.2: Algorithm for Fault Detection

1: Choose a appropriate τ from (4.3.5).

2: Solve the following convex optimization problem to obtain a feasible solution P, $\overline{E}$, and $\overline{X}$.

$$\text{s.t. } P > 0, \ (4.3.6)$$

$$\text{for } P, \overline{E}, \overline{X}, A, C \text{ and } \tau$$

3: Calculate the fault detection observer parameters as (4.3.7).

4: Implement the fault detection observer and output r_k.

5: Design the threshold J_{th} from (4.3.20) at fault-free case.

6: If the evaluation function $J(r_k) \geq J_{\text{th}}$ is satisfied, then trigger alarm and even classify fault level from residual r_k.

Remark 4.5 *Algorithm 4.2 presents a real-time fault detection strategy which is implemented by applying the bio-inspired vibration sensor and constructing the fault detection observer. Compared with acceleration signal, sometimes it is more reasonable to use the absolute motion to describe the degree of structure damage caused by fault [116]. Because the absolute motion can given more information on the structural deformation, which can be used to analyze the operating condition and health status of the monitored object.*

4.4 Experimental results

In this section, the first stage will estimate the damping coefficient by applying the parameter estimation method in Algorithm 4.1. Then, based on the obtained comparatively exact model of the sensor system, the second stage will construct the model-based fault

detection as depicted in Algorithm 4.2 and an experiment will be conducted to demonstrate this fault detection method. The parameter values are given in Table 4.3.

Table 4.3: The bio-inspired sensor parameters

Symbol	Description	Value
m	loading mass (kg)	0.21
L	length of rod (m)	0.10
α	initial angle (rad)	0.13π
n	number of layers	3
k_h	spring stiffness (N/m)	390
T_s	sampling period (s)	0.001
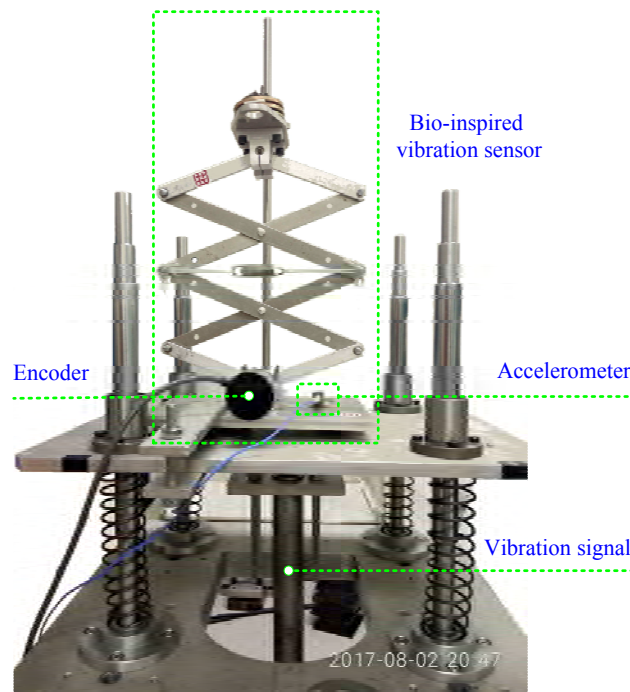
Fig. 4.5: Bio-inspired sensor prototype and experimental platform

4.4.1 Absolute vibration displacement measurement

In this experiment, the input excitation is generated from a shaker. Here, a sinusoid excitation is selected as input. The shaker requires a short period to generate the standard sinusoid signal. Thus the input excitation during the initial period is not a standard sinusoid excitation but a sinusoid-like signal. State variables and input signal are measured by using laser, encoder and accelerometer. As shown from Fig.4.6 to Fig.4.8, the
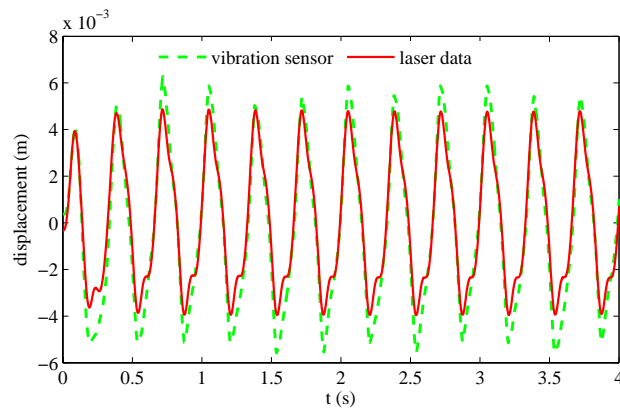
Fig. 4.6: Absolute displacement measurement at 3 Hz single frequency excitation
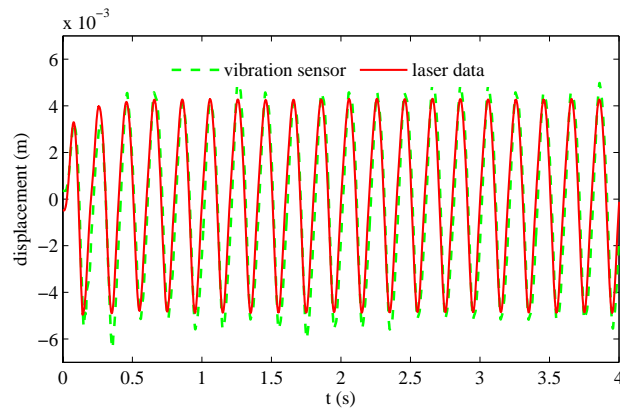
Fig. 4.7: Absolute displacement measurement at 5 Hz single frequency excitation
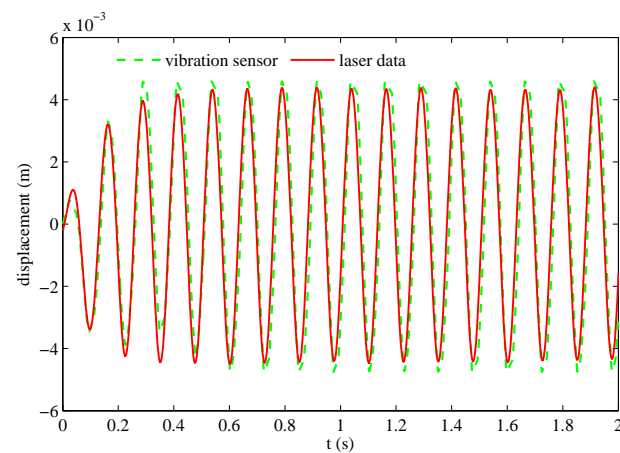
Fig. 4.8: Absolute displacement measurement at 8 Hz single frequency excitation

measurement results at single frequency excitation are illustrated, which demonstrates that this bio-inspired vibration sensor can obtain a high accuracy measurement when the excitation frequency is higher than 5 Hz.

Remark 4.6 *Although only single frequency excitation is used in the experiment, it can be obtained from the measurement results that the measurement accuracy is obviously improved when the excitation frequency is far away from the resonant frequency of the sensor system. The conclusion can be straightly extended to the multi-frequency case. If the main frequency component of multi-frequency excitation signal is far away from the resonant frequency of the sensor system, an accurate measurement can also be achieved.*
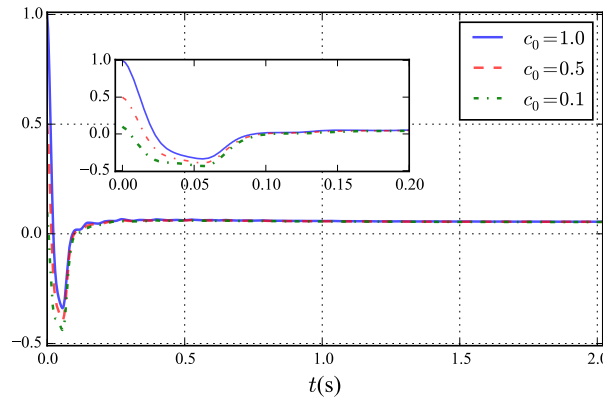
Fig. 4.9: Parameter estimation result with different initial guess

For the Algorithm 4.1, three different initial guesses for rotational damping coefficient are considered: $c_0 = 1.0$, $c_0 = 0.5$ and $c_0 = 0.1$. As depicted in Fig. 4.9, all the estimation results converge to a constant value at almost 0.052 after $t = 0.5$ s, which indicates that Algorithm 4.1 is not sensitive to the initial value. Thus, the estimation value of rotational damping coefficient is $c = 0.052$. State variables and error dynamics are shown in Fig. 4.10. x_k^1 and x_k^2 are the real measurement. $\hat{x}_k^1$ and $\hat{x}_k^2$ are the system state from the predictor. e_k^1 and e_k^2 are the error dynamics between the real measurement and predictor. The errors may come from the unmodeled dynamics and disturbances. It can be observed that the state variables of model are in basic agreement with the real measurement, which demonstrates the effectiveness of Algorithm 4.1.
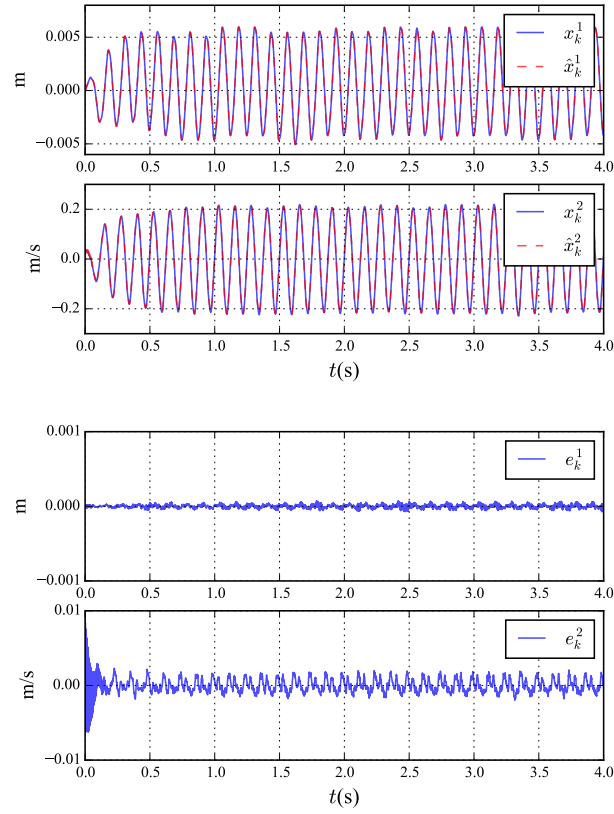
Fig. 4.10: System state and error dynamics

4.4.2 Fault detection using absolute vibration displacement

By applying Theorem 4.1 with a Lipschitz constant $\tau = 80$, the parameters of fault detection observer are obtained

$$
\begin{aligned}
N &= \begin{bmatrix} 0 & 0.0001 \\ -0.0002 & 0.2859 \end{bmatrix}, R = \begin{bmatrix} 0 \\ -0.001 \end{bmatrix} \\
M &= \begin{bmatrix} 0.0847 & 0 \\ -681.5633 & 1 \end{bmatrix}, L = \begin{bmatrix} 0.1424 \\ -486.7297 \end{bmatrix} \\
E &= \begin{bmatrix} -0.9153 \\ -681.5633 \end{bmatrix}
\end{aligned}
\tag{4.4.1}
$$

The conservativeness of the fault detection observer design method proposed is evaluated by calculating the maximum admissible Lipschitz constant. As shown in Table 4.4, $\tau_{\max}$

obtained by Corollary 4.1 of this thesis is larger than that obtained in Ref. [1]. To further illustrate the conservativeness on the structure parameters, the maximum admissible Lipschitz constant with different spring stiffness $k_h \in [380\ 400]$ and loading mass $m \in [0.18\ 0.25]$ is depicted in Fig. 4.11, from which it can be easily seen that Corollary 4.1 can always provide larger $\tau_{\max}$ than that of Ref. [1] on the whole given parameter space. Thus, the fault detection observer design method of this thesis is less conservative. And the design flexibility can benefit from the low conservative method.

Table 4.4: Comparison of the maximum admissible Lipschitz constant

Method	The maximum value of τ
Method in Ref. [1]	301.2329
Corollary 4.1 in this thesis	703.5384
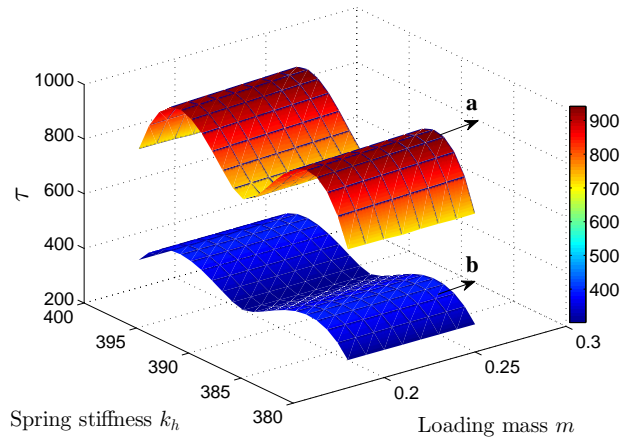
Fig. 4.11: Maximum admissible Lipschitz constant with different m and k_h, **a**: Corollary 4.1 in this thesis, **b**: Method in Ref. [1].

This fault detection experiment is conducted on the vibration platform as shown in Fig. 4.5. Excitation input is a sinusoid signal with 8Hz generated from shaker. The absolute vibration motion is measured through the optical encoder. The relationship of vibration motion and rotation angle measured by encoder has been presented in (4.1.7). The input signal is measured by the accelerometer. Fig. 4.12 shows the measurement of absolute vibration motion under the fault free case and faulty case. For faulty case, fault signal occurs at $t \in [6.65\ 6.75]$ s.

From the sensor parameters in Table 4.3, the natural frequency can be approximated as
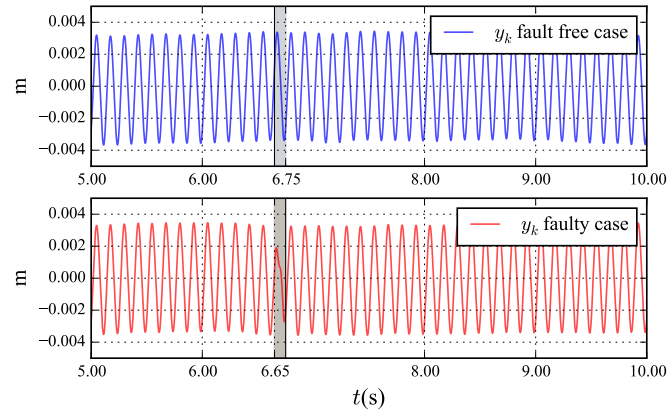
Fig. 4.12: Absolute vibration motion y_k

$f_0 \approx 0.98$ Hz by (4.1.6). According to the motion transmissibility property of the bio-inspired vibration sensor, when the frequency of base excitation is larger than $\sqrt{2}$ times the natural frequency, the sensor has a high-accuracy measurement of absolute motion by using y_r instead of y_a. Thus, the absolute motion can be given through measuring y_k. Next, we will make use of the measured absolute motion and fault detection observer (4.4.1) to construct a fault detection system.
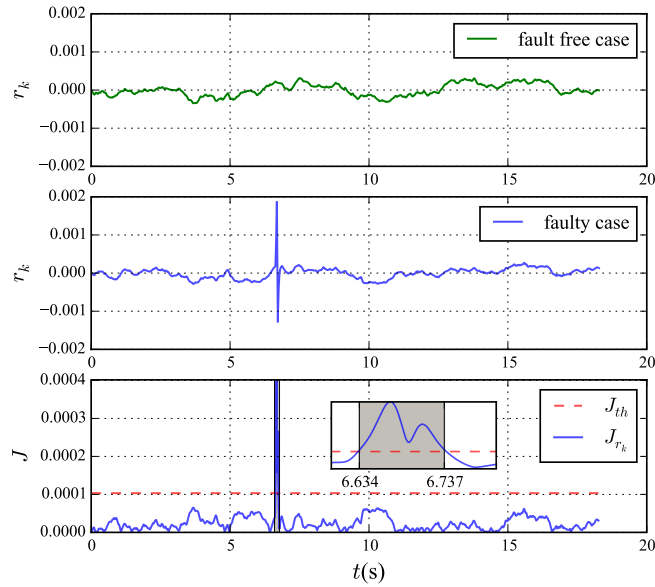
Fig. 4.13: Residual response and fault detection result
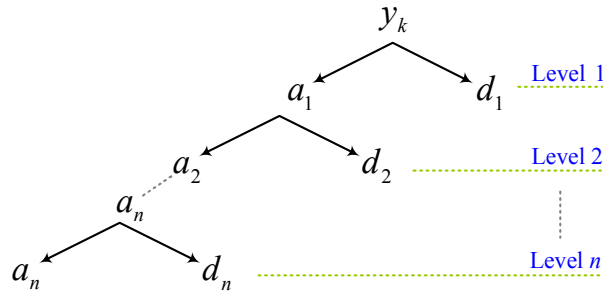
Fig. 4.14: n levels multi-resolution wavelet decomposition
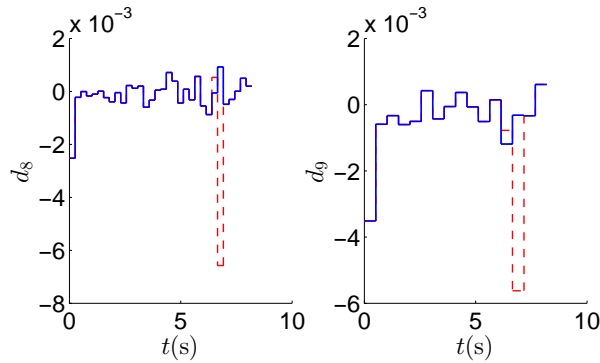
Fig. 4.15: Parts of wavelet decomposition results (blue solid line is fault-free case, red dotted line is faulty case).

As depicted in Fig. 4.4, the residual signal r_k is generated by the difference between absolute motion y_k and its estimation $\hat{y}_k$. Based on the fault detection observer (4.4.1), the estimation of y_k is expressed as $\hat{y}_k = C\hat{x}_k$. The responses of residual signal r_k and evaluation function $J(r_k)$ are shown in Fig. 4.13. The threshold of fault detection system here is set as $J_{\text{th}} = 1.032 \times 10^{-4}$. The characteristic frequency of the fault signal is covered by the excitation input and its harmonics. Due to the fast time-varying characteristic, the spectrum power of faulty case in some high frequency is stronger than that of fault-free case. It is difficult to locate the fast time-varying fault by using the simple spectrum analysis. The detection of the fast time-varying fault can be realized by adopting some advanced and complicated methods, such as the short time Fourier transform (STFT) [47] and the wavelet-based method [48]. The prior knowledge on the fast time-varying fault is generally unavailable. In order to obtain a high spectral resolution, the STFT method needs a long acquisition time, which will increase the computational complexity and degrade the real-time performance. Wavelet-based method requires a precise adjustment of the bands of decomposition to locate the fault signal. Thus, real-time and

accuracy performance of fault detection is difficult to be simultaneously guaranteed by using the frequency-based or wavelet-based fault detection methods, especially for the weak fault with fast time-varying.

To further demonstrate the advantage of the proposed fault detection approach, multi-resolution wavelet-based method in Ref. [48] is applied to analyse the measured signal y_k. The entire decomposition procedure of multi-resolution wavelet with n levels is illustrated in Fig. 4.14. For the convenience of conducting wavelet decomposition, only $2^{13} = 8192$ points during $t \in [0, 8.192)$ s are selected. Here the decomposition level is $n = 13$. Parts of wavelet decomposition results (d_8, and d_9) are shown in Fig. 4.15. Obviously, the fault can be located by detecting the singular value of the decomposition components. It is worth pointing out that wavelet-based fault detection is not a real-time method, which requires the acquisition of entire off-line data. Additionally, in order to identify the singular value induced by fault signal, it is necessary to do the decomposition until the last level. Thus, as the data volume increases, the wavelet-based fault detection method will be limited to the computational complexity. Fig. 4.16 shows computational time for different wavelet decomposition level on a computer with Intel Core2 processors @2.20 GHz @2.20 GHz and 3.0 GB DDR2 memory. However,

Table 4.5: Fault detection results

Method	Result	Computational Time	Real-time
Wavelet (d_8)	$t \in [6.65 \ 6.92]$ s	0.0165 s	Off-line
Wavelet (d_9)	$t \in [6.66 \ 7.17]$ s	0.0178 s	Off-line
Algorithm 4.2	$t \in [6.63 \ 6.74]$ s	< 0.001 s	On-line

using the proposed fault detection strategy in Algorithm 4.2, on-line fault detection becomes possible. Fault detection performance is depicted in Fig. 4.13, where alarm is triggered and removed at $t = 6.634$ s and $t = 6.737$ s, respectively. The real fault signal occurs at $t \in [6.65 \ 6.75]$ s. Table 4.5 shows the comparison of fault detection results between multi-resolution wavelet-based method and Algorithm 4.2. In level 8 decomposition, the singular value appears at $t \in [6.65 \ 6.92]$ s. In level 9, the singular value arises at $t \in [6.66 \ 7.17]$ s. These results illustrates that the occurrence time of fault identified by Algorithm 4.2 is more exact than multi-resolution wavelet-based

method. For multi-resolution wavelet-based method, downsampling in decomposition is a key factor affecting the fault detection exactness. Moreover, compared with the
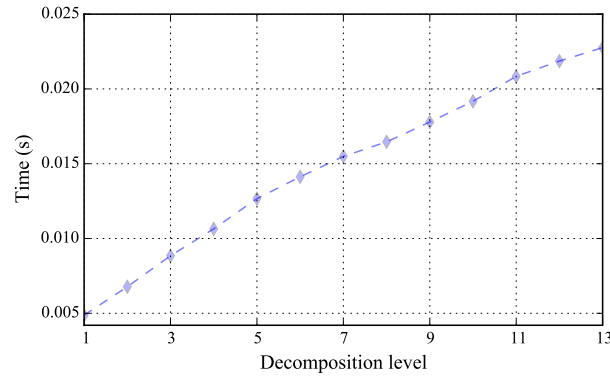
Fig. 4.16: Computational time for different decomposition level

wavelet-based method, the computational complexity of the fault detection approach in Algorithm 4.2 always remains constant (less than 0.001 s in one step) due to the real-time performance. Many detections and monitoring applications (e.g., building, bridge, and railway) can benefit from this real-time fault detection strategy by using the bio-inspired vibration sensor.

4.5 Concluding remarks

In the chapter, a novel bio-inspired vibration sensor for the real-time absolute motion measurement has been discussed, and its application for more reliable fault detection has been presented. Compared with some existing methods, the superiority of this bio-inspired sensor method lies in the following points: (1) This bio-inspired sensor has advantages of real-time performance, low cost and flexibility in comparison to traditional methods of absolute motion measurement using accelerometer and laser. For instance, the problems of error accumulation and real-time performance induced by traditional measurement method using integration of accelerometer data can be effectively eliminated. (2) By taking full advantage of the bio-inspired vibration sensor in real-time measurement of absolute vibration motion, a model-based fault detection algorithm has been proposed to cope with the on-line fault detection problem. Importantly, the fault

detection method of this chapter is less conservative and more reliable. (3) The detection results obtained from the on-line fault detection method of this chapter are more exact and more sensitive than other methods such as the multi-resolution wavelet-based method. (4) The on-line fault detection method is very simple to implement and the computational complexity of the fault detection approach in Algorithm 4.2 always remains very small.

5 Robust navigation control of a tracked mobile robot with uncertain disturbance

A tracked mobile robot adopting the bio-inspired structure as passive suspension system will be introduced in this chapter. Equipped with the novel bio-inspired suspension, the loading capacity, riding comfort and obstacle negotiation capability can be significantly enhanced and the tracked robot can be applied to various rough ground environments. In addition, autonomous navigation using laser radar sensor will be developed. A NMPC based architecture will be adopted for optimizations of trajectory tracking.

Compared to the local disturbance, the global trajectory tracking has slower process dynamic. Performing the optimization of global trajectory tracking at each lifting period is not necessary. A natural way is to separate the optimizations of global- and local-trajectory tracking on different time scales. An alternative method to overcome the above trade-off between the computational complexity and local dynamic optimization performance is to adopt multi-layer NMPC scheme. Although the multi-layer NMPC architecture has been successfully applied in various industry areas [117–119]. There is a paucity of literature on the multi-layer NMPC architecture for the trajectory tracking control of mobile robot with high dynamics. In this way, the upper layer NMPC is performed at a low frequency to optimize the global trajectory tracking performance, and the lower layer NMPC is conducted at a high frequency to capture the local dynamics.

The chapter is organized as follows. Section 5.1 starts with model description and analy-

sis of the bio-inspired structure and the novel passive bio-inspired suspension. In Section 5.2, the model predictive control methods are applied to optimize the trajectory tracking for autonomous navigation. Some experimental results are presented in Section 5.3 to demonstrate the effectiveness and applicability of the autonomous navigation performance of the tracked mobile robot with the novel passive bio-inspired suspension. Finally, Section 5.4 concludes the chapter.

5.1 Model description and analysis of the bio-inspired suspension

5.1.1 Design concept

It has been proven that this bio-inspired structure can provide an excellent quasi-zero-stiffness characteristic with high static stiffness, low dynamic stiffness and broad frequency range of vibration isolation [53, 56, 73], which means that both high loading capacity and excellent vibration isolation performance can be simultaneously guaranteed. Compared with the conventional mass-spring-damper (MSD) system, this bio-inspired structure with the above advantages provides a feasible solution to overcome the inherent trade-off between the loading capacity and vibration isolation performance. Importantly, this bio-inspired structure is easy to implement and does not require high precision at manufacturing.

Remark 5.1 *This bio-inspired structure is mainly developed for the isolation of vertical motion. In practical structure, a support rod will be placed along the vertical centerline to limit the motion and guarantee that the structure works in the effective range. Thus the deformation on the bio-inspired structure is assumed to be symmetrical. Compared to the asymmetric structure, the symmetric structure is easier to implement and is more stable. More detailed analysis on asymmetric structure can refer to [56], [120].*

5.1.2 Structural analysis

As shown in Fig.5.1, when the structure is compressed into the quasi-zero-stiffness range, vertical motion almost does not transmit force to the top platform. Heavier loading is helpful to compress the structure into the quasi-zero-stiffness range. But the linear stiffness still has the same force transmission during the whole motion range. It is worth pointing out that the quasi-zero-stiffness are generated from the special geometric relationship of this bio-inspired structure rather than the nonlinear spring. It means that using the linear components can realize the nonlinear quasi-zero-stiffness vibration isolator, which is one of the obvious advantages of this bio-inspired structure.
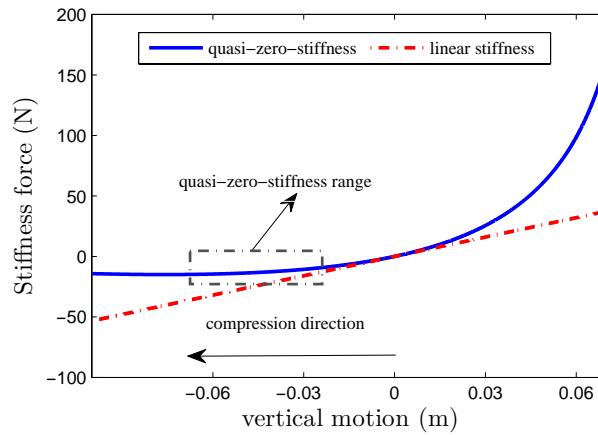
Fig. 5.1: Comparisons of quasi-zero-stiffness and linear stiffness

Through Taylor series expansion of nonlinear stiffness term at zero equilibrium, the natural frequency of the bio-inspired structure is approximated as

$$f_0 = \frac{\tan\alpha}{2\pi n}\sqrt{\frac{k_h}{m}} \tag{5.1.1}$$

As can be seen from (5.1.1), the natural frequency is determined by the spring stiffness, loading mass, assembly angle and layer number. Apart from adjusting the spring stiffness and loading mass, increasing the layer number and decreasing the assemble angle can effectively lower the natural frequency. This reveals the flexibility on the parameter design. In addition, higher loading will bring smaller assembly angle and thus lower dynamic stiffness can be obtained, upon which the bio-inspired structure become much

softer and meanwhile maintain high loading capacity.

5.1.3 Simulation and experimental verification

To further demonstrate the advantage of the bio-inspired structure, comparison of vibration isolation performance between the linear MSD system and the bio-inspired structure is conducted. As shown in Fig.5.2 (a), the Seekur mobile robot from Omron Adept Technologies, Inc. equips with the passive MSD suspension to provide the capability of traversing very rugged terrain [121]. For the bio-inspired structure with the parameters $m = 0.5$ kg, $n = 3$, $L = 0.05$ m, $k_h = 5000$ N/m, $\alpha = 50°$, the natural frequency obtained from (5.1.1) is about 6.3 Hz. The natural frequency of the linear MSD system with the same loading mass 0.5 kg and spring stiffness 5000 N/m is about 15.6 Hz. The simulation results including the acceleration response under the random excitation and the displacement transmissibility are depicted in Fig.5.3. It can be seen from Fig.5.3 that the bio-inspired structure can achieve better vibration isolation performance and much lower natural frequency than the linear MSD system with the same conditions of loading mass and stiffness.
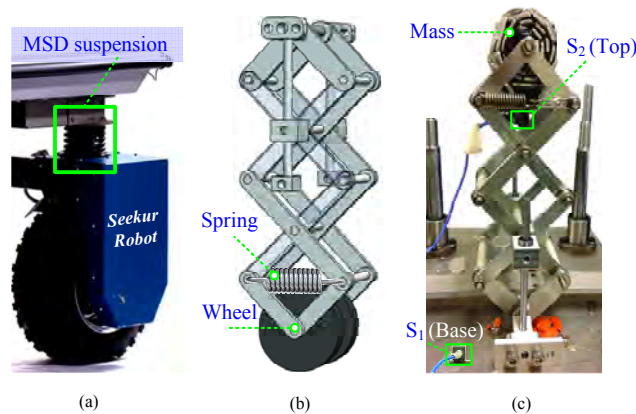
Fig. 5.2: (1) Passive MSD suspension. (b) Bio-inspired suspension. (c) Experiment prototype.

The novel passive suspension system using the 3 layer bio-inspired structure is shown in Fig.5.2 (b). The bio-inspired structure is placed between the support wheel and robot body to absorb the vibration disturbance from the rough ground or obstacle crossing and provide a stable upper platform. The experiment prototype is shown in Fig.5.2
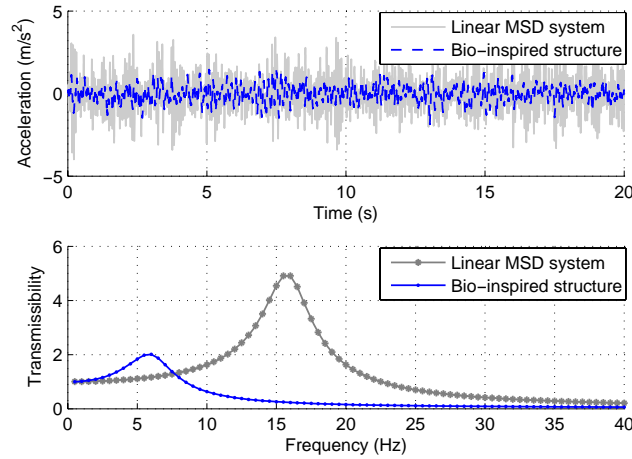
Fig. 5.3: Simulation results: acceleration response and transmissibility
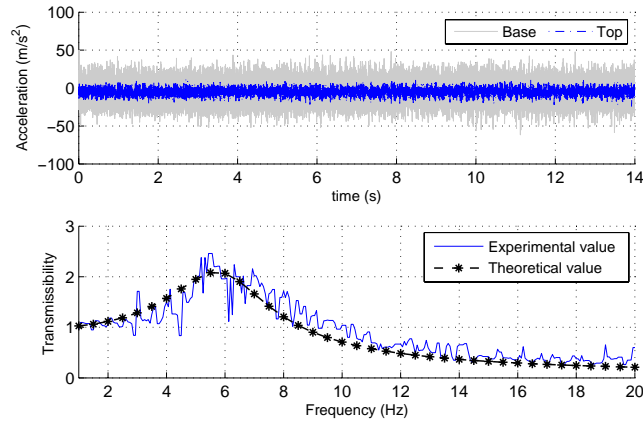
Fig. 5.4: Vibration experiment results of the suspension prototype

(c). Two accelerometers are respectively placed on the base and the top to measure the excitation and response. A random excitation generated by the shaker is applied to the base. The results of vibration experiment are depicted in Fig.5.4. The experimental value of transmissibility is obtained by the ratios of the two accelerations in the frequency domain. The theoretical value of transmissibility is in basic agreement with experimental value. It indicates that using the above model to analyze the dynamics of the bio-inspired structure is reasonable. The experimental results of Fig.5.4 demonstrate that the vibration amplitude on the top platform of the passive bio-inspired suspension can be significantly reduced.

The single passive bio-inspired suspension can be view as a soft "leg", which can be

applied to both tracked mobile robots and wheeled mobile robots. The tracked mobile robot has better obstacle negotiating ability and also suffers stronger vibration and shock when crossing the obstacle. The purpose of this chapter is to construct the bio-inspired suspension for the tracked mobile robot to obtain a more stable robot platform. Through combining multiple passive bio-inspired suspension systems together, the loading capacity and continuous-obstacle crossing ability of the tracked mobile robot can be significantly improved. Thus, a tracked mobile robot equipped with multiple bio-inspired suspensions similar to multi-legged animal or insect will be introduced in the next section.

5.2 Robust navigation using model predictive control method

5.2.1 Hardware

The overall configuration of the tracked mobile robot equipped with two-layer bio-inspired passive suspension is shown in Fig.5.5. Each side uses five individual bio-inspired structures as the passive suspension. The loading of the robot is uniformly distributed to each bio-inspired structure. Benefiting from the excellent isolation performance of the bio-inspired structure, the novel passive suspension system can efficiently absorb the strong shock and hence guarantee the steady and smoothness when the robot moves on rough ground or negotiates obstacles.

This tracked mobile robot with equivalent load 10 kg is driven by two DC motors connecting to optical encoders, similar to the differential wheeled robot. The measurement and control of the motor speed are implemented by motor driver. The transmission between the motor driver and control board is through the RS232 serial communication. A low speed two dimension laser radar (RPLIDAR A2) is used to generate an outline map of surrounding environment. The parameters of the RPLIDR A2 are as follows: detection range (360 degree omnidirectional laser range and 18 meters range radius),

resolution (1 degree angular resolution and 0.2 centimeter distance resolution), and frequency (10 Hz). An inertial measurement unit (IMU) is also used for the measurement of acceleration and angular velocity. The control board is the RASPBERRY PI 3 MODEL B with quad core 1.2GHz 64bit CPU and 1GB RAM.
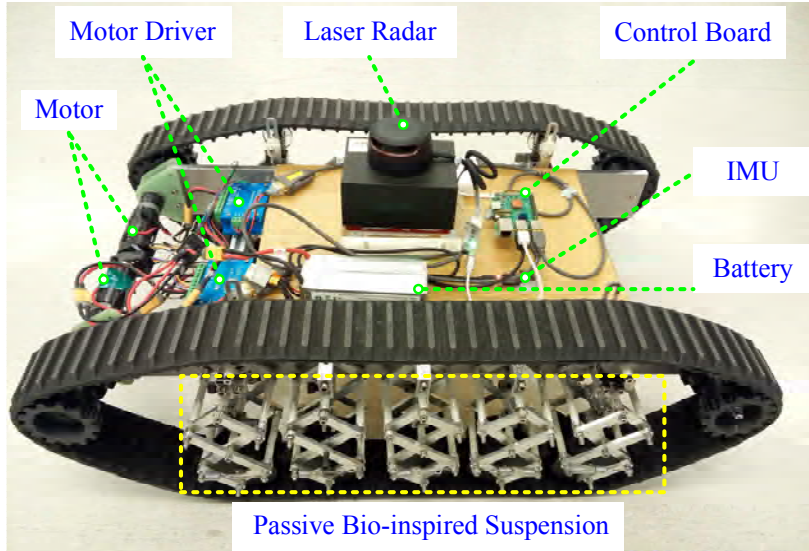
Fig. 5.5: Overall configuration of the tracked mobile robot
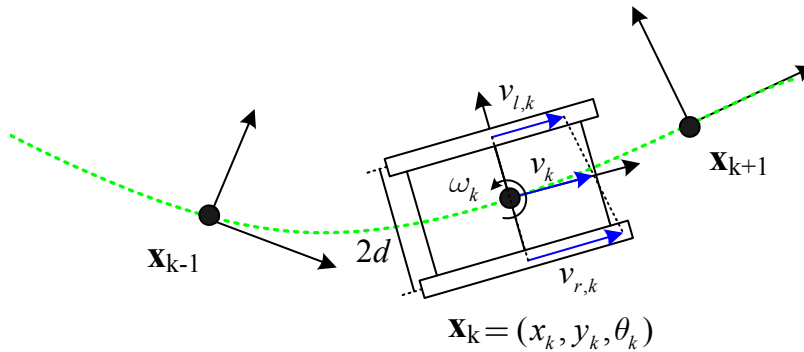
Fig. 5.6: Robot pose definition: the motion is decomposed into translation v_k and rotation w_k.

5.2.2 Kinematic model omitting slippage

For the dynamic equation of the tracked mobile robot, we need to know the exact friction force between the crawler and ground in advance. However, the friction force is closely
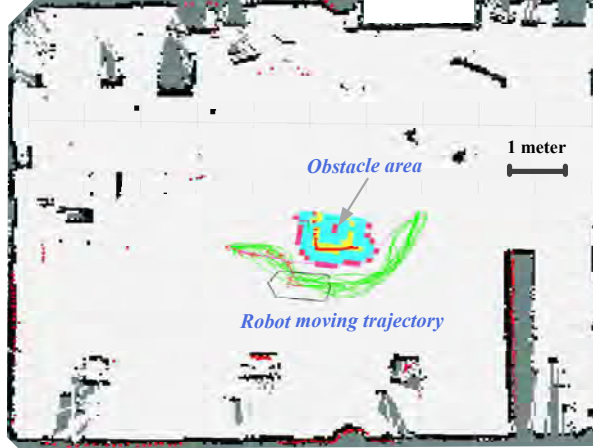
Fig. 5.7: Visualization map constructed by using the laser radar data
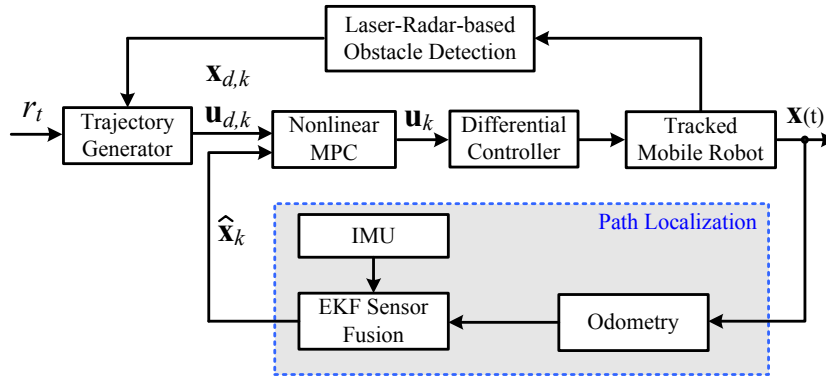
Fig. 5.8: Single layer NMPC

related to the ground environment and hence it is difficult to directly obtain the accurate measurement. Particularly for obstacle crossing, the friction force is highly uncertain and dependent on the process of obstacle crossing. Thus, the control methods combining the dynamic and kinematics equations cannot be applied to the autonomous navigation of this tracked mobile robot [122]. On the other side, the navigation method only using kinematics equation is simple, easy to implement.

According to the robot pose definition in Fig.5.6, the kinematics equation of the tracked mobile robot without considering the slippage is described as

$$\mathbf{x}_{k+1} = \mathbf{x}_k + \mathbf{f}(\mathbf{x}_k, \mathbf{u}_k) \qquad (5.2.1)$$
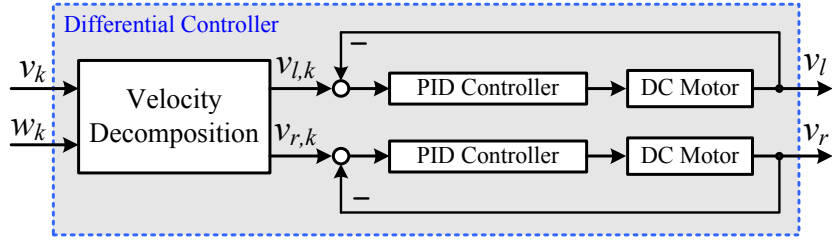
Fig. 5.9: Structure of differential controller

$$\mathbf{f}(\mathbf{x}_k, \mathbf{u}_k) = T_u \begin{bmatrix} \cos\theta_k & 0 \\ \sin\theta_k & 0 \\ 0 & 1 \end{bmatrix} \mathbf{u}_k$$

where $\mathbf{x}_k = (x_k, y_k, \theta_k)$ is the robot pose at time instance k, T_u is the control interval determined by the processing latency of mapping and trajectory generating, $\mathbf{u}_k = (v_k, w_k)$ is the control input including the linear velocity v_k and angular velocity w_k, which are determined by the velocities of left- and right-crawlers

$$v_k = \frac{v_{r,k} + v_{l,k}}{2}, \ \omega_k = \frac{v_{r,k} - v_{l,k}}{2d} \tag{5.2.2}$$

The NMPC will be applied to the autonomous navigation of this tracked mobile robot. For given starting and target positions, the globally optimal reference trajectory is generated by using the Dijkstra algorithm [123]. The reference trajectory and control is adjusted dynamically by integrating the laser radar and timed elastic band approach [124], thus this tracked mobile robot has the ability of avoiding the dynamic moving obstacle that it cannot pass over. The RVIZ visualization map constructed by using the laser radar data is shown in Fig.5.7. The black and white map with the resolution 0.05 meters/pixel is generated by scanning the whole environment in advance. The red point cloud is the scanning result of laser radar. The starting and target position can be set through this visualization map and the moving trajectory can also be observed from the visualization map.

5.2.3 Single-layer control

The structure of the single layer NMPC is shown in Fig.5.8. An odometry is implemented by using the optical encoders (connecting to the actuators) for the estimation of robot pose in GPS denied environment. By resorting to the extended Kalman filter [125], the sensor fusion of odometry and IMU can provide more accurate estimation of the robot pose. r_t is the target position. $\mathbf{x}_{d,k}$ is the reference trajectory, $\mathbf{u}_{d,k}$ is the desired input. $\mathbf{u}_k$ is the real input. With the differential controller, the control input $\mathbf{u}_k$ is decomposed into the velocities of left- and right-crawlers. To achieve the desired velocities, two PID controllers are adopted for the speed control of motors.

$$v_{r,k} = v_k + d\,\omega_k, \ v_{l,k} = v_k - d\,\omega_k \tag{5.2.3}$$

Next, a nonlinear model predictive controller will be designed to optimize the navigation performance of this tracked robot over a given time-horizon. The cost function of predicted state and input sequence $\mathbf{x}_{k|t}$, $\mathbf{u}_{k|t}$ to be minimized at time instant t is defined as

$$J_u\big(\mathbf{x}_{k|t}, \mathbf{u}_{k|t}\big) = \sum_{k=0}^{N-1} \big(||\mathbf{x}_{k|t} - \mathbf{x}_{d,k}||^2_{\mathbf{Q}_1} + ||\mathbf{u}_{k|t} - \mathbf{u}_{d,k}||^2_{\mathbf{Q}_2}\big)$$
$$+ ||\mathbf{x}_{N|t} - \mathbf{x}_{d,N}||^2_{\mathbf{Q}_3} \tag{5.2.4}$$

where $\mathbf{x}_{d,k}$ and $\mathbf{u}_{d,k}$ are respectively the reference trajectory vector and desired control, N is the horizon, operator $||\cdot||^2_{\mathbf{Q}}$ is defined as $||\mathbf{x}_k||^2_{\mathbf{Q}} = \mathbf{x}_k^T \mathbf{Q} \mathbf{x}_k$ ($\mathbf{Q}$ is a symmetric semi-positive definite matrix). $\mathbf{Q}_1$, $\mathbf{Q}_2$, and $\mathbf{Q}_3$ refer to the corresponding weighting matrices of the system state, control input, and terminal state. In this paper, the prediction process is performed at the same frequency of controller and the control horizon equals the prediction horizon. The control input constraints $\mathbb{U}$ are given by

$$\mathbb{U} = \left\{\mathbf{u} \in \mathbb{R}^2 | \begin{bmatrix} v_{\min} \\ \omega_{\min} \end{bmatrix} \leq \mathbf{u} \leq \begin{bmatrix} v_{\max} \\ \omega_{\max} \end{bmatrix}\right\} \tag{5.2.5}$$

where $v_{\min}$ and $v_{\max}$ are linear velocity limits, $\omega_{\min}$ and $\omega_{\max}$ are angular velocity limits. The nonlinear model predictive control scheme will repeatedly solve the following optimal control problem:

$$\min_{\mathbf{x},\mathbf{u}} J_u(\mathbf{x}_{k|t}, \mathbf{u}_{k|t}) \tag{5.2.6}$$

$$\text{s.t. } \mathbf{x}_{k+1|t} = \mathbf{f}(\mathbf{x}_{k|t}, \mathbf{u}_{k|t}), \ \mathbf{u}_{k|t} \in \mathbb{U}, \ \mathbf{x}_{0|t} = \mathbf{x}(t)$$

The optimal control problem above can be solved by resorting to the Gauss-Newton method [126], [127], which is an efficient numerical method for NMPC. In this paper, the NMPC is used for the trajectory tracking control with reference trajectory and desired control input, thus the residual norm is small. The contraction rate of the Gauss-Newton method is fast when the residual norm is small. Only the first optimal control $\mathbf{u}_{0|t}^*$ will be applied to the tracked mobile robot. This process will be repeated in the next time step in a receding horizon fashion. The single layer NMPC is summarized in Algorithm 5.1.

Algorithm 5.1: Single Layer NMPC

---

initialize NMPC ;
input data: $\mathbf{x}_{d,k}, \mathbf{u}_{d,k}$ and $\hat{\mathbf{x}}_k$;
output result: optimal control $\mathbf{u}_{0|t}^*$;
k_{max} is the number of control ;
for $t := 1$ *to* $k_{\max}$ **do** *Trajectory optimization*
    solve the optimal control problem:

$$\min_{\mathbf{x},\mathbf{u}} J_u(\mathbf{x}_{k|t}, \mathbf{u}_{k|t})$$

$$\text{s.t. } \mathbf{x}_{k+1|t} = \mathbf{f}(\mathbf{x}_{k|t}, \mathbf{u}_{k|t}), \ \mathbf{u}_{k|t} \in \mathbb{U}, \ \mathbf{x}_{0|t} = \hat{\mathbf{x}}_t$$

    exert the optimal control $\mathbf{u}_{0|t}^*$ to the robot;
end

5.2.4 Kinematic model considering slippage

The kinematic model (5.2.1) is only valid for the case without slippage between the crawler and ground. To reflect the effects of the slippage, the following kinematic model

with consideration of slipping ratio is adopted,

$$\mathbf{x}_{k+1} = \mathbf{x}_k + T_l \begin{bmatrix} \frac{v_{r,k}(1-a_{r,k})+v_{l,k}(1-a_{l,k})}{2}\cos\theta_k \\ \frac{v_{r,k}(1-a_{r,k})+v_{l,k}(1-a_{l,k})}{2}\sin\theta_k \\ \frac{v_{r,k}(1-a_{r,k})-v_{l,k}(1-a_{l,k})}{2d} \end{bmatrix} \tag{5.2.7}$$

$$a_{r,k} = \frac{v_{r,k} - v'_{r,k}}{v_{r,k}}, \; a_{l,k} = \frac{v_{l,k} - v'_{l,k}}{v_{l,k}}$$

where T_l is the control interval of lower layer NMPC, $v_{r,k}$ and $v_{l,k}$ are the theoretical velocities of left- and right-crawlers, $v'_{r,k}$ and $v'_{l,k}$ are the real velocities of left- and right-crawlers, $a_{r,k}$ and $a_{l,k}$ are the slippage ratios. The slippage ratios are assumed to satisfy the following relationship [68]

$$a_{r,k} = -\text{sgn}(v_{r,k} \cdot v_{l,k})\, a_{l,k} \tag{5.2.8}$$

where $\text{sgn}(\cdot)$ is the sign function. Detailed explanation for this relationship is presented as follows. When the left- and right-crawlers run in the same rotation direction, the slow side will be pulled by the fast side. Traction and braking forces are correspondingly generated on the fast and slow sides, which leads to the positive slippage of fast side and negative slippage of slow side. When the left- and right-crawlers run in the opposite rotation direction, both the slow and fast sides generate the traction forces to drive the rotation of tracked robot. Hence, both sides appear the positive slippage. Through measuring the angular velocity $\hat{\omega}_k$ of the tracked robot's body, the slippage ratios can be calculated

$$a_{r,k} = \frac{v_{r,k} - v_{l,k} - 2d\,\hat{\omega}_k}{v_{r,k} + v_{l,k}\,\text{sgn}(v_{r,k} \cdot v_{l,k})} \tag{5.2.9}$$

$$a_{l,k} = \frac{-v_{r,k} + v_{l,k} + 2d\,\hat{\omega}_k}{v_{l,k} + v_{r,k}\,\text{sgn}(v_{r,k} \cdot v_{l,k})} \tag{5.2.10}$$

The kinematic model (5.2.7) is reformulated as the following form with considering slippage disturbance

$$\mathbf{x}_{k+1} = \mathbf{x}_k + \mathbf{f}(\mathbf{x}_k, \mathbf{u}_k) + \mathbf{g}(\mathbf{x}_k) \tag{5.2.11}$$

$$\mathbf{f}(\mathbf{x}_k, \mathbf{u}_k) = T_l \begin{bmatrix} \cos\theta_k & 0 \\ \sin\theta_k & 0 \\ 0 & 1 \end{bmatrix} \mathbf{u}_k$$

$$\mathbf{g}(\mathbf{x}_k) = T_l \begin{bmatrix} \frac{-v_{r,k}\, a_{r,k} - v_{l,k}\, a_{l,k}}{2} \cos\theta_k \\ \frac{-v_{r,k}\, a_{r,k} - v_{l,k}\, a_{l,k}}{2} \sin\theta_k \\ \frac{-v_{r,k}\, a_{r,k} + v_{l,k}\, a_{l,k}}{2d} \end{bmatrix}$$

where $\mathbf{g}(x_k)$ is the disturbance from slippage. The disturbance $\mathbf{g}(\mathbf{x}_k)$ can be measured by sampling the IMU sensor and optical encoder data. If no slippage occurs or the slippage is very small, the absolute velocity approximately equals to the theoretical velocity (i.e., $a_{r,k} = a_{l,k} = 0$). Then kinematic model (5.2.11) will reduce to model (5.2.1).

Remark 5.2 *It is worth pointing out that the single layer NMPC in Algorithm 5.1 is performed at a relatively low frequency to wait for the renewal of reference input due to the speed limit of laser radar and processing latency of mapping. With such a low control frequency, it is almost impossible to measure the slippage disturbance and employ a dynamic compensation for improvement of the navigation performance. As shown in Fig.5.10, slippage ratios measured at 5 Hz sampling frequency obviously loses much information compared to the results at 50 Hz sampling frequency.*

A conventional way of increasing the control frequency is to adopt the lifting method shown in Fig.5.11, which is also referred to as the multirate sampling method [81]. T_u is the input sampling period for renewal of reference trajectory and desired control, T_l is the output sampling period for measurements of robot pose and slippage ratios. Assume that $T_u = l\, T_l$ holds, l is a integer number. The reference trajectory $\mathbf{x}_{d,k}$ and desired control $\mathbf{u}_{d,k}$ still update at the input sampling period T_u and remain invariant during the lifting period T_l. Through the lifting method, the control interval can be reduced to T_l.

Assume that the receding horizon length of original single layer NMPC is $N+1$ and the lifting frequency is l times of the original frequency. Then the length of receding horizon will become $l(N+1)$ after using the lifting method. The computational complexity of
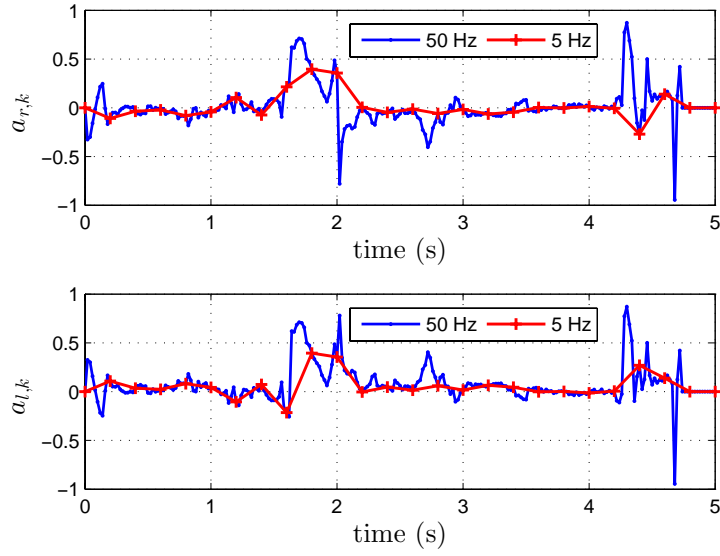
Fig. 5.10: Slippage ratios under different sampling frequency
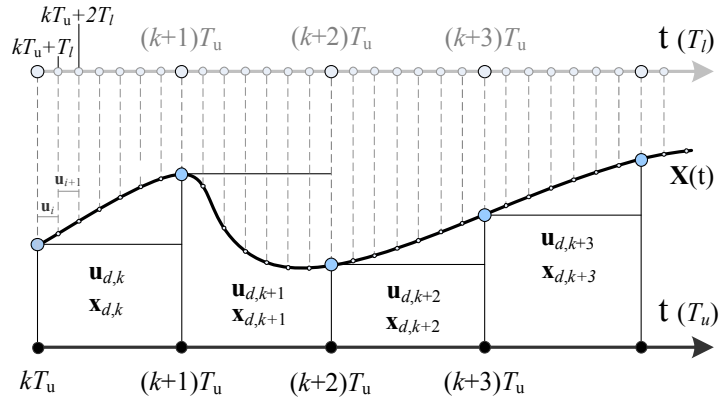
Fig. 5.11: Lifting method for increasing control frequency

the lifting method is determined by the lifting times l and horizon length $N+1$. For the case with long horizon $N+1$ and high lifting ratio l, the computational complexity of single layer NMPC introduced by the frequency lifting will increase to a very high and unacceptable level, which will affect the real-time performance for some platforms with limited computational resources.

5.2.5 Double-layer control

Actually, it is not necessary to perform the optimization of global trajectory tracking at each lifting period since the global trajectory tracking has slow process dynamic

compared to the local disturbance.

An alternative method to overcome the above trade-off between the computational complexity and local dynamic optimization performance is multi-layer model predictive control scheme. As shown in Fig. 5.12, a double layer NMPC architecture with slippage compensation is presented for the optimization of navigation performance. According to the different optimization objective, the optimization process is divided into two different time scales: the upper layer is performed at a low frequency ($\frac{1}{T_u}$) to optimize the global trajectory tracking performance, and the lower layer is conducted at a high frequency ($\frac{1}{T_l}$) to capture the local slippage.
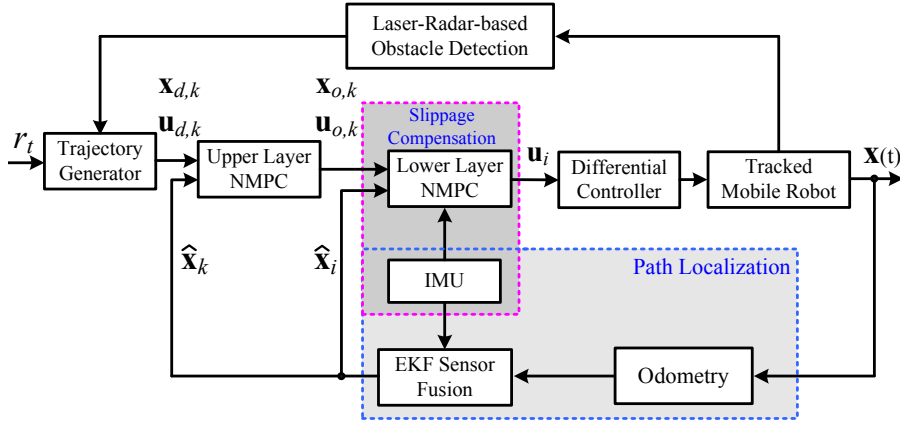
Fig. 5.12: Double layer NMPC with slippage compensation

As previous discussion about the double layer NMPC architecture, the global trajectory optimization based on the slow-scale model (5.2.1) is solved at the upper layer, and the slippage compensation based on the highly-dynamic model (5.2.11) is conducted at the lower layer to improve the local trajectory tracking performance. The upper layer NMPC cost function still utilize the cost function (5.2.4). Similar to the upper layer NMPC, the lower layer NMPC cost function is defined as

$$J_l(\mathbf{x}_{i|t}, \mathbf{u}_{i|t}) = \sum_{i=0}^{N_l-1} \left(||\mathbf{x}_{i|t} - \mathbf{x}_{o,k}||_{\mathbf{P}_1}^2 + ||\mathbf{u}_{i|t} - \mathbf{u}_{o,k}||_{\mathbf{P}_2}^2 \right)$$

$$+ ||\mathbf{x}_{N_l|t} - \mathbf{x}_{o,N_l}||_{\mathbf{P}_3}^2 \qquad (5.2.12)$$

where $\mathbf{x}_{o,k}$ is the local trajectory to be tracked by the lower layer NMPC, $\mathbf{u}_{o,k}$ is the

first control generated from the upper layer NMPC, and N_l is the horizon of the lower layer NMPC. Matrices $\mathbf{P}_1$, $\mathbf{P}_2$, and $\mathbf{P}_3$ refer respectively to the weighting matrices of the system state, control input, and terminal state of lower layer NMPC. The lower layer NMPC scheme based on the highly-dynamic model (5.2.11) will repeatedly solve the following optimal control problem:

$$\min_{\mathbf{x},\mathbf{u}} J_l(\mathbf{x}_{i|t}, \mathbf{u}_{i|t}) \tag{5.2.13}$$

$$\text{s.t. } \mathbf{x}_{i+1|t} = \mathbf{f}(\mathbf{x}_{i|t}, \mathbf{u}_{i|t}) + \mathbf{g}(\mathbf{x}_{i|t}), \ \mathbf{u}_{i|t} \in \mathbb{U}, \ \mathbf{x}_{0|t} = \mathbf{x}(t)$$

The double layer NMPC control scheme is summarized in Algorithm 5.2. A numerical case is simulated to evaluate the computational complexity. For the single layer NMPC with control frequency 5 Hz and horizon length 20, the horizon length will become 120 after lifting the control frequency to 30 Hz. The parameters of double layer NMPC are selected as: upper layer NMPC (control frequency 5 Hz, horizon length 20) and lower layer NMPC (control frequency 30 Hz, horizon length 20). The comparison of processing latency between the lifting-method-based single layer NMPC and double layer NMPC is illustrated in Fig.5.13. The processing latency mean values of lifting-method-based single layer NMPC and double layer NMPC are correspondingly 78.2921 ms and 6.1986 ms, which indicates that computation delay can be significantly reduced by using the double layer NMPC architecture. As for the trajectory tracking performance, some real experiments will be conducted to demonstrate it.

Remark 5.3 *The trajectory tracking based on the double layer NMPC architecture can be extended to other types of robots. The dynamic compensation of lower layer NMPC can be designed according to the specific characteristics of robots. For the robots with very high dynamic, the lower layer NMPC can be implemented on an embedded platform for the improvement of the real-time performance and the upper layer NMPC can be implemented on a computer with powerful computation resource for planning of complex tasks.*
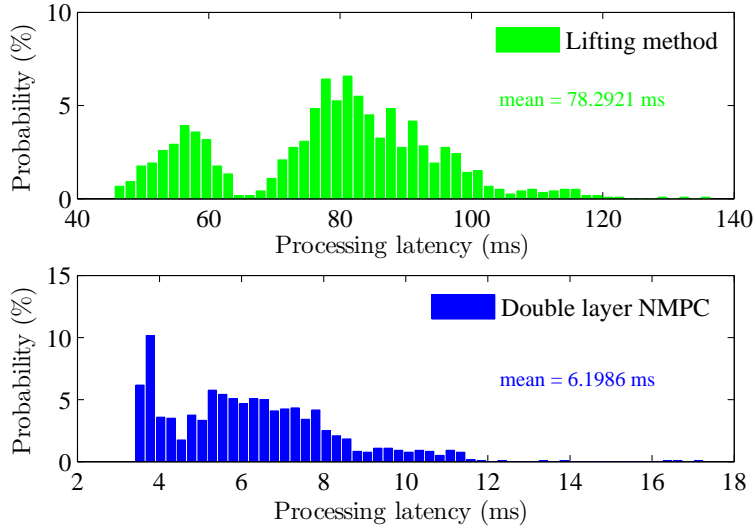
Fig. 5.13: Processing latency of lifting method and double layer NMPC

5.2.6 Feasibility, stability, and robustness analysis

The trajectory tracking error is denoted by $\mathbf{e}_k = \mathbf{x}_k - \mathbf{x}_{d,k}$. The closed-loop error system is represented as a time-varying system

$$\mathbf{e}(k+1) = \mathbf{f}(\mathbf{e}_k + \mathbf{x}_{d,k}, \mathbf{u}_k) - \mathbf{x}_{d,k+1} \qquad (5.2.14)$$
$$= \bar{\mathbf{f}}(\mathbf{e}_k, \mathbf{u}_k)$$

Achieving asymptotic stability of error dynamic system (5.2.14) can guarantee the reference tracking. Assume that there exists at least a feasible solution for the optimal problem (5.2.4), the optimal value function is defined as

$$V(t) = \min J_u(\mathbf{x}_{k|t}, \mathbf{u}_{k|t}) \qquad (5.2.15)$$

Obviously, $V(t)$ is bounded if there exists a feasible solution and $V(t)$ is continuous in the system state. $V(t) = 0$ holds for $\mathbf{e}_{k|t} = \mathbf{x}_{k|t} - \mathbf{x}_{d,k} = 0$, $\mathbf{u}_{k|t} = \mathbf{u}_{d,k} = 0$ and $V(t) > 0$ for arbitrary $\mathbf{e}_{k|t} \neq 0$. Denote the optimal control sequence as

$$\mathbf{u}^*_{\cdot|t} = \left[\mathbf{u}^*_{0|t}, \ \mathbf{u}^*_{1|t}, \ \ldots, \ \mathbf{u}^*_{N-1|t} \right] \qquad (5.2.16)$$

Algorithm 5.2: Double Layer NMPC

---

initialize upper layer NMPC ;
input data: $\mathbf{x}_{d,k}, \mathbf{u}_{d,k}$ and $\hat{\mathbf{x}}_k$;
output result: $\mathbf{x}_{o,k}$ and $\mathbf{u}_{o,k}$;
$k_{\max}$ is the number of upper layer control ;
$i_{\max}$ is the number of lower layer control during T_u;
for $t_u := 1$ *to* $k_{\max}$ **do** *Global trajectory optimization*
$\quad$ solve the upper-layer optimal control problem:

$$\min_{\mathbf{x},\mathbf{u}} J_u(\mathbf{x}_{k|t_u}, \mathbf{u}_{k|t_u})$$

$$\text{s.t. } \mathbf{x}_{k+1|t_u} = \mathbf{f}(\mathbf{x}_{k|t_u}, \mathbf{u}_{k|t_u}), \mathbf{u}_{k|t_u} \in \mathbb{U}, \mathbf{x}_{0|t_u} = \hat{\mathbf{x}}_{t_u}$$

$\quad$ update tracking trajectory $\mathbf{x}_{o,t_u}$ and control $\mathbf{u}_{o,t_u}$;
$\quad$ initialize lower layer NMPC ;
$\quad$ input data: $\mathbf{x}_{o,t_u}, \mathbf{u}_{o,t_u}$ and $\hat{\mathbf{x}}_i$;
$\quad$ output result: optimal control $\mathbf{u}^*_{0|t_l}$;
$\quad$ **for** $t_l := 1$ *to* $i_{\max}$ **do** *Local trajectory optimization*
$\quad\quad$ estimate the slippage disturbance $\mathbf{g}(\mathbf{x}_{t_l})$;
$\quad\quad$ solve the lower-layer optimal control problem:

$$\min_{\mathbf{x},\mathbf{u}} J_l(\mathbf{x}_{i|t_l}, \mathbf{u}_{i|t_l})$$

$$\text{s.t. } \mathbf{x}_{i+1|t_l} = \mathbf{f}(\mathbf{x}_{i|t_l}, \mathbf{u}_{i|t_l}) + \mathbf{g}(\mathbf{x}_{i|t_l}), \mathbf{u}_{i|t_l} \in \mathbb{U}, \mathbf{x}_{0|t_l} = \hat{\mathbf{x}}_{t_l}$$

$\quad\quad$ exert the optimal control $\mathbf{u}^*_{0|t_l}$ to the robot;
$\quad$ **end**
$\quad$ reset $t_l = 1$, prepare the next optimization loop;
end

---

which satisfies the constraints in (5.2.5), and the corresponding optimal error state sequence is represented as

$$\mathbf{e}^*_{\cdot|t} = \left[\mathbf{e}^*_{0|t}, \ \mathbf{e}^*_{1|t}, \ \ldots, \ \mathbf{e}^*_{N|t} \right], \mathbf{e}^*_{k|t} = \mathbf{x}^*_{k|t} - \mathbf{x}_{d,k} \tag{5.2.17}$$

The optimal input sequence has minimized the cost function $J_u(\mathbf{x}_{k|t}, \mathbf{u}_{k|t})$ such that

$$V(t) = \sum_{k=0}^{N-1} \left(||\mathbf{e}^*_{k|t}||^2_{\mathbf{Q}_1} + ||\Delta\mathbf{u}^*_{k|t}||^2_{\mathbf{Q}_2} \right) + ||\mathbf{e}^*_{N|t}||^2_{\mathbf{Q}_3} \tag{5.2.18}$$

where $\Delta\mathbf{u}^*_{k|t} = \mathbf{u}^*_{k|t} - \mathbf{u}_{d,k}$. For a sufficiently large prediction horizon N, the following relationships $\mathbf{e}_{k|t+1} = \mathbf{e}^*_{k+1|t}$, $\Delta\mathbf{u}_{k|t+1} = \Delta\mathbf{u}^*_{k+1|t}$, $k \in [1, N]$ would hold according to that

the optimal solution $^*_{k+1|t}$ is also a feasible solution [79]. For convenient analysis, the weighting matrix $\mathbf{Q}_3$ is chosen equal to $\mathbf{Q}_1$. Consequently, it is obtained that

$$
\begin{aligned}
J_u&(\mathbf{x}_{k|t+1}, \mathbf{u}_{k|t+1}) \\
&= \sum_{k=0}^{N-1} \left(||\mathbf{e}_{k|t+1}||^2_{\mathbf{Q}_1} + ||\Delta\mathbf{u}_{k|t+1}||^2_{\mathbf{Q}_2} \right) + ||\mathbf{e}_{N|t+1}||^2_{\mathbf{Q}_3} \\
&= V(t) - ||\mathbf{e}^*_{0|t}||^2_{\mathbf{Q}_1} - ||\Delta\mathbf{u}^*_{0|t}||^2_{\mathbf{Q}_2}
\end{aligned}
\tag{5.2.19}
$$

Then, it follows from (5.2.15) and (5.2.19) that

$$
V(t+1) \leq J_u(\mathbf{x}_{k|t+1}, \mathbf{u}_{k|t+1}) \leq V(t) - ||\mathbf{e}^*_{0|t}||^2_{\mathbf{Q}_1}
\tag{5.2.20}
$$

Recursive feasibility requires that the optimal problem has a feasible solution at time instant $t = 0$. Since the reference tracking control in this paper is based on the open-loop trajectory planning, a feasible solution at time instant $t = 0$ always exists in a neighborhood of reference trajectory and desired control. Thus, the recursive feasibility can be guaranteed. From (5.2.20), it can be derived that

$$
V(t+1) - V(t) \leq -\lambda_{\min}(\mathbf{Q}_1)||\mathbf{e}^*_{0|t}||^2
\tag{5.2.21}
$$

$\lambda_{\min}(\mathbf{Q}_1)$ is the minimum eigenvalue. Inequality (5.2.21) demonstrates that the optimal value function $V(t)$ will converge along the reference trajectory. Thus, the stability of error dynamic system can be guaranteed.

The stability analysis of the lower layer control is similar to above analysis of the upper layer control when the slippage disturbance is ignored, and which is not repeated here. Additionally, the lower layer control with slippage compensation can be exploited to improve the prediction accuracy, which can effectively enhance the robustness and controller performances.

5.3 Experimental results

In this section, the vibration isolation and autonomous navigation performance of this tracked mobile robot will be tested in indoor environment. The schematic diagram of navigation is shown in Fig.5.14. The robot will cross the small obstacle placed on the ground and simultaneously avoid the obstacle from the starting point to the target point. For the convenient of experimental testing, the model predictive controllers mentioned in the previous section are implemented on a laptop with an Intel 1.6 Ghz Core i5 processor and 8GB RAM. The communication between the laptop and control board including the sensor data acquisition and control command transmission is through wireless network.
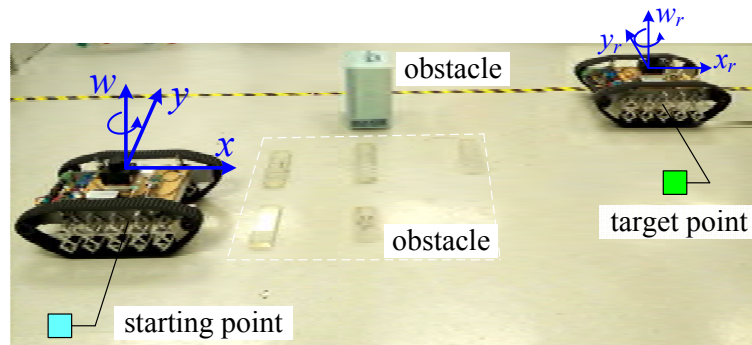
Fig. 5.14: Schematic diagram of navigation task

5.3.1 Assessment of obstacle negotiation performance

The snapshot sequence of negotiating obstacle with height 40 mm is shown in Fig.5.15, where Fig.5.15 (a-i) and (j-o) correspondingly illustrate the motions of climbing up and down the obstacle. The isolation performance is evaluated by measuring the vertical acceleration. The vertical acceleration response of the robot body is shown in Fig.5.16. It can be clearly observed that the tracked mobile robot with the bio-inspired suspension has much smaller shock amplitude compared with the case without enabling the bio-inspired suspension. This result demonstrates that the novel passive suspension can efficiently absorb the strong shock induced by the process of obstacle crossing and hence guarantee the smooth motion of the robot.
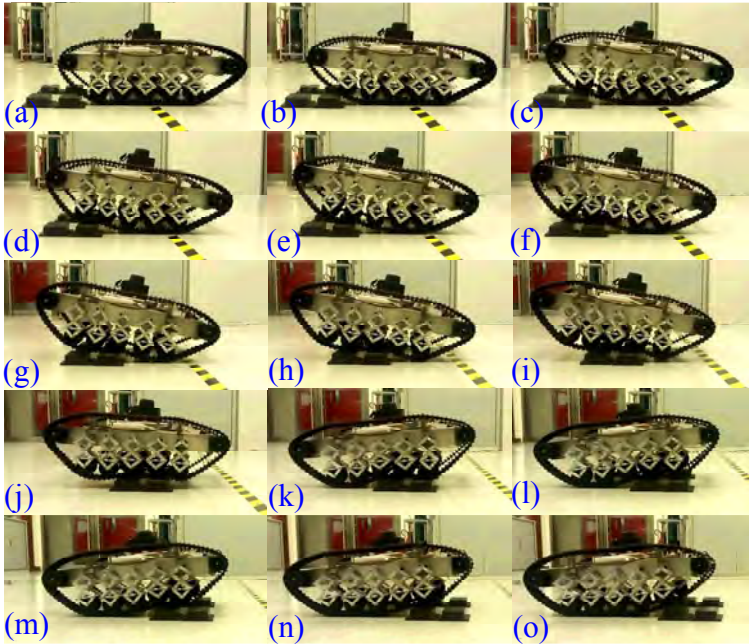
Fig. 5.15: Snapshot sequence of negotiating obstacle
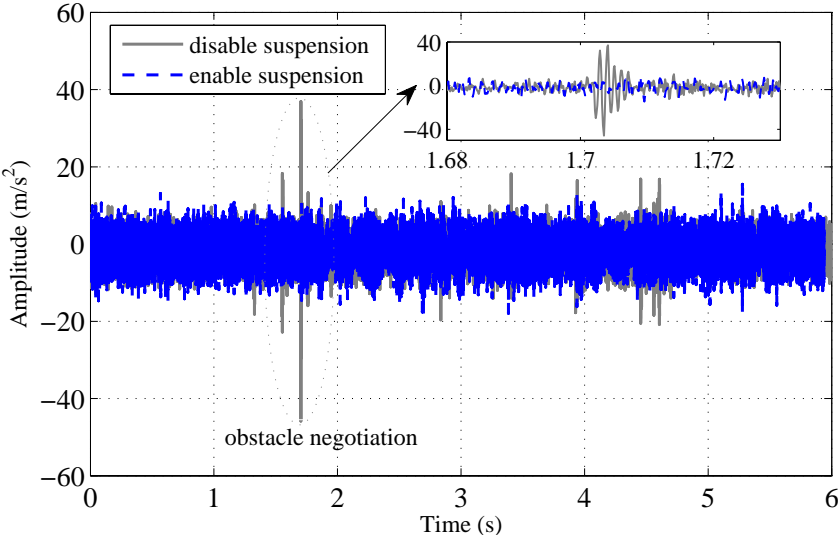
Fig. 5.16: Acceleration response under different cases
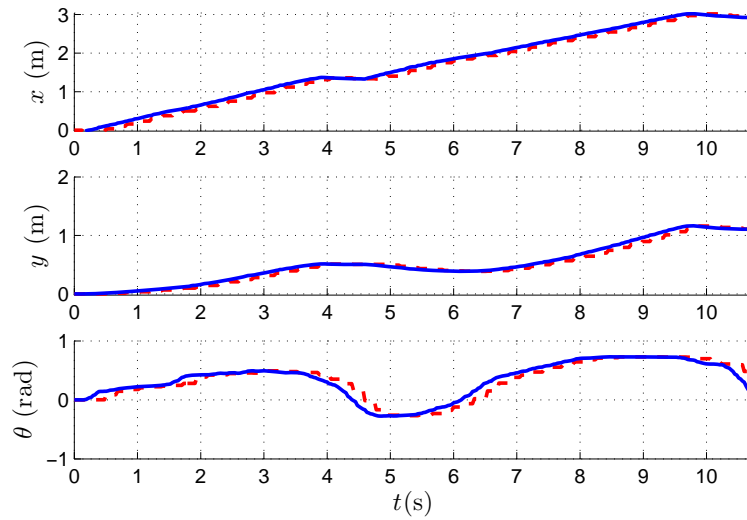
Fig. 5.17: State response: reference (solid line) and measurement (dash line) using single layer NMPC
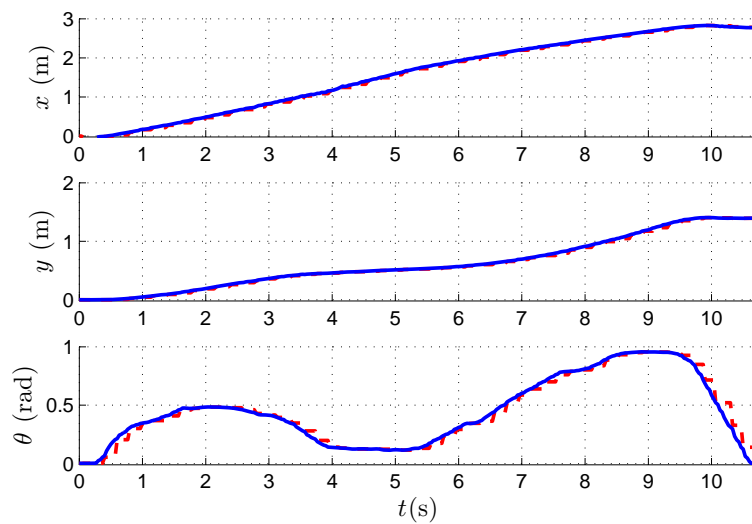
Fig. 5.18: State response: reference (solid line) and measurement (dash line) using double layer NMPC
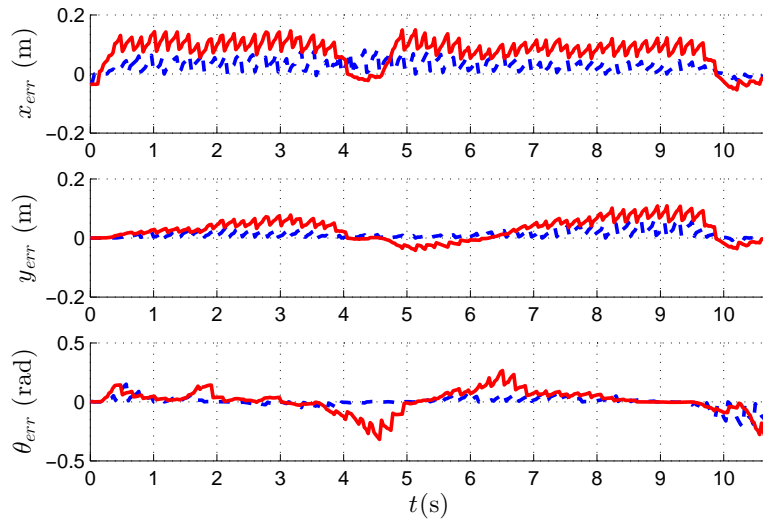
Fig. 5.19: Trajectory tracking error: single layer NMPC (solid line) and double layer NMPC (dash line).
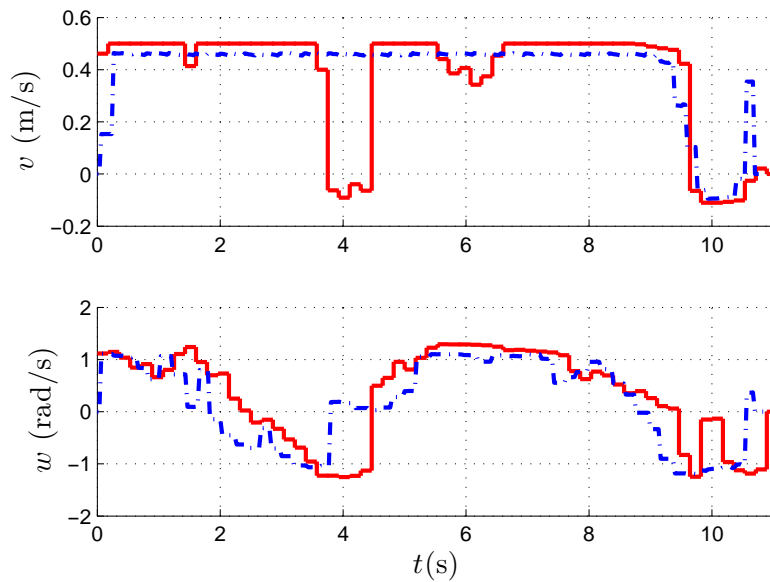
Fig. 5.20: Controller output: single layer NMPC (solid line) and double layer NMPC (dash line).
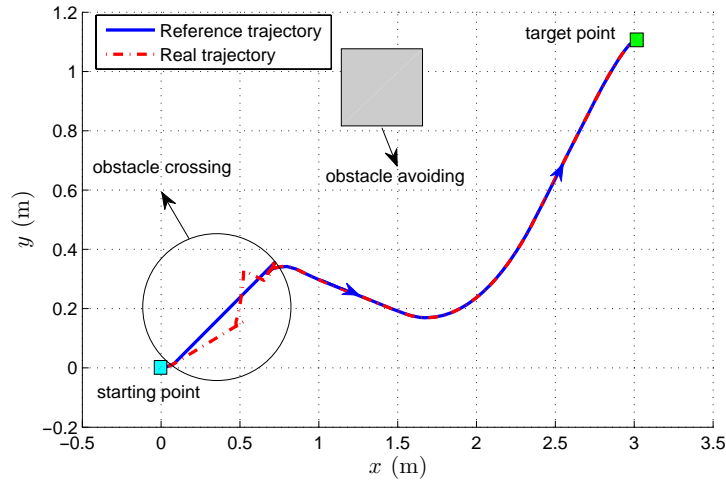
Fig. 5.21: Trajectory tracking results using double layer NMPC: reference (solid line) and measurement (dash line).

5.3.2 Trajectory tracking results using different algorithms

For the single layer NMPC, the reference trajectory and control signal are generated at approximate 5 Hz and the horizon length is 10. The parameters of double layer NMPC are selected as: upper layer NMPC (control frequency 5 Hz, horizon length 10) and lower layer NMPC (control frequency 30 Hz, horizon length 15). The navigation performance is adjusted through the weighting matrices. The linear and angular velocities are correspondingly limited to $-0.4\,\mathrm{m/s} \leq v \leq 0.5\,\mathrm{m/s}$ and $-1.3\,\mathrm{rad/s} \leq \omega \leq 1.3\,\mathrm{rad/s}$. The state responses under the single layer and double layer NMPC are shown in Fig.5.17 and Fig.5.18 correspondingly. The robot can follow the reference trajectory and finally reach the target position. The resulting trajectory tracking error is depicted in Fig.5.19. The detailed peak-to-peak (PtoP) and root-mean-square (RMS) values of trajectory tracking error defined in (5.3.1) and (5.3.2) are listed in Table 5.1, which also demonstrates that the double layer NMPC strategy holds a significant PtoP error reduction (around 38%-51%) and also RMS error reduction (around 51%-62%). These results verify that the double layer NMPC can effectively improve the trajectory tracking accuracy.

$$\mathrm{PtoP}\{x_{\mathrm{err}}\} = \max\{x_{\mathrm{err}}\} - \min\{x_{\mathrm{err}}\} \qquad (5.3.1)$$

$$\mathrm{RMS}\{x_{\mathrm{err}}\} = \sqrt{\frac{1}{N_e}\sum\nolimits_{i=1}^{N_e}\|x_{\mathrm{err}}(t_i)\|^2} \qquad (5.3.2)$$
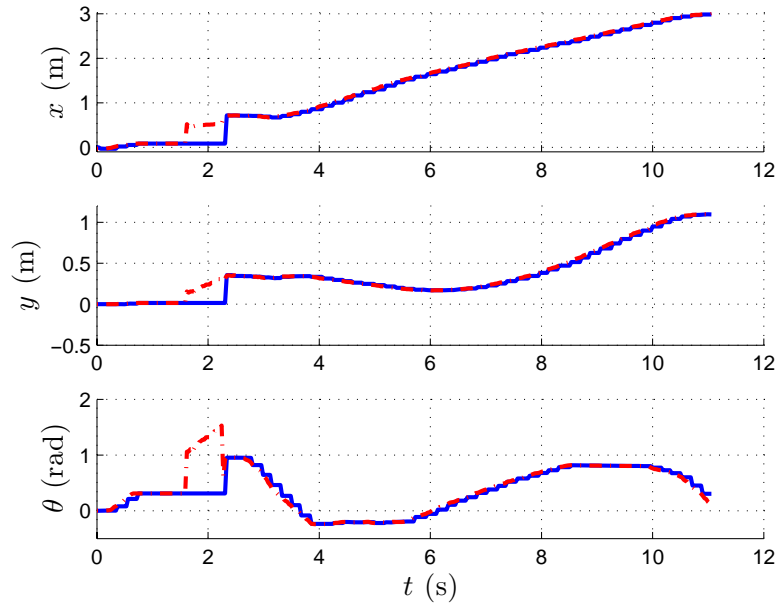
(a) State response
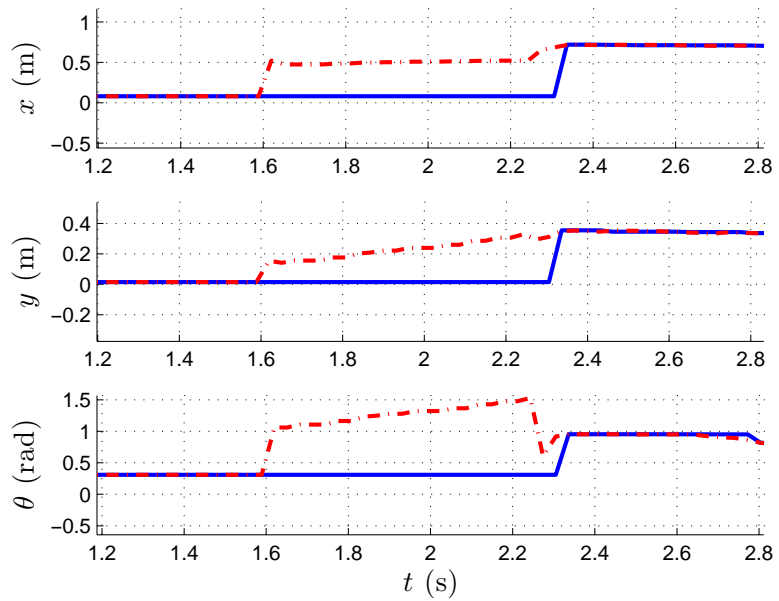
(b) Transient tracking process

Fig. 5.22: State response of double layer NMPC: reference (solid line) and measurement (dash line).

Table 5.1: PtoP and RMS values of trajectory tracking error

	Single layer NMPC	Double layer NMPC
PtoP$\{x_{\text{err}}\}$ (m)	0.1845	0.1144 ($\downarrow$ 37.99%)
PtoP$\{y_{\text{err}}\}$ (m)	0.1512	0.0730 ($\downarrow$ 51.72%)
PtoP$\{\theta_{\text{err}}\}$ (rad)	0.5843	0.3578 ($\downarrow$ 38.76%)
RMS$\{x_{\text{err}}\}$ (m)	0.0919	0.0346 ($\downarrow$ 62.35%)
RMS$\{y_{\text{err}}\}$ (m)	0.0463	0.0190 ($\downarrow$ 58.96%)
RMS$\{\theta_{\text{err}}\}$ (rad)	0.0906	0.0436 ($\downarrow$ 51.88%)

The controller output is shown in Fig.5.20. In this case, when the robot negotiates the obstacle, the sudden change of robot pose does not appear. And the dynamic compensation of lower layer NMPC still plays an important role in the local trajectory optimization.
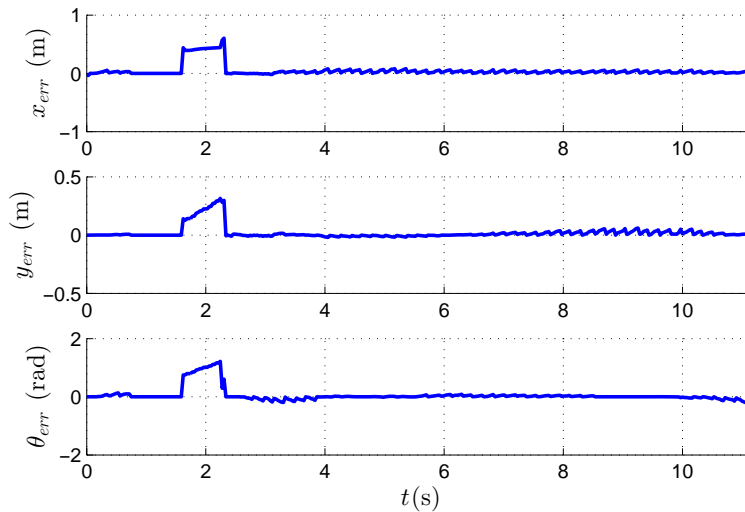
Fig. 5.23: Trajectory tracking error using double layer NMPC

To further illustrate the effectiveness of the double layer NMPC scheme for the trajectory tracking optimization, a case with external disturbance induced by the sudden change of robot pose is considered. This case has the same navigation task as shown in Fig.5.14. The trajectory tracking result under the double layer NMPC scheme is depicted in Fig.5.21. Different from the previous experiment, this experiment appears trajectory deviation. During the process of obstacle crossing, the robot pose suddenly changes and meanwhile the motion direction is constrained to an uncontrolled state, thus
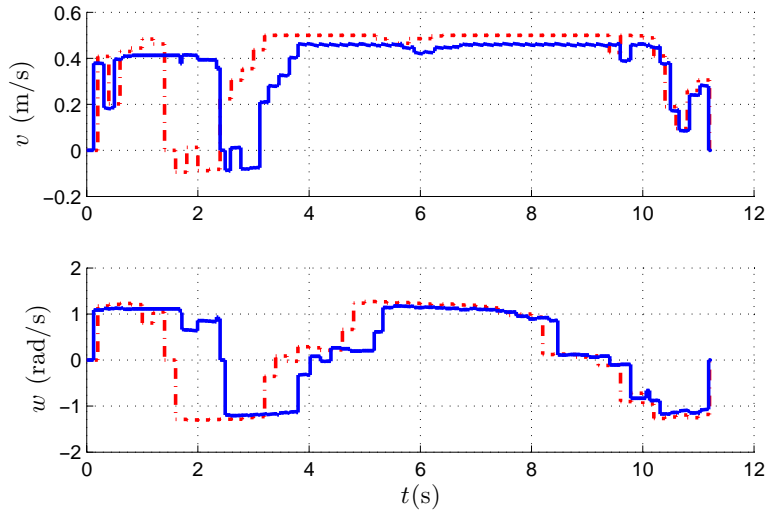
Fig. 5.24: Controller output of double layer NMPC: upper layer $\mathbf{u}_{o,k}$ (dash line) and lower layer $\mathbf{u}_i$ (solid line).

the robot moves away from the reference trajectory. The state response and transient tracking process at $t \in [1.2\ 2.8]$ s under the double layer NMPC are shown in Fig.5.22. The obstacle crossing starts at about $t = 1.6$ s and ends at about $t = 2.2$ s. Once the process is completed, the robot moves back to the reference trajectory quickly. During $t \in [2.2\ 2.4]$ s, the robot adjusts the motion direction toward the reference trajectory using a higher frequency than the control frequency(5 Hz) of the upper layer NMPC, which means that lower layer NMPC makes important contributions to improve the transient tracking process. The resulting trajectory tracking error and controller output are correspondingly shown in Fig.5.23 and 5.24.

5.4 Concluding remarks

In this chapter, the autonomous navigation control of a tracked mobile robot with a novel passive suspension system using bio-inspired animal-limb-like structure has been discussed. The superiority of tracked mobile robot lies in the following points: (1) This bio-inspired structure can provide an excellent quasi-zero-stiffness characteristic with high static stiffness, low dynamic stiffness and broad frequency range of vibration isolation. For the tracked mobile robot with the novel bio-inspired suspension, both high

loading capacity and excellent vibration isolation performance can be simultaneously guaranteed. (2) The tracked robot with the bio-inspired suspension is easy to implement and maintain and does not require high precision at manufacturing. (3) The robust navigation adopting a double layer NMPC strategy is capable of tracking the global reference trajectory also with the ability to perform local performance optimization in occurrence of uncertain slippage disturbances with less computational burden.

6 Vision-based robust human following control for a tracked mobile robot

This chapter will investigate the vision based robust human-following controller for the tracked mobile robot. Since human's motion is often completely unpredictable, traditional human-following method using PID controllers cannot simultaneously guarantee the smoothness and rapidity of human-following [86]. Increasing the gain of PID controller can effectively improve the robot's transient response but also has the possibility of causing local oscillation. The main problem of PID controller with a low gain lies in the fact that human's lateral movement may make the target out of the robot camera's FOV leading to following failure. A robust nonlinear controller with disturbance compensation is proposed for reliable and smooth human following. The human skeleton image is measured by using a RGB-D camera. Different from existing methods, the disturbance compensation on human's motion is implemented by combining the depth skeleton tracking and human motion estimation. In addition, human-robot interaction is realized through the hand gesture recognition. The laser radar sensor is used for collision avoidance during human-robot following.

The chapter is organized as follows. Section 6.1 starts with the problem formulation and preliminaries of vision based human-following control. In Section 6.2, a vision-based robust controller with disturbance compensation is designed. The disturbance induced by human motion is estimated through using the depth skeleton image measured by RGB-D camera. Some experimental results are presented in Section 6.3 to demonstrate the effectiveness and applicability of the robust human-following controller on the tracked mobile robot. Finally, Section 6.4 concludes the chapter.

114

6.1 Problem formulation and preliminaries

The tracked mobile robot mounting a RGB-D camera for human following is shown in Fig.6.1. Fig.6.2 depicts the human position and orientation with respect to the robot, where α is the human orientation angle measured between the robot principle axis and the distance vector e, s is the human motion vector and θ is the human moving angle measured between the distance vector e and human motion vector s. v and w are respectively the linear and angular velocities. For the vision based human-robot following control, the goal is to make the robot follow the human along the direction of distance vector e. Under this control strategy, the target human can always be kept within the FOV of robot camera. In order to keep target within the center of robot camera's FOV and avoid following failure, the tracking controller should have a quick response capability.
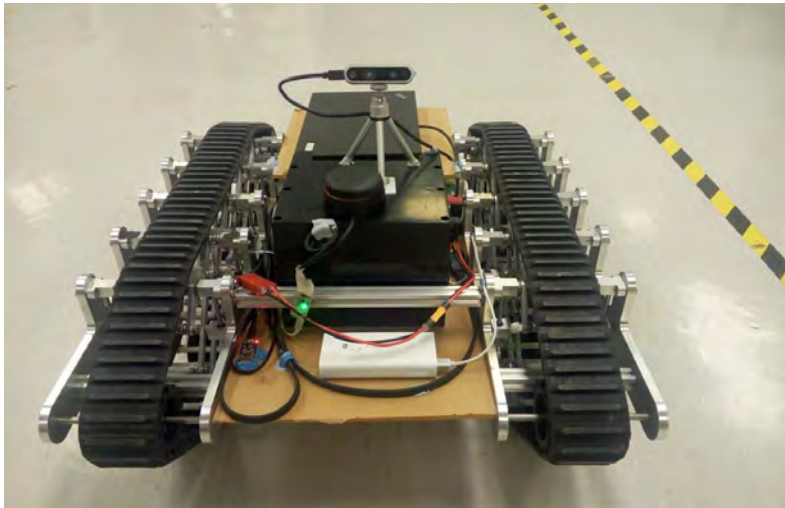
Fig. 6.1: Tracked mobile robot mounting a RGB-D camera

A simple and traditional method to achieve this human-robot following control is to use PID controllers to separately adjust the linear and angular velocities [86].

$$v(t) = k_{p1}\, e(t) + k_{i1} \int_0^t e(\tau)d\tau + k_{d1}\frac{d\, e(t)}{dt} \tag{6.1.1}$$

$$w(t) = k_{p2}\, \alpha(t) + k_{i2} \int_0^t \alpha(\tau)d\tau + k_{d2}\frac{d\, \alpha(t)}{dt} \tag{6.1.2}$$
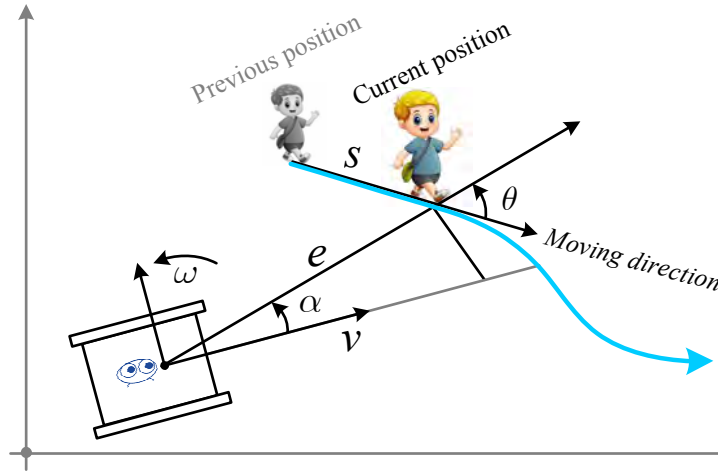
Fig. 6.2: Human's position and orientation with respect to the robot

where k_{p1}, k_{i1} and k_{d1} are the parameters of linear velocity controller, k_{p2}, k_{i2} and k_{d2} are the parameters of angular velocity controller.

Remark 6.1 *The PID controllers in (6.1.1) and (6.1.2) are easy to be implemented. Even though the parameters k_{p1}, k_{i1}, k_{d1} and k_{p2}, k_{i2}, k_{d2} can be well turned through multiple experiments, the PID controllers still have the problems of low robust stability and poor following performance when the systems encounter the perturbations, like the disturbance from human motion, skeleton tracking accuracy. Another aspect is that the linear and angular velocities are separately controlled. It is difficult to simultaneously guarantee the smoothness and rapidity of human-robot following control. Furthermore, improving the transient response may lead to local oscillation.*

6.2 Robust controller design with disturbance compensation

In view of the above observations, a robust following controller with disturbance compensation will be designed. Without considering the human's motion, the kinematic equation of human following control modified from [128] is described in a polar coordi-

nate,

$$
\begin{cases}
\dot{e}(t) = -v(t)\cos(\alpha(t)) \\
\dot{\alpha}(t) = -w(t) + v(t)\dfrac{\sin(\alpha(t))}{e(t)}
\end{cases}
\tag{6.2.1}
$$

For vision based human following control, the robot camera's FOV is very limited. To improve the robot's following capability, it is necessary to consider the human's motion during controller design. By considering the human motion in kinematic equation (6.2.1), the kinematic equation can be rewritten as

$$
\begin{cases}
\dot{e}(t) = -v(t)\cos(\alpha(t)) + \dot{s}(t)\cos(\theta(t)) \\
\dot{\alpha}(t) = -w(t) + v(t)\dfrac{\sin(\alpha(t))}{e(t)} - \dot{s}(t)\dfrac{\sin(\theta(t))}{e(t)}
\end{cases}
\tag{6.2.2}
$$

The human's position and orientation with respect to robot is depicted in Fig.6.2. From (6.2.2), it is obvious that the human following control performance is additionally affected by the absolute velocity $\dot{s}(t)$ and motion direction $\theta(t)$ apart from the control input $v(t)$ and $w(t)$.

The human's motion can be regarded as a uncertain disturbance of kinematic system (6.2.2). Design a robust nonlinear human-robot following controller with disturbance compensation as the following form

$$
\begin{cases}
v(t) = \gamma\cos(\alpha)e(t) + \Delta v(t) \\
w(t) = k\alpha(t) + \gamma\cos(\alpha(t))\sin(\alpha(t)) + \Delta w(t)
\end{cases}
\tag{6.2.3}
$$

where γ and k are positive constant, $\Delta v(t)$ and $\Delta w(t)$ are correspondingly the disturbance compensations of linear velocity $v(t)$ and angular velocity $w(t)$. The disturbance compensation is on-line calculated according the following relationship

$$
\begin{cases}
\Delta v(t) = \dfrac{\dot{s}(t)\cos(\theta(t))}{\cos(\alpha(t))} \\
\Delta w(t) = (\dot{s}(t)\cos(\theta(t))\tan(\alpha(t)) - \dot{s}(t)\sin(\theta(t)))\dfrac{1}{e(t)}
\end{cases}
\tag{6.2.4}
$$

The stability of this nonlinear following controller with disturbance compensation is demonstrated as follows. By substituting the controller (6.2.3) into kinematic equation

(6.2.2), the closed-loop system of human-robot following control is obtained

$$\begin{cases} \dot{e}(t) = -\gamma \cos^2(\alpha(t))e(t) \\ \dot{\alpha}(t) = -k\alpha(t) \end{cases} \tag{6.2.5}$$

where nonlinear term $\cos^2(\alpha(t))$ is a state-dependent uncertainty. For convenient analysis of the system stability, the closed-loop system is rewritten as the form of state-dependent polytopic system (2.1.5).

$$\begin{bmatrix} \dot{e}(t) \\ \dot{\alpha}(t) \end{bmatrix} = \sum_{i=1}^{2} \sigma_i(t) A_i \begin{bmatrix} e(t) \\ \alpha(t) \end{bmatrix} \tag{6.2.6}$$

where $\sigma_1(t) = \cos^2(\alpha(t))$, $\sigma_2(t) = 1 - \cos^2(\alpha(t))$ and

$$A_1 = \begin{bmatrix} -\gamma & 0 \\ 0 & -k \end{bmatrix}, A_2 = \begin{bmatrix} 0 & 0 \\ 0 & -k \end{bmatrix}$$

By resorting to Lyapunov stability criterion (2.2.1), it is easy to conclude that for any parameters $\gamma > 0$ and $k > 0$, the closed-loop system is asymmetrically stable. A brief analysis is presented as follows. A Lyapunov function in the following form is constructed to analyze the stability of closed-loop system (6.2.6)

$$V(t) = \begin{bmatrix} e(t) \\ \alpha(t) \end{bmatrix}^T P \begin{bmatrix} e(t) \\ \alpha(t) \end{bmatrix} \tag{6.2.7}$$

where P is a symmetric positive definite matrix. The time derivative of $V(t)$ is obtained as

$$\dot{V}(t) = \begin{bmatrix} e(t) \\ \alpha(t) \end{bmatrix}^T \sum_{i=1}^{2} \sigma_i(t) \left(PA_i + A_i^T P \right) \begin{bmatrix} e(t) \\ \alpha(t) \end{bmatrix} \tag{6.2.8}$$

For convenient analysis, matrix P is chosen as the identity matrix. Then, it follows from

(6.2.6) and (6.2.8) that

$$\dot{V}(t) + \lambda V(t) = \begin{bmatrix} e(t) \\ \alpha(t) \end{bmatrix}^T \sum_{i=1}^{2} \sigma_i(t) \left(2A_i + \lambda I\right) \begin{bmatrix} e(t) \\ \alpha(t) \end{bmatrix} \qquad (6.2.9)$$

Furthermore, for any positive scalar λ satisfying $\lambda \leq \min\{2\gamma, 2k\}$, the following relationship holds due to the fact that $2A_i + \lambda I$, $i = \{1, 2\}$, is negative definite.

$$\dot{V}(t) < -\lambda V(t) < 0 \qquad (6.2.10)$$

Therefore, it can be concluded that the system (6.2.2) can be globally exponentially stabilized by the human-robot following controller (6.2.3) with a decay rate $\lambda = \min\{2\gamma, 2k\}$.
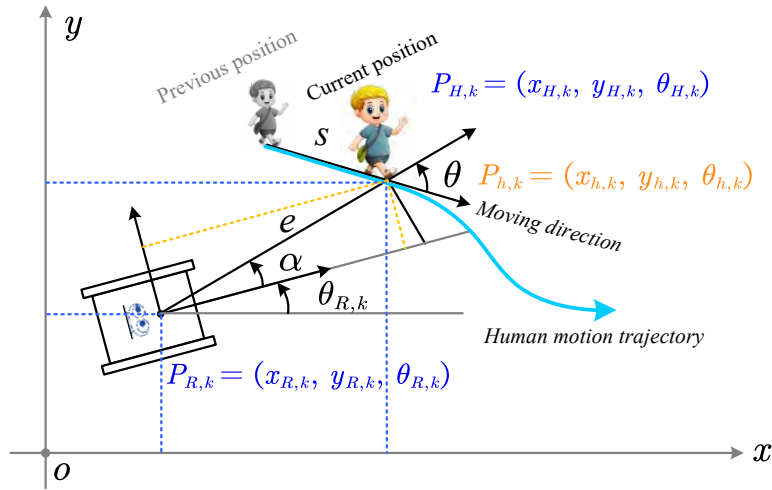
Fig. 6.3: Posture definitions for estimation of human motion

To implement the nonlinear controller with disturbance compensation, the human motion absolute velocity and moving direction need to be estimated. As shown in Fig.6.3, the human's position at previous sampling instant is recorded and transformed into the current robot's local coordinate. At sampling time instant k, human's local posture with respect to robot's position is define as $P_{h,k} = (x_{h,k}, y_{h,k}, \theta_{h,k})$. Human's global posture is define as $P_{H,k} = (x_{H,k}, y_{H,k}, \theta_{H,k})$. Robot's global posture is define as $P_{R,k} = (x_{R,k}, y_{R,k}, \theta_{R,k})$. The human's global posture can be calculated by

$$P_{H,k} = \begin{bmatrix} \cos(\theta_{R,k}) & -\sin(\theta_{R,k}) & 0 \\ \sin(\theta_{R,k}) & \cos(\theta_{R,k}) & 0 \\ 0 & 0 & 1 \end{bmatrix} P_{h,k} + P_{R,k} \qquad (6.2.11)$$

The human's local posture at sampling time instant k with respect to the robot's position at sampling time instant $k+1$ is represented as

$$\tilde{P}_{h,k} = \begin{bmatrix} \cos(\theta_{R,k+1}) & \sin(\theta_{R,k+1}) & 0 \\ -\sin(\theta_{R,k+1}) & \cos(\theta_{R,k+1}) & 0 \\ 0 & 0 & 1 \end{bmatrix} (P_{H,k} - P_{R,k+1}) \qquad (6.2.12)$$

By substituting the human's global posture (6.2.11) into (6.2.12), it is obtained

$$\tilde{P}_{h,k} = \begin{bmatrix} \cos(\theta_{R,k+1}) & \sin(\theta_{R,k+1}) & 0 \\ -\sin(\theta_{R,k+1}) & \cos(\theta_{R,k+1}) & 0 \\ 0 & 0 & 1 \end{bmatrix} \times$$

$$\left\{ \begin{bmatrix} \cos(\theta_{R,k}) & -\sin(\theta_{R,k}) & 0 \\ \sin(\theta_{R,k}) & \cos(\theta_{R,k}) & 0 \\ 0 & 0 & 1 \end{bmatrix} P_{h,k} + P_{R,k} - P_{R,k+1} \right\} \qquad (6.2.13)$$

For small angle variation, i.e., $\theta_{R,k} \approx \theta_{R,k+1}$, the following approximation holds

$$\begin{bmatrix} \cos(\theta_{R,k+1}) & \sin(\theta_{R,k+1}) & 0 \\ -\sin(\theta_{R,k+1}) & \cos(\theta_{R,k+1}) & 0 \\ 0 & 0 & 1 \end{bmatrix} \begin{bmatrix} \cos(\theta_{R,k}) & -\sin(\theta_{R,k}) & 0 \\ \sin(\theta_{R,k}) & \cos(\theta_{R,k}) & 0 \\ 0 & 0 & 1 \end{bmatrix} \approx I \qquad (6.2.14)$$

To reduce the computational complexity, the posture $\tilde{P}_{h,k}$ can be approximately obtained as

$$\tilde{P}_{h,k} = P_{h,k} + \begin{bmatrix} \cos(\theta_{R,k+1}) & \sin(\theta_{R,k+1}) & 0 \\ -\sin(\theta_{R,k+1}) & \cos(\theta_{R,k+1}) & 0 \\ 0 & 0 & 1 \end{bmatrix} (P_{R,k} - P_{R,k+1}) \qquad (6.2.15)$$

Through (6.2.15), the previous human's posture has been transformed into current local coordinate. Define human motion error posture $P_{e,k+1} = P_{h,k+1} - \tilde{P}_{h,k} = (x_{e,k+1}, y_{e,k+1}, \theta_{e,k+1})$,

$$P_{e,k+1} = (P_{h,k+1} - P_{h,k}) + \begin{bmatrix} \cos(\theta_{R,k+1}) & \sin(\theta_{R,k+1}) & 0 \\ -\sin(\theta_{R,k+1}) & \cos(\theta_{R,k+1}) & 0 \\ 0 & 0 & 1 \end{bmatrix} (P_{R,k+1} - P_{R,k}) \quad (6.2.16)$$

A more accurate estimation of human motion error posture $P_{e,k+1}$ is presented from (6.2.13)

$$P_{e,k+1} = P_{h,k+1} + \begin{bmatrix} \cos(\theta_{R,k+1}) & \sin(\theta_{R,k+1}) & 0 \\ -\sin(\theta_{R,k+1}) & \cos(\theta_{R,k+1}) & 0 \\ 0 & 0 & 1 \end{bmatrix} (P_{R,k+1} - P_{R,k}) - \\ \begin{bmatrix} \cos(\theta_{R,k+1} - \theta_{R,k}) & \sin(\theta_{R,k+1} - \theta_{R,k}) & 0 \\ -\sin(\theta_{R,k+1} - \theta_{R,k}) & \cos(\theta_{R,k+1} - \theta_{R,k}) & 0 \\ 0 & 0 & 1 \end{bmatrix} P_{h,k} \quad (6.2.17)$$

The absolute velocity $\dot{s}(t_{k+1})$, $\cos(\theta(t_{k+1}))$, and $\sin(\theta(t_{k+1}))$ are calculated by

$$\dot{s}(t_{k+1}) = \frac{\sqrt{x_{e,k+1}^2 + y_{e,k+1}^2}}{\Delta t} \quad (6.2.18)$$

$$\cos(\theta(t_{k+1})) = \frac{x_{e,k+1} x_{h,k+1} + y_{e,k+1} y_{h,k+1}}{\sqrt{x_{e,k+1}^2 + y_{e,k+1}^2}\sqrt{x_{h,k+1}^2 + y_{h,k+1}^2}} \quad (6.2.19)$$

$$\sin(\theta(t_{k+1})) = \frac{x_{e,k+1} \tilde{x}_{h,k+1} + y_{e,k+1} \tilde{y}_{h,k+1}}{\sqrt{x_{e,k+1}^2 + y_{e,k+1}^2}\sqrt{\tilde{x}_{h,k+1}^2 + \tilde{y}_{h,k+1}^2}} \quad (6.2.20)$$

where $\tilde{x}_{h,k+1} = \sqrt{x_{h,k+1}^2 + y_{h,k+1}^2}/\cos(\alpha(t_{k+1})) - x_{h,k+1} = y_{h,k+1}^2/x_{h,k+1}$, $\tilde{y}_{h,k+1} = -y_{h,k+1}$, Δt is the sampling interval. The robust nonlinear following controller (6.2.3) with disturbance compensation can be realized though measuring the human's motion including absolute velocity $\dot{s}(t_{k+1})$ and moving direction $\theta(t_{k+1})$.

Remark 6.2 *According to the robust nonlinear controller in (6.2.3), the disturbance compensation on human's motion is realized through adding disturbance suppression con-*

trol variables $\Delta v(t)$ and $\Delta w(t)$ to the control input to cancel the disturbance's effect. Consequently, the control input is adaptively adjusted according to the disturbance level.

6.3 Experimental results

The human-robot following control diagram is shown in Fig.6.4. The human skeleton tracking and gesture recognition is implemented by using Intel RealSense Depth Camera D435 [129] with a wide field of view and Nuitrack SDK [2]. Human's local posture with respect to robot's current position can be obtained through skeleton tracking. Gesture recognition is used to start or stop the human-following control. The human-robot following controller is responsible for generating control input to track human by using skeleton data. The sampling frequency of human-robot following control system is 30 Hz.
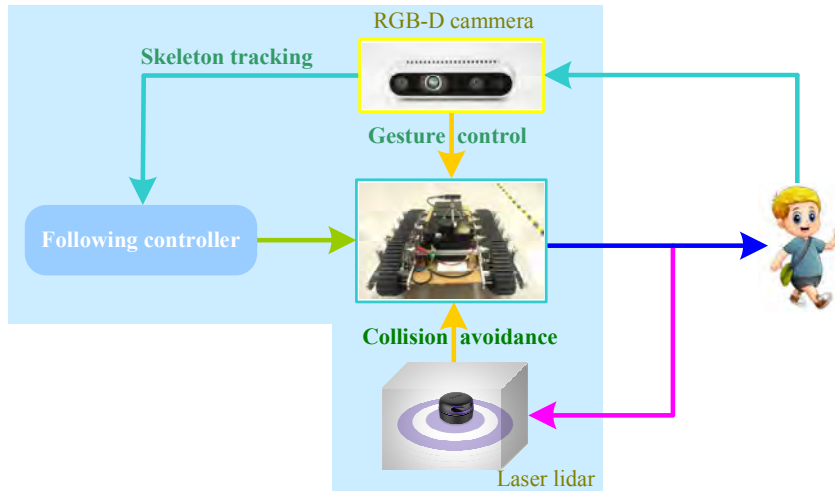
Fig. 6.4: Human-robot following control diagram

To guarantee the safety of human-robot following control, the laser radar is used for collision avoidance. When the obstacle distance is less than a safe threshold value, the robot stops following the human's motion. Some human skeleton tracking and gesture recognition results are shown in Fig.6.5.

Through hand gesture recognition, it is very convenient to realize human-robot interaction. Fig.6.6 shows a frame laser data scanning the surrounding environment to detect
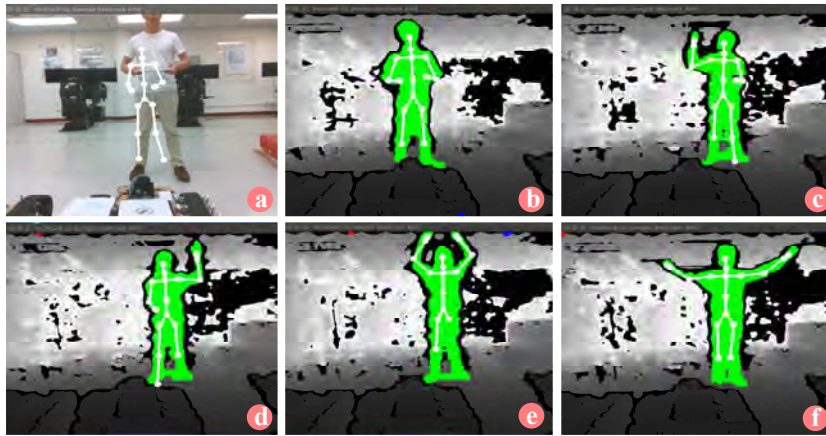
Fig. 6.5: Human skeleton tracking and gesture recognition using RGB-D camera and Nuitrack SDK [2]. (a) RGB image. (b) Skeleton tracking. (c) Swipe left. (d) Swipe right. (e) Swipe up. (f) Swipe down.
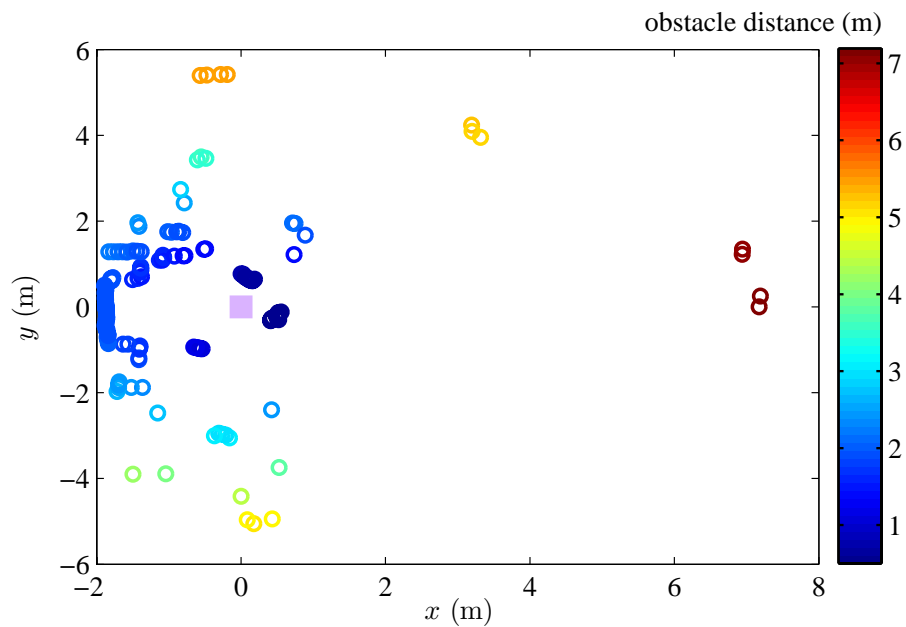
Fig. 6.6: Laser radar data for obstacle avoidance

the obstacle distance. The robot's position is located at the origin point of Fig.6.6.
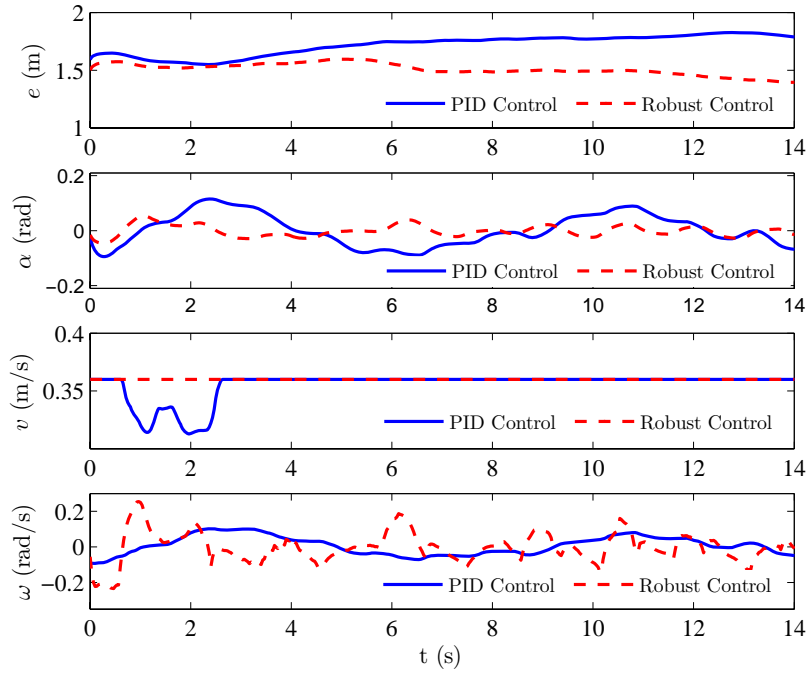
Fig. 6.7: Human-robot following state and control input: straight line

The PID controller and robust nonlinear controller proposed in this thesis are respectively applied to the human-robot following control. As shown in Fig.6.7, human-robot following state and control input under different controllers are presented. In this case, the human-robot following trajectory is a straight line as shown in Fig.6.9(a). From Fig.6.7, it is obviously observed that distance $e(t)$ and angle $\alpha(t)$ under the robust nonlinear control with disturbance compensation are more smooth compared to the PID controller. Importantly, the amplitude of human orientation angle α is less than 0.06 rad, which means that human is always located at the center of the visual field. This performance guarantees that the target is visible during the following process. For the control input, the linear velocities $v(t)$ have reached the maximum value, the angular velocity generated from robust nonlinear controller shows more dynamic characteristic to compensate the disturbance induced by the human motion. Fig.6.8 depicts the disturbance compensations of linear and angular velocities induced by human motion. Thus, the robust nonlinear controller is adaptively adjusted according the disturbance compensations $\Delta v(t)$ and $\Delta w(t)$.
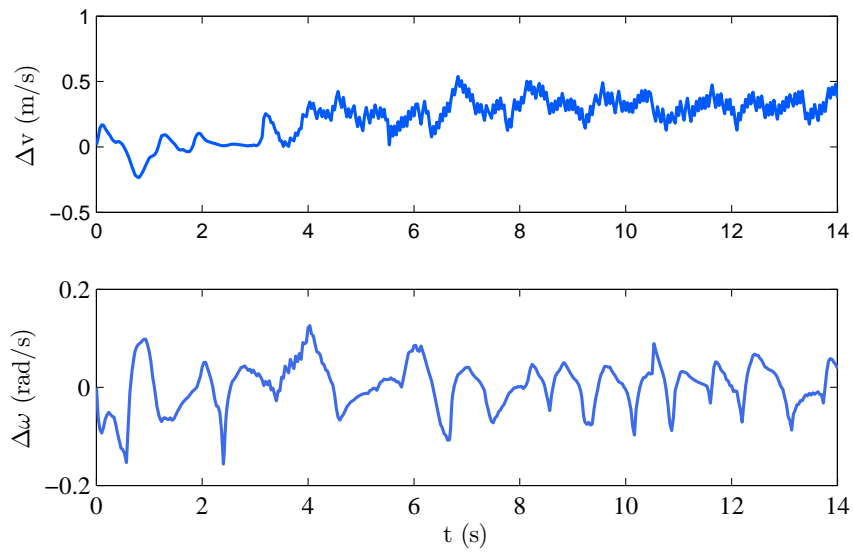
Fig. 6.8: Disturbance compensation for human motion
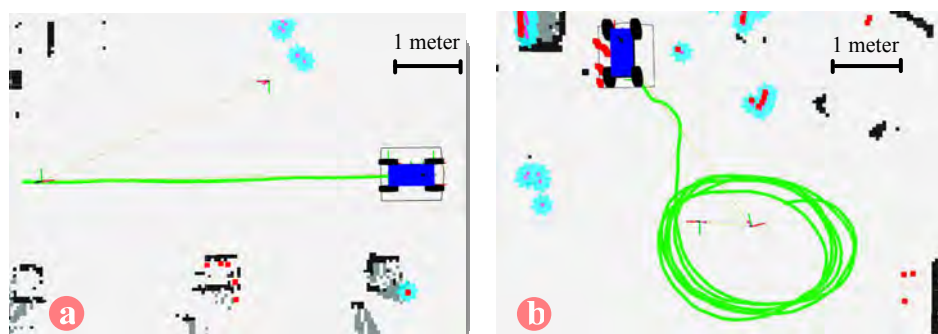
Fig. 6.9: Robot following trajectory (green line). (a)straight line (b) circle

To further illustrate the effectiveness of the proposed robust nonlinear following controller, another case of circle trajectory is considered as shown in Fig.6.9(b). The corresponding human-robot following state and control input are presented in Fig.6.10, from which it can be seen that the amplitude of human orientation angle α under robust nonlinear control is less than 0.25 rad, which means that human is still located near the center of the visual field even for the circle trajectory. While the amplitude of human orientation angle α under PID control is less than 0.5 rad. In summary, compared to the PID controller the robust controller can provide faster transient response through compensating the disturbances induced by human motion.
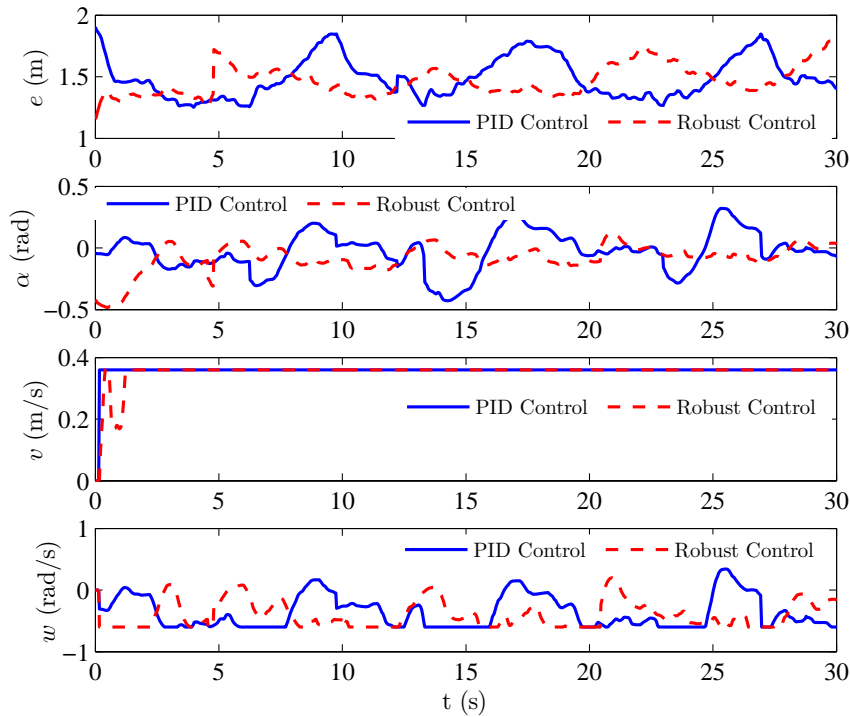
Fig. 6.10: Human-robot following state and control input: circle

The snapshot sequence of human-robot following in a curved path is shown in Fig.6.11. In Fig.6.11(a-b), the human-robot following control is activated by the swipe-up hand gesture. Fig.6.11(c-o) illustrate the process of human-robot following control in a curved path. These results of following a curved path demonstrate that the proposed robust human-robot following controller has the capability of following a continuous curved path to operate in narrow indoor environment.

Fig. 6.11: Snapshot sequence: human-robot following control in a curved path. (a-b) Controller is activated by the swipe-up hand gesture. (c-o) Following process in a curved path.

6.4 Concluding remarks

In this chapter, a robust controller with disturbance compensation is proposed for human-robot following control. The disturbance compensation on human's motion is realized through adding the disturbance suppression variables $\Delta v(t)$ and $\Delta w(t)$ to the control input to cancel the disturbance's effect. Consequently, the proposed robust nonlinear human following controller can adaptively adjust the control input according to the disturbance level. With this robust control strategy, the tracking controller has a quick response capability to guarantee that the human is always located near the center of the robot camera's FOV. Human-robot interaction is realized through the hand gesture recognition. Additionally, the laser radar is used for collision avoidance during human following. Two examples of human following including straight line and circle have illustrated the effectiveness of the proposed robust following controller.

7 Conclusions and future work

The objective of this thesis is to systematically investigate the robust control and filtering of state-dependent uncertain systems and applications.

The background of state-dependent uncertain system has been reviewed in Chapter 1. Some practical examples including the electronic circuit and mechanical system have been presented in this thesis to illustrate the applicability of state-dependent uncertain system. Further study on the evolution of system behaviour under different parameter or model switch should be conducted.

Robust stability analysis and synthesis for state-dependent uncertain systems have been presented in Chapter 2. Through constructing a new parameter dependent Lyapunov function, some improved stability conditions are established by utilizing the property of time-derivatives of uncertain parameters. A model-dependent state-feedback stabilization scheme, which has more flexibilities in controller synthesis and can achieve better system performances in practice, is presented.

Robust filter design for state-dependent uncertain system is addressed in Chapter 3. Through introducing a generalized performance index, classical filtering problems H_∞, $L_2 - L_\infty$ and dissipative filtering have been solved in a unified framework. It should be noted that the filter method proposed in this chapter is for the whole frequency domain. Thus, this filter design method inevitably has the over deign problem. To further improve the performance, finite frequency filtering can cope with the over design problem.

A novel vibration sensor based on a bio-inspired animal-limb-like structure with state-dependent nonlinearity is developed for the real-time measurement of absolute vibration motion in Chapter 4. With this bio-inspired vibration sensor, the problems of error

accumulation and real-time performance induced by traditional measurement method using accelerometer are effectively eliminated. A model-based fault detection algorithm is proposed by using the vibration sensor to cope with the real-time detection problem of weak fault with fast time-varying characteristic. The future work would extend the fault detection technology based on this bio-inspired vibration sensor to a series of practical applications for fault-tolerant control and health monitoring, such as vehicle active suspension system, railway, aeronautic engineering, and various civil structures.

Chapter 5 has introduced a tracked mobile robot with a novel passive suspension system which is constructed by using a bio-inspired animal-limb-like structure. Equipped with the novel bio-inspired suspension, the loading capacity, riding comfort and obstacle negotiation capability can be significantly enhanced and the tracked robot can be applied to various rough terrain environments. Robust navigation control using model predictive control method is realized to improve the trajectory tracking accuracy against the unknown slippage disturbances with less computational burden. Therefore, this tracked mobile robot can be well applied to various rough terrain, like construction sites. The future work would focus on more complex task design based on this stable robot platform.

Finally, a robust controller with disturbance compensation is proposed for vision based human following control of this tracked mobile robot. The disturbance compensation on human's motion is realized through adding the disturbance suppression variables to cancel the disturbance's effect. Thus the tracking controller can simultaneously guarantee the smoothness and rapidity of human following. The future work will focus on intelligent human following with capability of autonomous path planning for avoiding obstacle by combining the proposed vision based robust following control and navigation control.

Bibliography

[1] S. Sayyaddelshad and T. Gustafsson, "Observer design for a class of nonlinear systems subject to unknown inputs," in *Proceedings of 2014 European Control Conference*, Strasbourg, France, June 2014, pp. 970–974.

[2] "3D body (skeletal) tracking middleware nuitrack SDK," https://nuitrack.com, accessed: 2019-06-16.

[3] E. Feron, P. Apkarian, and P. Gahinet, "Analysis and synthesis of robust control systems via parameter-dependent Lyapunov functions," *IEEE Trans. Automat. Control*, vol. 41, no. 7, pp. 1041–1046, 1996.

[4] M. M. Fateh, "Robust control of flexible-joint robots using voltage control strategy," *Nonlinear Dyn.*, vol. 67, no. 2, pp. 1525–1537, 2012.

[5] P. P. Khargonekar, I. R. Petersen, and K. Zhou, "Robust stabilization of uncertain linear systems: quadratic stabilizability and H_∞ control theory," *IEEE Trans. Automat. Control*, vol. 35, no. 3, pp. 356–361, 1990.

[6] I. Postlethwaite, M. C. Turner, and G. Herrmann, "Robust control applications," *Annual Reviews in Control*, vol. 31, no. 1, pp. 27–39, 2007.

[7] M. Zribi, N. Almutairi, M. Abdel-Rohman, and M. Terro, "Nonlinear and robust control schemes for offshore steel jacket platforms," *Nonlinear Dyn.*, vol. 35, no. 1, pp. 61–80, 2004.

[8] B. Pal and B. Chaudhuri, *Robust Control in Power Systems*. New York, USA: Springer, 2006.

[9] C. I. Marrison and R. F. Stengel, "Design of robust control systems for a hypersonic aircraft," *Journal of Guidance, Control, and Dynamics*, vol. 21, no. 1, pp. 58–63, 1998.

[10] B. Yao, M. Al-Majed, and M. Tomizuka, "High-performance robust motion control of machine tools: an adaptive robust control approach and comparative experiments," *IEEE/ASME Trans. Mechatronics*, vol. 2, no. 2, pp. 63–76, 1997.

[11] D. Yue, Q.-L. Han, and J. Lam, "Network-based robust H_∞ control of systems with uncertainty," *Automatica*, vol. 41, no. 6, pp. 999–1007, 2005.

[12] Z. Zhang, J. Park, and H. Shao, "Adaptive synchronization of uncertain unified chaotic systems via novel feedback controls," *Nonlinear Dyn.*, vol. 81, no. 1-2, pp. 695–706, 2015.

[13] Z. Zhang and S. Xu, "Observer design for uncertain nonlinear systems with unmodeled dynamics," *Automatica*, vol. 51, no. 0, pp. 80 – 84, 2015.

[14] Z. Zhang, S. Xu, and B. Zhang, "Asymptotic tracking control of uncertain nonlinear systems with unknown actuator nonlinearity," *IEEE Trans. Automat. Contr.*, vol. 59, no. 5, pp. 1336–1341, 2014.

[15] D. Cafagna and G. Grassi, "Generation of chaotic beats in a modified Chua's circuit part II: Circuit design," *Nonlinear Dyn.*, vol. 44, no. 1-4, pp. 101–108, 2006.

[16] T. Banerjee, "Single amplifier biquad based inductor-free Chua's circuit," *Nonlinear Dyn.*, vol. 68, no. 4, pp. 565–573, 2012.

[17] S. S. Walker and J. A. Connelly, "A new negative resistance oscillator model," *Circuits, Systems and Signal Processing*, vol. 2, no. 2, pp. 213–238, 1983.

[18] N. R. Werthamer, "Nonlinear self-coupling of Josephson radiation in superconducting tunnel junctions," *Physical Review*, vol. 147, no. 1, pp. 255–263, 1966.

[19] K. S. Narendra and J. Balakrishnan, "A common Lyapunov function for stable LTI systems with commuting A-matrices," *IEEE Transactions on Automatic Control*, vol. 39, no. 12, pp. 2469–2471, Dec 1994.

[20] T. Ooba and Y. Funahashi, "Two conditions concerning common quadratic Lyapunov functions for linear systems," *IEEE Transactions on Automatic Control*, vol. 42, no. 5, pp. 719–722, May 1997.

[21] D. Liberzon and R. Tempo, "Common Lyapunov functions and gradient algorithms," *IEEE Transactions on Automatic Control*, vol. 49, no. 6, pp. 990–994, June 2004.

[22] J. Tong and N. Bajcinca, "Computation of feasible parametric regions for common quadratic Lyapunov functions," in *2018 European Control Conference (ECC)*, June 2018, pp. 807–812.

[23] P. Gahinet, P. Apkarian, and M. Chilali, "Affine parameter-dependent Lyapunov functions and real parametric uncertainty," *IEEE Trans. Automat. Control*, vol. 41, no. 3, pp. 436–442, 1996.

[24] X. Zhao, L. Zhang, P. Shi, and H. Karimi, "Robust control of continuous-time systems with state-dependent uncertainties and its application to electronic circuits," *IEEE Trans. Ind. Electron.*, vol. 61, no. 8, pp. 4161–4170, 2014.

[25] L. Zhang, T. Yang, X. Zhao, and Y. Zhu, "Robust filtering for systems with state-dependent uncertainties and application to a class of tunnel diode circuits," in *Industrial Electronics (ISIE), 2013 IEEE International Symposium on.* IEEE, 2013, pp. 1–6.

[26] L. E. Ghaoui, F. Oustry, and M. AitRami, "A cone complementarity linearization algorithm for static output-feedback and related problems," *IEEE Trans. Automat. Control*, vol. 42, no. 8, pp. 1171–1176, 1997.

[27] J. George, "Robust Kalman-Bucy filter," *IEEE Trans. Automat. Contr.*, vol. 58, no. 1, pp. 174–180, 2013.

[28] M. Makarov, A. Caldas, M. Grossard, P. Rodriguez-Ayerbe, and D. Dumur, "Adaptive filtering for robust proprioceptive robot impact detection under model uncertainties," *IEEE/ASME Trans. Mechatronics*, vol. 19, no. 6, pp. 1917–1928, 2014.

[29] D. H. Lee, Y. H. Joo, and M. H. Tak, "Periodically time-varying H_∞ memory filter design for discrete-time LTI systems with polytopic uncertainty," *IEEE Trans. Automat. Contr.*, vol. 59, no. 5, pp. 1380–1385, 2014.

[30] H. Gao, X. Meng, and T. Chen, "A parameter-dependent approach to robust H_∞ filtering for time-delay systems," *IEEE Trans. Automat. Control*, vol. 53, no. 10, pp. 2420–2425, 2008.

[31] H. Gao and C. Wang, "Robust L_2-L_∞ filtering for uncertain systems with multiple time-varying state delays," *IEEE Trans. Circuits and Systems (I)*, vol. 50, no. 4, pp. 594–599, 2003.

[32] K. Mathiyalagan, J. Park, and R. Sakthivel, "Robust reliable dissipative filtering for networked control systems with sensor failure," *IET Signal Processing*, vol. 8, no. 8, pp. 809–822, 2014.

[33] F. Alonge, F. D'Ippolito, and A. Sferlazza, "Sensorless control of induction-motor drive based on robust kalman filter and adaptive speed estimation," *IEEE Transactions on Industrial Electronics*, vol. 61, no. 3, pp. 1444–1453, 2014.

[34] X. Li and H. Gao, "Reduced-order generalized H_∞ filtering for linear discrete-time systems with application to channel equalization," *IEEE Transactions on Signal Processing*, vol. 62, no. 13, pp. 3393–3402, 2014.

[35] A. Zolghadri, F. Castang, and D. Henry, "Design of robust fault detection filters for multivariable feedback systems," *International Journal of Modelling and Simulation*, vol. 26, no. 1, pp. 17–26, 2006.

[36] L. Li, Z.-Q. Luo, T. N. Davidson, K. M. Wong, and E. Bossé, "Robust filtering via semidefinite programming with applications to target tracking," *SIAM Journal on Optimization*, vol. 12, no. 3, pp. 740–755, 2002.

[37] D. Lee, G. Vukovich, and R. Lee, "Robust adaptive unscented kalman filter for spacecraft attitude estimation using quaternion measurements," *Journal of Aerospace Engineering*, vol. 30, no. 4, p. 04017009, 2017.

[38] R. M. Palhares and P. L. Peres, "Robust H_∞ filter design with pole constraints for discrete-time systems," *Journal of the Franklin Institute*, vol. 337, no. 6, pp. 713 – 723, 2000.

[39] F. Yang and Y. Hung, "Robust mixed H_2/H_∞ filtering with regional pole assignment for uncertain discrete-time systems," *IEEE Trans. Circuits Syst. I, Fundam. Theory Appl.*, vol. 49, no. 8, pp. 1236–1241, Nov 2002.

[40] F. Yang, Z. Wang, Y. S. Hung, and H. Shu, "Mixed H_∞/H_2 filtering for uncertain systems with regional pole assignment," *IEEE Trans. Aerospace and Electronic Systems*, vol. 41, no. 2, pp. 438–448, Apr. 2005.

[41] Z. Wang and J. Fang, "Robust H_∞ filter design with variance constraints and parabolic pole assignment," *IEEE Signal Processing Letters*, vol. 13, no. 3, pp. 137–140, Mar. 2006.

[42] Y. Li, M. J. Zuo, J. Lin, and J. Liu, "Fault detection method for railway wheel flat using an adaptive multiscale morphological filter," *Mechanical Systems and Signal Processing*, vol. 84, Part A, pp. 642 – 658, 2017.

[43] B. Garcia, J. C. Burgos, and A. M. Alonso, "Transformer tank vibration modeling as a method of detecting winding deformations-part i: theoretical foundation," *IEEE Transactions on Power Delivery*, vol. 21, no. 1, pp. 157–163, Jan 2006.

[44] S. Saponara, L. Fanucci, F. Bernardo, and A. Falciani, "Predictive diagnosis of high-power transformer faults by networking vibration measuring nodes with integrated signal processing," *IEEE Transactions on Instrumentation and Measurement*, vol. 65, no. 8, pp. 1749–1760, Aug 2016.

[45] G. Shen, M. Stephen, Y. Xu, and W. Paul, "Theoretical and experimental analysis of bispectrum of vibration signals for fault diagnosis of gears," *Mechanical Systems and Signal Processing*, vol. 43, no. 1 - 2, pp. 76 – 89, 2014.

[46] V. Rai and A. Mohanty, "Bearing fault diagnosis using FFT of intrinsic mode functions in Hilbert-Huang transform," *Mechanical Systems and Signal Processing*, vol. 21, no. 6, pp. 2607 – 2615, 2007.

[47] S. Nandi, T. C. Ilamparithi, S. B. Lee, and D. Hyun, "Detection of eccentricity faults in induction machines based on nameplate parameters," *IEEE Transactions on Industrial Electronics*, vol. 58, no. 5, pp. 1673–1683, May 2011.

[48] A. Ziaja, I. Antoniadou, T. Barszcz, W. J. Staszewski, and K. Worden, "Fault detection in rolling element bearings using wavelet-based variance analysis and novelty detection," *Journal of Vibration and Control*, vol. 22, no. 2, pp. 396–411, 2016.

[49] W. Sun, H. Pan, and H. Gao, "Filter-based adaptive vibration control for active vehicle suspensions with electrohydraulic actuators," *IEEE Transactions on Vehicular Technology*, vol. 65, no. 6, pp. 4619–4626, June 2016.

[50] J. Vass, R. Šmíd, R. Randall, P. Sovka, C. Cristalli, and B. Torcianti, "Avoidance of speckle noise in laser vibrometry by the use of kurtosis ratio: Application to mechanical fault diagnostics," *Mechanical Systems and Signal Processing*, vol. 22, no. 3, pp. 647 – 671, 2008.

[51] Y. Wang, F. Li, X. Jing, and Y. Wang, "Nonlinear vibration analysis of double-layered nanoplates with different boundary conditions," *Physics Letters A*, vol. 379, no. 24, pp. 1532 – 1537, 2015.

[52] I. Kovacic, M. J. Brennan, and T. P. Waters, "A study of a nonlinear vibration isolator with a quasi-zero stiffness characteristic," *Journal of Sound and Vibration*, vol. 315, no. 3, pp. 700 – 711, 2008.

[53] X. Sun, X. Jing, J. Xu, and L. Cheng, "Vibration isolation via a scissor-like structured platform," *Journal of Sound and Vibration*, vol. 333, no. 9, pp. 2404 – 2420, 2014.

[54] Y. Li and D. Xu, "Vibration attenuation of high dimensional quasi-zero stiffness floating raft system," *International Journal of Mechanical Sciences*, vol. 126, pp. 186 – 195, 2017.

[55] Y. Wang, F. Li, Y. Wang, and X. Jing, "Nonlinear responses and stability analysis of viscoelastic nanoplate resting on elastic matrix under 3:1 internal resonances,"

International Journal of Mechanical Sciences, vol. 128-129, no. Supplement C, pp. 94 – 104, 2017.

[56] Z. Wu, X. Jing, J. Bian, F. Li, and R. Allen, "Vibration isolation by exploring bio-inspired structural nonlinearity," *Bioinspiration & Biomimetics*, vol. 10, no. 5, p. 056015, 2015.

[57] X. Jing, Y. Wang, Q. Li, and X. Sun, "Design of a quasi-zero-stiffness based sensor system for the measurement of absolute vibration displacement of moving platforms," *Smart Materials and Structures*, vol. 25, no. 9, p. 097002, 2016.

[58] H. Pan, X. Jing, W. Sun, and H. Gao, "A bioinspired dynamics-based adaptive tracking control for nonlinear suspension systems," *IEEE Transactions on Control Systems Technology*, vol. 26, no. 3, pp. 903–914, May 2018.

[59] A. Davids, "Urban search and rescue robots: from tragedy to technology," *IEEE Intelligent Systems*, vol. 17, no. 2, pp. 81–83, March 2002.

[60] T. Takei, R. Imamura, and S. Yuta, "Baggage transportation and navigation by a wheeled inverted pendulum mobile robot," *IEEE Transactions on Industrial Electronics*, vol. 56, no. 10, pp. 3985–3994, Oct 2009.

[61] G. Song, K. Yin, Y. Zhou, and X. Cheng, "A surveillance robot with hopping capabilities for home security," *IEEE Transactions on Consumer Electronics*, vol. 55, no. 4, pp. 2034–2039, November 2009.

[62] J. Pineau, M. Montemerlo, M. Pollack, N. Roy, and S. Thrun, "Towards robotic assistants in nursing homes: Challenges and results," *Robotics and Autonomous Systems*, vol. 42, no. 3, pp. 271 – 281, 2003, socially Interactive Robots.

[63] C. J. Ostafew, A. P. Schoellig, and T. D. Barfoot, "Robust constrained learning-based NMPC enabling reliable mobile robot path tracking," *The International Journal of Robotics Research*, vol. 35, no. 13, pp. 1547–1563, 2016.

[64] W. Sun, S. Tang, H. Gao, and J. Zhao, "Two time-scale tracking control of nonholonomic wheeled mobile robots," *IEEE Transactions on Control Systems Technology*, vol. 24, no. 6, pp. 2059–2069, Nov 2016.

[65] S. Yin and B. Xiao, "Tracking control of surface ships with disturbance and uncertainties rejection capability," *IEEE/ASME Transactions on Mechatronics*, vol. 22, no. 3, pp. 1154–1162, June 2017.

[66] Z. Li, T. Zhao, F. Chen, Y. Hu, C. Y. Su, and T. Fukuda, "Reinforcement learning of manipulation and grasping using dynamical movement primitives for a humanoidlike mobile manipulator," *IEEE/ASME Transactions on Mechatronics*, vol. 23, no. 1, pp. 121–131, Feb 2018.

[67] B. Mu and Y. Shi, "Distributed LQR consensus control for heterogeneous multi-agent systems: Theory and experiments," *IEEE/ASME Transactions on Mechatronics*, vol. 23, no. 1, pp. 434–443, Feb 2018.

[68] K. Nagatani, D. Endo, and K. Yoshida, "Improvement of the odometry accuracy of a crawler vehicle with consideration of slippage," in *Proceedings 2007 IEEE International Conference on Robotics and Automation (ICRA)*, Roma, Italy, April 2007, pp. 2752–2757.

[69] Y. Liu and G. Liu, "Track–stair interaction analysis and online tipover prediction for a self-reconfigurable tracked mobile robot climbing stairs," *IEEE/ASME Transactions on Mechatronics*, vol. 14, no. 5, pp. 528–538, Oct 2009.

[70] G. Mario, F. Federico, M. Matteo, and P. Fiora, "Adaptive robust three-dimensional trajectory tracking for actively articulated tracked vehicles," *Journal of Field Robotics*, vol. 33, no. 7, pp. 901–930, 2016.

[71] D. Choi and J.-H. Oh, "Active suspension for a rapid mobile robot using cartesian computed torque control," *Journal of Intelligent & Robotic Systems*, vol. 79, no. 2, pp. 221–235, Aug 2015.

[72] M. Hamaguchi, "Damping and transfer control system with parallel linkage mechanism-based active vibration reducer for omnidirectional wheeled robots," *IEEE/ASME Transactions on Mechatronics*, vol. 23, no. 5, pp. 2424–2435, Oct 2018.

[73] X. Sun and X. Jing, "Analysis and design of a nonlinear stiffness and damping system with a scissor-like structure," *Mechanical Systems and Signal Processing*, vol. 66-67, pp. 723 – 742, 2016.

[74] C. B. Low and D. Wang, "GPS-based tracking control for a car-like wheeled mobile robot with skidding and slipping," *IEEE/ASME Transactions on Mechatronics*, vol. 13, no. 4, pp. 480–484, Aug 2008.

[75] ——, "GPS-based path following control for a car-like wheeled mobile robot with skidding and slipping," *IEEE Transactions on Control Systems Technology*, vol. 16, no. 2, pp. 340–347, March 2008.

[76] S. J. Yoo and T.-H. Kim, "Distributed formation tracking of networked mobile robots under unknown slippage effects," *Automatica*, vol. 54, pp. 100 – 106, 2015.

[77] F. A. Fontes, "A general framework to design stabilizing nonlinear model predictive controllers," *Systems & Control Letters*, vol. 42, no. 2, pp. 127 – 143, 2001.

[78] D. Gu and H. Hu, "Receding horizon tracking control of wheeled mobile robots," *IEEE Transactions on Control Systems Technology*, vol. 14, no. 4, pp. 743–749, July 2006.

[79] Z. Li, C. Yang, C. Y. Su, J. Deng, and W. Zhang, "Vision-based model predictive control for steering of a nonholonomic mobile robot," *IEEE Transactions on Control Systems Technology*, vol. 24, no. 2, pp. 553–564, March 2016.

[80] M. Mizuochi, T. Tsuji, and K. Ohnishi, "Multirate sampling method for acceleration control system," *IEEE Transactions on Industrial Electronics*, vol. 54, no. 3, pp. 1462–1471, June 2007.

[81] T. Wang, H. Gao, and J. Qiu, "A combined adaptive neural network and nonlinear model predictive control for multirate networked industrial process control," *IEEE Transactions on Neural Networks and Learning Systems*, vol. 27, no. 2, pp. 416–425, Feb 2016.

[82] N. Bellotto and H. Hu, "Multisensor-based human detection and tracking for mobile service robots," *IEEE Transactions on Systems, Man, and Cybernetics, Part B: Cybernetics*, vol. 39, no. 1, pp. 167–181, Feb 2009.

[83] J. Mainprice and D. Berenson, "Human-robot collaborative manipulation planning using early prediction of human motion," in *2013 IEEE/RSJ International Conference on Intelligent Robots and Systems (IROS)*, Nov 2013, pp. 299–306.

[84] N. Hirose, R. Tajima, K. Sukigara, and M. Tanaka, "Personal robot assisting transportation to support active human life," in *2014 IEEE International Conference on Robotics and Automation (ICRA)*, May 2014, pp. 2223–2230.

[85] W. Ye, Z. Li, C. Yang, J. Sun, C. Su, and R. Lu, "Vision-based human tracking control of a wheeled inverted pendulum robot," *IEEE Transactions on Cybernetics*, vol. 46, no. 11, pp. 2423–2434, Nov 2016.

[86] N. Yao, E. Anaya, Q. Tao, S. Cho, H. Zheng, and F. Zhang, "Monocular vision-based human following on miniature robotic blimp," in *2017 IEEE International Conference on Robotics and Automation (ICRA)*, May 2017, pp. 3244–3249.

[87] M. Gupta, S. Kumar, L. Behera, and V. K. Subramanian, "A novel vision-based tracking algorithm for a human-following mobile robot," *IEEE Transactions on Systems, Man, and Cybernetics: Systems*, vol. 47, no. 7, pp. 1415–1427, July 2017.

[88] "KLM's Robot Assistant helps passengers through the airport and make air travel less stressful," http://klmcare-e-entry.com/, accessed: 2019-06-24.

[89] N. Kejriwal, S. Garg, and S. Kumar, "Product counting using images with application to robot-based retail stock assessment," in *2015 IEEE International Conference on Technologies for Practical Robot Applications (TePRA)*. IEEE, 2015, pp. 1–6.

[90] L. Kocarev, K. S. Halle, K. Eckert, L. O. Chua, and U. Parlitz, "Experimental demonstration of secure communications via chaotic synchronization," *International Journal of Bifurcation and Chaos*, vol. 02, no. 03, pp. 709–713, 1992.

[91] T. Yang and L. Chua, "Impulsive stabilization for control and synchronization of chaotic systems: theory and application to secure communication," *IEEE Trans. Circuits Syst. I, Fundam. Theory Appl.*, vol. 44, no. 10, pp. 976–988, 1997.

[92] J. C. Geromel and P. Colaneri, "Robust stability of time varying polytopic systems," *Systems & Control Letters*, vol. 55, no. 1, pp. 81–85, 2006.

[93] F. Bruzelius, *Linear Parameter-Varying Systems*. Chalmers University of Technology, Sweden: Thesis for the Degree of Doctor of Philosophy, 2004.

[94] J. Löfberg, "Yalmip : A Toolbox for Modeling and Optimization in MATLAB," in *Proceedings of the CACSD Conference*, Taipei, Taiwan, 2004. [Online]. Available: http://users.isy.liu.se/johanl/yalmip

[95] K.-C. Toh, M. J. Todd, and R. H. Tütüncü, "Sdpt3-A MATLAB software package for semidefinite programming, version 1.3," *Optimization methods and software*, vol. 11, no. 1-4, pp. 545–581, 1999. [Online]. Available: http://www.math.nus.edu.sg/~mattohkc/sdpt3.html

[96] K. W. Lee and S. N. Singh, "Robust control of chaos in Chua's circuit based on internal model principle," *Chaos, Solitons & Fractals*, vol. 31, no. 5, pp. 1095–1107, 2007.

[97] J. H. Deane and D. C. Hamill, "Instability, subharmonics, and chaos in power electronic systems," *IEEE Trans. Power Electron.*, vol. 5, no. 3, pp. 260–268, 1990.

[98] X. Zhao, L. Zhang, P. Shi, and H. Karimi, "Robust control of continuous-time systems with state-dependent uncertainties and its application to electronic circuits," *IEEE Trans. Ind. Electron.*, vol. 61, no. 8, pp. 4161–4170, 2014.

[99] B. Zhang, W. X. Zheng, and S. Xu, "Filtering of markovian jump delay systems based on a new performance index," *IEEE Trans. Circuits Syst. I*, vol. 60, no. 5, pp. 1250–1263, May 2013.

[100] M. J. Lacerda, S. Tarbouriech, G. Garcia, and P. L. Peres, "Filter design for nonlinear polynomial systems," *Systems & Control Letters*, vol. 70, no. 0, pp. 77 – 84, 2014.

[101] H. Gao, J. Lam, and C. Wang, "Robust energy-to-peak filter design for stochastic time-delay systems," *Systems & Control Letters*, vol. 55, no. 2, pp. 101 – 111, 2006.

[102] B. Brogliato, R. Lozano, B. Maschke, and O. Egeland, *Dissipative Systems Analysis and Control: Theory and Applications, 2nd ed.* Springer-Verlag London, 2007.

[103] X.-Z. Dong, "Robust strictly dissipative control for discrete singular systems," *IET Control Theory & Applications*, vol. 1, no. 4, pp. 1060–1067, 2007.

[104] S. K. Nguang and W. Assawinchaichote, "H_∞ filtering for fuzzy dynamical systems with $\mathcal{D}$ stability constraints," *IEEE Trans. Circuits Syst. I, Fundam. Theory Appl.*, vol. 50, no. 11, pp. 1503–1508, 2003.

[105] Q. N. Xu, K. M. Lee, H. Zhou, and H. Y. Yang, "Model-based fault detection and isolation scheme for a rudder servo system," *IEEE Transactions on Industrial Electronics*, vol. 62, no. 4, pp. 2384–2396, April 2015.

[106] Z. Zhao, Y. Yang, S. X. Ding, and L. Li, "Fault-tolerant control for systems with model uncertainty and multiplicative faults," *IEEE Transactions on Systems, Man, and Cybernetics: Systems*, 2017, doi: 10.1109/TSMC.2017.2759144.

[107] H. Pan, W. Sun, H. Gao, and X. Jing, "Disturbance observer-based adaptive tracking control with actuator saturation and its application," *IEEE Transactions on Automation Science and Engineering*, vol. 13, no. 2, pp. 868–875, April 2016.

[108] Z. Zhao, Y. Yang, and Y. Zhang, "Fault tolerant control using adaptive output integral-type sliding mode," *Journal of the Franklin Institute*, vol. 354, no. 6, pp. 2648 – 2662, 2017.

[109] J. Yao, Z. Jiao, and D. Ma, "A practical nonlinear adaptive control of hydraulic servomechanisms with periodic-like disturbances," *IEEE/ASME Transactions on Mechatronics*, vol. 20, no. 6, pp. 2752–2760, Dec 2015.

[110] J. Yao, W. Deng, and Z. Jiao, "Rise-based adaptive control of hydraulic systems with asymptotic tracking," *IEEE Transactions on Automation Science and Engineering*, vol. 14, no. 3, pp. 1524–1531, July 2017.

[111] W. Sun, Y. Zhang, Y. Huang, H. Gao, and O. Kaynak, "Transient-performance-guaranteed robust adaptive control and its application to precision motion control systems," *IEEE Transactions on Industrial Electronics*, vol. 63, no. 10, pp. 6510–6518, Oct 2016.

[112] J. Yao and W. Deng, "Active disturbance rejection adaptive control of hydraulic servo systems," *IEEE Transactions on Industrial Electronics*, vol. 64, no. 10, pp. 8023–8032, Oct 2017.

[113] D. Lehrer, V. Adetola, and M. Guay, "Parameter identification methods for nonlinear discrete-time systems," in *Proceedings of the 2010 American Control Conference*, Baltimore, MD, USA, June 2010, pp. 2170–2175.

[114] Y. Zhao, J. Lam, and H. Gao, "Fault detection for fuzzy systems with intermittent measurements," *IEEE Transactions on Fuzzy Systems*, vol. 17, no. 2, pp. 398–410, April 2009.

[115] H. Li, Y. Gao, P. Shi, and H. K. Lam, "Observer-based fault detection for nonlinear systems with sensor fault and limited communication capacity," *IEEE Transactions on Automatic Control*, vol. 61, no. 9, pp. 2745–2751, Sept 2016.

[116] J. Slavič, A. Brković, and M. Boltežar, "Typical bearing-fault rating using force measurements: application to real data," *Journal of Vibration and Control*, vol. 17, no. 14, pp. 2164–2174, 2011.

[117] P. T. Mietek A. Brdys, *Iterative Algorithms for Multilayer Optimizing Control.* London, U.K.: Imperial College Press, 2005.

[118] L. Würth, R. Hannemann, and W. Marquardt, "A two-layer architecture for economically optimal process control and operation," *Journal of Process Control*, vol. 21, no. 3, pp. 311 – 321, 2011, thomas McAvoy Festschrift.

[119] Y. Tang, C. Peng, S. Yin, J. Qiu, H. Gao, and O. Kaynak, "Robust model predictive control under saturations and packet dropouts with application to networked flotation processes," *IEEE Transactions on Automation Science and Engineering*, vol. 11, no. 4, pp. 1056–1064, Oct 2014.

[120] Y. Wang and X. Jing, "Nonlinear stiffness and dynamical response characteristics of an asymmetric X-shaped structure," *Mechanical Systems and Signal Processing*, vol. 125, pp. 142 – 169, 2019, exploring nonlinear benefits in engineering.

[121] "Seekur mobile robot with 4 omnidirectional drive wheels," https://www.generationrobots.com/en/402404-robot-mobile-seekur.html, accessed: 2019-06-29.

[122] C. Shen, B. Buckham, and Y. Shi, "Modified C/GMRES algorithm for fast nonlinear model predictive tracking control of AUVs," *IEEE Transactions on Control Systems Technology*, vol. 25, no. 5, pp. 1896–1904, Sept 2017.

[123] E. W. Dijkstra, "A note on two problems in connexion with graphs," *Numerische mathematik*, vol. 1, no. 1, pp. 269–271, 1959.

[124] C. Rösmann, W. Feiten, T. Wösch, F. Hoffmann, and T. Bertram, "Trajectory modification considering dynamic constraints of autonomous robots," in *the 7th German Conference on Robotics*, Munich, Germany, May 2012, pp. 74–79.

[125] T. Moore and D. Stouch, "A generalized extended kalman filter implementation for the robot operating system," in *13th International Conference on Intelligent Autonomous Systems*, Padua, Italy, July 2014, pp. 335–348.

[126] M. Diehl, H. J. Ferreau, and N. Haverbeke, "Efficient numerical methods for nonlinear MPC and moving horizon estimation," in *Lecture Notes in Control and Information Sciences: Nonlinear model predictive control*, vol. 384. Springer, 2009, pp. 391–417.

[127] B. Houska, H. J. Ferreau, and M. Diehl, "An auto-generated real-time iteration algorithm for nonlinear MPC in the microsecond range," *Automatica*, vol. 47, no. 10, pp. 2279 – 2285, 2011.

[128] M. Aicardi, G. Casalino, A. Bicchi, and A. Balestrino, "Closed loop steering of unicycle like vehicles via lyapunov techniques," *IEEE Robotics & Automation Magazine*, vol. 2, no. 1, pp. 27–35, March 1995.

[129] "Intel RealSense Depth Camera D435," https://www.intelrealsense.com/depth-camera-d435/, accessed: 2019-06-18.